SEARCHES FOR NEW PHYSICS USING THE ATLAS DETECTOR

Approved by:

Prof. Ryszard Stroynowski

Prof. Jingbo Ye

Prof. Gary Evans

Prof. Kent Hornbostel

SEARCHES FOR NEW PHYSICS USING THE ATLAS DETECTOR

A Dissertation Presented to the Graduate Faculty of the

Dedman College

Southern Methodist University

in

Partial Fulfillment of the Requirements

for the degree of

Doctor of Philosophy

with a

Major in Physics

by

Ana Firan

M.S., University of Craiova, Romania, 1994

July 31, 2008

Firan , Ana M.S., University of Craiova, Romania, 1994

Searches for New Physics using the ATLAS Detector

Advisor: Prof. Ryszard Stroynowski

Co-advisor: Associate Professor Prof. Jingbo Ye

Doctor of Philosophy degree conferred July 31, 2008
Dissertation completed June 30, 2008

The search for the Higgs boson has been one of the main motivations for the construction of the Large Hadron Collider. In this study we show that there are new Higgs decay channels, previously neglected by the literature that proceed via internal photon conversion. For the Higgs masses of interest at the CERN LHC in the range of 100-150 GeV, the conversions to pairs of fermions represent a significant fraction of Higgs decays.

In addition to the Higgs boson, other particles might be produced, like magnetic monopoles. We present the results of the simulation of the Dirac magnetic monopole production and discuss the feasibility of its detection with the ATLAS detector. This study shows that the magnetic monopole, if it exists, will be detected with the ATLAS detector. The number of events estimated for a luminosity of 1 fb^{-1} corresponding to the first year of the ATLAS experiment, indicates that the magnetic monopole will be found in the early ATLAS data.

TABLE OF CONTENTS

LIST OF FIGURES

LIST OF TABLES

ACKNOWLEDGMENTS

I would like to express my gratitude to my advisers, Ryszard Stroynowski and Jingbo Ye, for their guidance, support and encouragement throughout my graduate years. Many interesting meetings and conversations contributed greatly to my understanding of physics and scientific research methods.

I would also like to thank the Dedman College and the Lightner-Sam Foundation. This work would not have been possible without their generous support.

Chapter 1

THE LARGE HADRON COLLIDER

1.1. Particle Physics and the need for LHC

The question "What is the Universe made of?" haunted human kind for centuries. The "search for the origin of matter" means the understanding of the basic building blocks of matter, called elementary particles, where the term "elementary" has a reductionist meaning of structureless. This requires not only understanding of their characteristics but also how they interact.

In ancient Greece, Aristoteles' four-element theory suggested that the world was built from four primordial elements: water, air, fire and earth. Later on, the idea that matter consists of minimum units, called atoms, was proposed by another Greek philosopher, Demokritos. "Atom" means "unable to be divided". Atoms remained the smallest known components of matter until 1897 Thomson discovered the electron and in 1909 Rutherford showed that the atom had a dense nucleus and orbiting electrons. Later physicists showed that the nucleus was composed of neutrons and protons. More recently, in 1968, the Stanford Linear Accelerator Center(SLAC), announced the discovery of quarks in electron proton collisions. Quarks join together to form protons, neutrons and other subatomic particles like mesons and baryons. Several hundred such subatomic particles have been discovered so far. However, most of them are not fundamental, they are composed of smaller units, the quarks.

The fundamental particles are spin half particles called fermions.

They are divided into two groups: quarks (up, down, charm, strange, top and bottom) and leptons (electron, electron neutrino, muon, muon neutrino, tau and tau neutrino) [1]. In Fig. 1.1 a diagram shows the organization of fermions.

Fermions are also classified into three generations which are identical in every

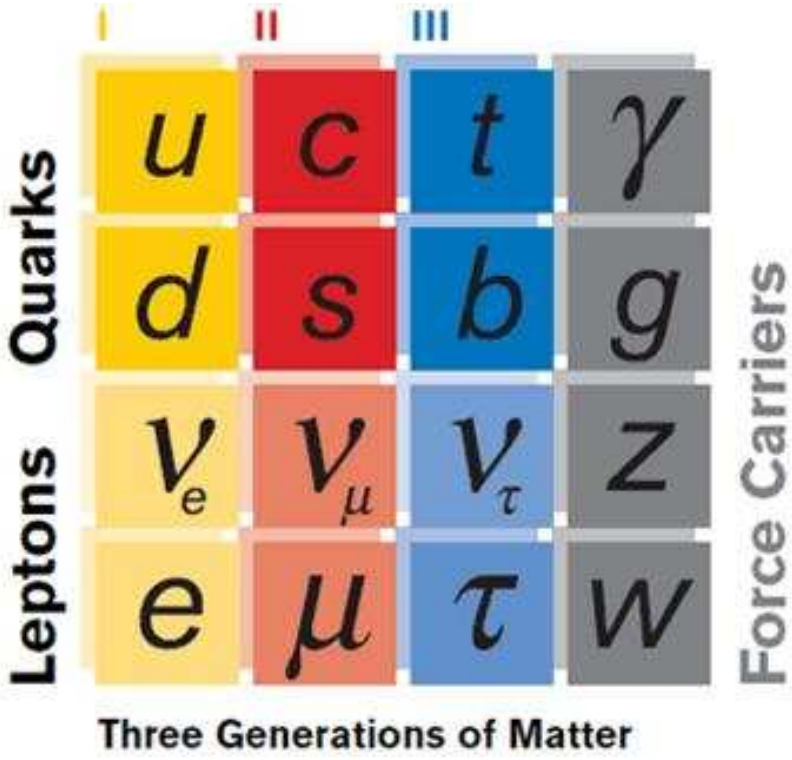

Figure 1.1. Standard Model; fermion organization and force carriers.

attribute except their masses. The first generation includes the up (u) and down (d) quarks, that are the constituents of nucleons, and the electron and the electron neutrino. They are the basic constituents of the everyday world that surrounds us. The quarks corresponding to the other two generations form heavier, short-lived particles.

They and their corresponding charged leptons rapidly decay into quarks and leptons of the first generation. Quarks have fractional electric charges in units of 1/3 or 2/3 of the charge of the electron ($e = 1.602 \cdot 10^{-19}$ C) and leptons have charges in units of 1 or 0. For every quark or lepton there is a corresponding antiparticle. For example, there are antiquarks, anti-electrons (called positrons). There is an unresolved question whether neutrinos are their own antiparticles. If they are Dirac neutrinos, then the antineutrinos and neutrinos are distinct; but if they are Majorana neutrinos, then the antineutrinos and neutrinos are the same.

Free quarks cannot be observed as separate objects. They have an internal property called color. There are three colors: red, blue and green. Each individual color does not manifest itself in any observable that can be detected in experiments. Only color neutral objects are detectable as isolated particles. Thus quarks combine to form baryons and mesons. Baryons are made of three quarks. Examples of baryons are the protons and neutrons found in the atomic nuclei (and also anti-protons and anti-neutrons). Mesons are short lived particles that are made of quark-antiquark pairs.

We describe interactions between all these particles as mediated by four distinct forces, characterized by widely different ranges and strengths. The strong force binds quarks into protons, neutrons and mesons, and holds the nucleus of the atom together despite the repulsive electromagnetic force between protons. The strong nuclear force has a range of about 10^{-15} m. The weak force is responsible for radioactive decay of atomic nuclei and has a range of 10^{-17} m. The electromagnetic force describes the interaction between charged particles. This force governs much of macroscopic physics and has infinite range but its strength decreases with the inverse of the square of the distance. The fourth force, gravity, also has infinite range but it is too weak to be observable in laboratory experiments for elementary particles.

The standard picture used in textbooks explains forces as resulting from matter particles exchanging force-carrying particles. These carriers are integer spin particles that follow the Bose-Einstein statistics called bosons [2].

Interactions among electrically charged particles are due to the exchange of quanta of the electromagnetic field called photons. The photon is massless which accounts for the long range of the electromagnetic force. The shorter range of the weak force is mediated by the charged W^+, W^- and neutral Z bosons. Because the $W^\pm$ particles carry electric charge they must couple to the photon, implying a theory that unites the weak and electromagnetic interactions. In distinction to the photons, the W bosons couple only to left-handed fermions (with spin oriented opposite to the direction of motion). The strong force is mediated by the exchange of massless gluons between quarks. Quarks carry a quantum number called color which can be "red", "blue" or "green". It takes the sum of the anti-symmetrized products of all three colors to make a colorless object. Gluons possess color charge, because they carry color-anticolor charge, and hence they couple to one another. As a consequence, the color force between two colored particles increases in strength with increasing distance. Thus quarks and gluons cannot appear as free particles, but exist only inside composite particles, called hadrons, that have no net color charge. In the quantum description of the gravity, the gravitational force is associated with a neutral boson named graviton.

Standard Model (SM) [3], [4], [5] of particle physics is a theoretical framework that has been enormously successful in predicting a wide range of phenomena. The main achievement of the SM is the elaboration of a unified description of the strong, weak and electromagnetic forces in the language of quantum field theories.

Moreover, the SM combines the weak and electromagnetic forces in a single electroweak theory, similarly to the Maxwells unification of the apparently distinct forces of electricity and magnetism [6].

Despite the Standard Model's effectiveness at describing the phenomena within its domain, it is nevertheless incomplete. The theory incorporates only three out of the four fundamental forces, omitting gravity. There are also important questions that it cannot answer, such as what is the dark matter, what happened to the missing antimatter in the Universe, and more.

One of the most important questions that the Standard Model faces refers to the unification of the weak and electromagnetic forces. If those two forces are part of the same electroweak force, why is it that the exchange particle for the electromagnetic interaction, the photon, is massless while the W and Z have masses more than 80 times that of a proton. In the Standard Model, spontaneous electroweak symmetry breaking is the process that give masses to the W and Z bosons and the fermions. It takes place when a system that is symmetric has a vacuum state that is not symetric. A detailed description of the mechanism will be given in chapter (2.1).

In mathematical terms the behavior of a system is described by the Lagrangians. The Lagrangians can be split into a kinetical term and a potential term. It is in the potential term that the symmetry breaking occurs. If we assume a potential term of the shape of the famous "mexican hat", and we imagine a ball sitting at the top of the hat, that state is symmetric but it is not stable(Fig. 1.2). The ball could spontaneously roll down at any time and by doing this will single out a preferred direction thus breaking the symmetry. This is an intuitive example of symmetry breaking. The idea of a field that fills all space and has a nonzero expectation value was proposed by Peter Higgs in 1964 [7]. The field is called the Higgs field and its quanta is called the Higgs boson.

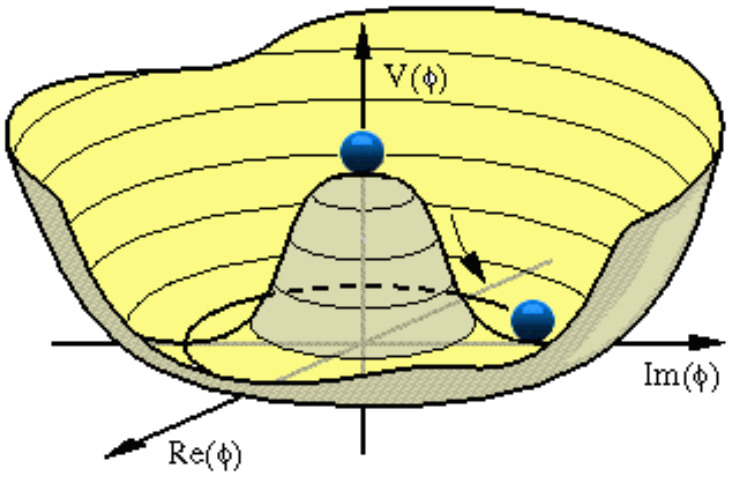

Figure 1.2. Mexican hat potential.

The Higgs mechanism explains how particles acquire mass as they move through the Higgs field. This is a vital part of the Standard Model as without it the theory suggests that all particles should be massless [8]. The quarks, leptons and W and Z bosons continuously collide with these Higgs bosons as they move through the vacuum. The whole Higgs field acts as a molasses slowing down anything that interacts with it; the stronger the interactions between the particles and the Higgs field are, the heavier the particles become. The discovery of the Higgs boson is therefore a key element in proving the validity of the Standard Model.

The SM is further characterized by a high degree of symmetry. CP is the product of two symmetries: C for charge conjugation, which transforms a particle into its antiparticle, and P for parity, which creates the mirror image of a physical system. James Cronin and Val Fitch with co-workers proved in 1964 that CP symmetry could be broken. Thus they won the 1980 Nobel Prize [9].

Their discovery was based on the fact that neutral kaons can transform into their antiparticles (in which each quark is replaced with its antiquark) and vice versa, but such transformation does not occur with exactly the same probability in both directions. So it appears that antimatter is not precisely the three-coordinate mirror image of matter. While this effect is small and may seem to be unimportant, it could explain one of the largest questions in physics: "Why is the universe made almost entirely of matter?". The big bang is believed to have produced equal amounts of matter and antimatter. However, whenever matter and antimatter meet, they annihilate creating gamma rays, so this theory would suggest that both matter and antimatter should all have annihilated long ago, and the universe should today simply consist of radiation. Since CP violation exists, the small difference between matter and antimatter may explain why, after all the early annihilation and creation of mater antimatter pairs, there is a tiny surplus of matter left over to form galaxies. This hypothesis remains to be proven.

Supersymetry (SUSY) could probably provide some answers to questions like "What is Dark Matter?" or "Is it possible to unify electroweak and strong interactions in one Grand Unified Theory?" [10]. In particle physics, SUSY is a symmetry that relates each elementary particle of a given spin to other particles called superparteners that have a spin that differs by half a unit. That means that for every type of boson there is a corresponding type of fermion, and vice-versa. Incorporating spin supersymmetry into the Standard Model requires doubling the number of particles because the particles in the Standard Model cannot be superpartners to each other. With the addition of the new particles, there are many possible new interactions. Each SUSY particle is expected to be short lived, decaying into supersymetric particles of lower mass. SUSY particles with the lowest mass cannot decay furthermore and it is stable.

Stable, charged supersymetric particles are excluded since they should have been seen already. This leaves open the possibility that the lowest mass SUSY particle is neutral and it is called neutralino. In many SUSY models neutralinos could serve as a WIMPs (Weakly Interacting Massive Particles) proposed to explain astronomical observations of dark matter [11]. Moreover, if supersymmetry exists close to the TeV energy scale, it allows for a solution of another problem that puzzles particle physics: the unification of the weak interactions, the strong interactions and electromagnetism.

In summary, we expect that the Standard Model of particle physics is only a part of a bigger picture that includes new physics that has so far been hidden deep in the subatomic world or in the dark recesses of the Universe. New information from experiments at the Large Hadron Collider will help us find some of the missing pieces. In addition to the Higgs boson, other particles that might be produced, like strangelets [12], micro black holes [13], magnetic monopoles and supersymmetric particles.

1.2. The Large Hadron Collider

1.2.1. Description

Particle physicists study matter by colliding accelerated particles. Accelerators use electric fields to accelerate charged particles to high energies. Many of today's accelerators are colliders in which two particle beams are accelerated in opposite directions and are made to collide head on inside the devices that detect objects created in these collisions. In these collisions practically all the particle energy can be used for particle production. Based on Einstein's equation $E = mc^2$, when those particles collide they can into "transform" into more massive or even new particles.

Highly energetic particles have high momentum and thus having short wavelengths according to de Broglie formula $\lambda = h/p$ where h is Planck's constant, λ the wavelength of the accelerated particles and is p the momentum. This makes possible the exploration of the structure of matter with an extremely high spatial resolution. Using colliders is the most efficient and economic way to obtain high collision energies to explore the interior of matter and to produce new particles. Huge detector systems surround the collision points and register what is happening in the collisions.

The Large Hadron Collider (LHC) at CERN will extend the frontiers of known particle physics. The high luminosity and increased cross-sections at the LHC will allow precision tests of QCD (Quantum Chromodynamics), electroweak interactions, and flavour physics. It is proton-proton particle accelerator located at CERN (Conseil Europen pour la Recherche Nuclaire -European Council for Nuclear Research), near Geneva, Switzerland. The collider is situated underground, in a circular tunnel on the border of France and Switzerland. The main ring has has a circumference of 27 kilometres (17 mi) and a depth ranging from 50 to 175 metres underground. The tunnel hosts two pipes, each pipe containing a beam of protons which travels in opposite directions around the ring.

Before being injected in the main accelerator the protons are passed through a series of systems that successively increase their kinetic energy. The first system is the linear accelerator Linac 2 generating 50 MeV protons which feeds the Proton Synchrotron Booster (PSB). Protons are then injected at 1.4 GeV into the Proton Synchrotron (PS) and accelerated to 26 GeV. Finally the Super Proton Synchrotron (SPS) is used to increase the energy of protons up to 450 GeV.

Thus each proton will reach an energy of 7 TeV, giving a total collision energy of 14 TeV. At these energies it will take less than 90 microseconds for an individual proton to travel once around the collider. There are 1232 dipole magnets keeping the two beams on their circular path.

The protons are "bunched" together into 2,808 bunches, so that interactions between the two beams will take place at discrete intervals never shorter than 25 ns apart. This means that bunches containing 10^{11} protons will collide 40 million times per second.

Because the size of the proton is very small, about 10^{-14} m, they represent a very small target. Therefor we need to reduce the distance between them, in a bunch, by concentrating the beam to a very small diameter. This increases the interaction probability between bunches traveling in opposite direction. There are 392 quadrupole magnets used to keep the beams focused.

The interaction rate is measured by a parameter called *Luminosity*. Luminosity is a function of the number of protons in the two colliding beams.

$$L = fn\frac{N_1 N_2}{A} \tag{1.1}$$

where N_1 and N_2 are the number of protons in each of the beam bunches, f is the collision frequency , n is the number of bunches and A is the transverse area of the beam. The LHC has a design luminosity of $10^{24}\ cm^{-2}s^{-1}$.

Six detectors are being constructed at the LHC, located underground in large caverns excavated at the LHC's intersection points. Two are the general purpose detectors, ATLAS (A Toroidal LHC ApparatuS) and CMS (Compact Muon Solenoid).

The ALICE detector is designed to study heavy ion collisions in order to evaluate the properties of quark-gluon plasma. The other three (LHCb, TOTEM, and LHCf) are relatively smaller and more specialized.

1.2.2. ATLAS detector

The "A Toroidal LHC ApparatuS" (ATLAS) experiment consists of a series of concentric detection layers arranged with cylindrical symmetry around the interaction point where the proton beams collide. It has three major parts: the Inner Detector, the calorimeters and the muon spectrometer. Each layer has a specific function. The Inner Detector detects the trajectories of the particles, the calorimeters measure their energies, and the muon system makes additional identification of highly penetrating muons. The two magnet systems bend electrically charged particles in the Inner Detector and the muon spectrometer, allowing their momenta to be measured. The only long lived particles that cannot be detected directly are neutrinos; their presence is inferred by noticing a momentum imbalance among detected particles [14]. In fig. 1.3 the different layers of the ATLAS detector are presented in a longitudinal section.

1.2.2.1. Inner Detector

The Inner Detector begins a few centimeters from the proton beam axis, extends to a radius of 1.2 meters, and is seven meters in length along the beam pipe. Its basic function is to track the path of charged particles. There is a two Tesla magnetic field surrounding the entire Inner Detector region causing the trajectories of electrically charged particles to bend.

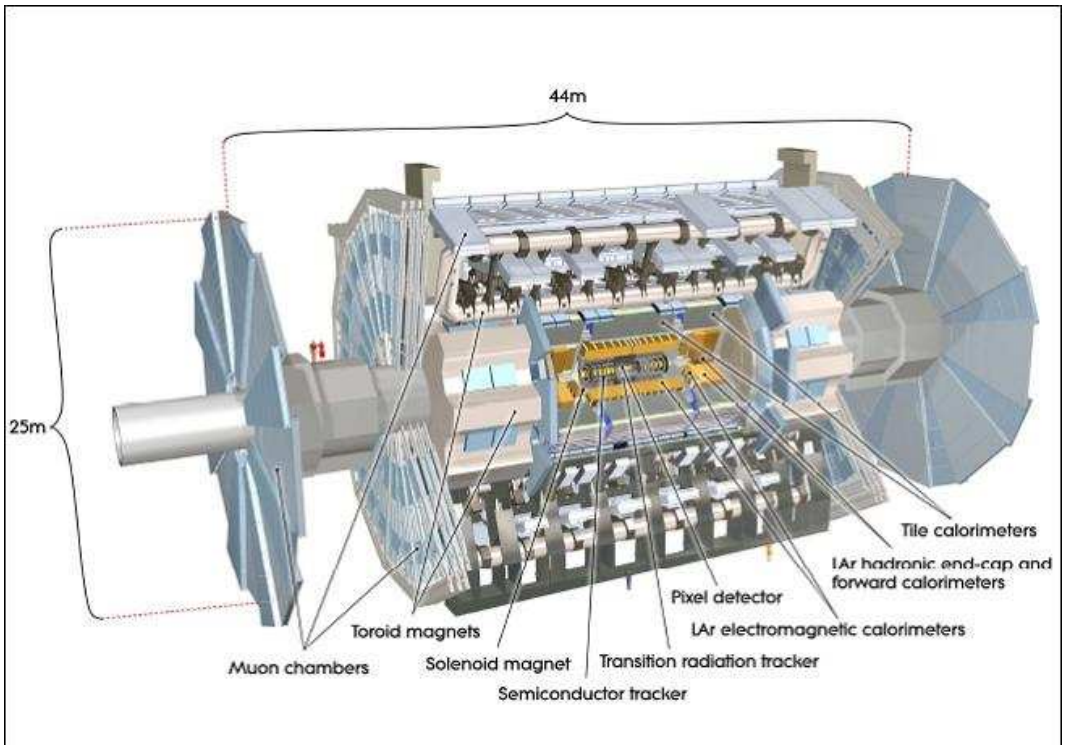

Figure 1.3. Cut-away view of the ATLAS detector.

The direction of the curve gives information about the particle's charge and the degree of curvature relates its momentum.

The Inner Detector, being the closest detector to the interaction point, needs to identify with extreme accuracy the trajectories of the produced particles. This is done by precise pattern recognition, momentum and vertex measurements, and electron identification. The detector layers are designed to achieve these goals. There are high-resolution semiconductor pixel and strip detectors in the inner part of the tracking volume, and straw-tube tracking detectors with the capability to generate and detect transition radiation in its outer part [15]. The Inner Detector has three parts(see Fig. 1.4):

- the silicon Pixel detector
- the SemiConductor Tracker (SCT)
- the Transition Radiation Tracker (TRT)

The three layers have increasing resolution. Closest to the collision point, we have pixel detector with the best spatial resolution. Silicon strips have larger spatial resolution but are more cost efficient. The TRT tubes are the less expensive and have the poorest resolution.

The detectors sensors are silicon pixel and micro-strip sensors for SCT and TRT sub-systems, and straw tubes filled with a Xe/CO2/O2 gas mixture for the TRT. The silicon detectors detect the primary ionization directly. Silicon is a solid, so it is much denser than gases that means that more primary ions are produced and it also means that the charged particle loses more energy in order to be tracked. Being a solid, there is also less diffusion than in a gas, which means it has a higher resolution.

The Pixel Detector is the innermost part of the detector and contains three concentric detection layers around the beam pipe, in the barrel region, and three disks on each end-cap(see Fig. 1.3).

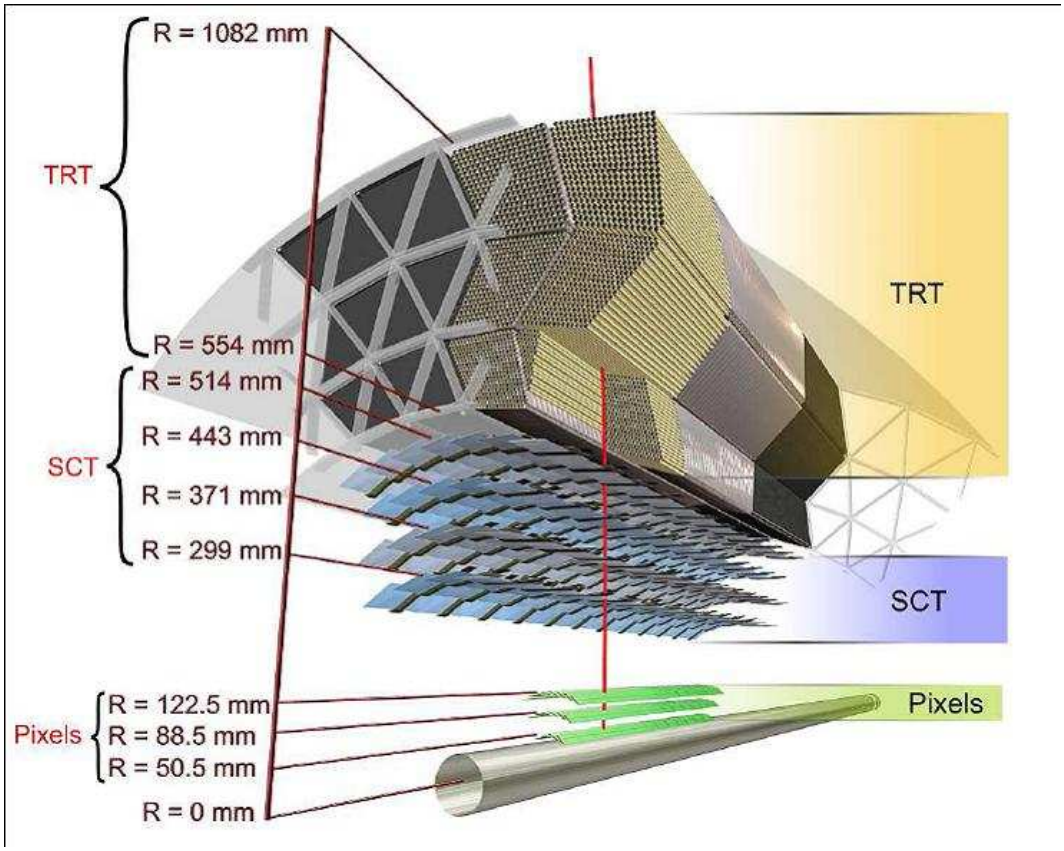

Figure 1.4. Cut-away view of the ATLAS inner detector.

It is a semiconductor detector made out of wafers with very small rectangular two dimensional detection elements. The detecting material is 250 m thick silicon. The smallest unit that can be read out is a pixel (each with dimensions of 50 by 400 micrometers). A large number of such detector elements uniformly spread on a surface ensures high spatial resolution in two coordinates, in the plane of the wafer. Because of their high precision, the pixel detector are used in vertex chambers [16]. The smallest unit that can be read out is a pixel (each 50 by 400 micrometers). The pixels are organized in modules, each measuring two centimeters by six centimeters. There are in total of 1744 modules. Each module contains roughly 47,000 pixels. This makes possible extremely precise tracking very close to the interaction point [17].

The Semi-Conductor Tracker (SCT) is the middle component of the inner detector. It has a similar concept and function to the Pixel Detector but with long, narrow strips in order to assure coverage of a larger area. Each strip measures 80 micrometers by 12.6 cm. The SCT consists of 4088 modules organized in four coaxial cylindrical layers in the barrel region and in nine disk layers in the two end-caps. It covers a total area of 63 square meters.

The Transition Radiation Tracker (TRT), the outermost component of the inner detector, is a combination of a straw tracker and a transition radiation detector. It contains many small straws, each four millimeters in diameter and up to 144 cm long. In the barrel region the straws are parallel to the beam and in the forward region they are radial. Each straw is filled with gas that becomes ionized when a charged particle passes through. With this set up the TRT covers a larger volume but with a much coarser resolution than the other two detectors. The ions produce a current in a high-voltage wire running through the middle of the the straw.

The sum of the signals form many straws creates a pattern that allows the path of the particle to be determined. The detector contains also alternating materials with very different indices of refraction, causing charged particles to produce transition radiation and leave much stronger signals in each straw. The TRT has about 351,000 straws in total.

1.2.2.2. Calorimeters

The calorimeters are situated outside the solenoidal magnet that surrounds the Inner Detector. A particle entering the calorimeter generates a shower, which is a cascade of particles produced as the result of a high-energy secondaries particle interacting with dense matter. In the interaction, multiple new particles are produced, each with lesser energy; each of these then interacts in the same way, a process that continues until many low-energy particles are produced. There are two basic types of showers: electromagnetic showers are produced by a particle that interacts primarily or exclusively via the electromagnetic force (a photon or electron) and hadronic showers are produced by hadrons (nucleons and other particles made of quarks) that proceed mostly via the strong nuclear force.

There are two types of electromagnetic calorimeters: homogeneous and sampling calorimeter. In a homogeneous calorimeter the entire volume is made of the sensitive material whereas the sampling calorimeter has layers of active medium which detects the signal and passive medium that acts as an absorber. The ATLAS calorimeter is a sampling calorimeter composed of three basic calorimeter systems: electromagnetic, hadronic and forward calorimeter. All are sampling detectors with full symmetry and coverage around the beam axis.

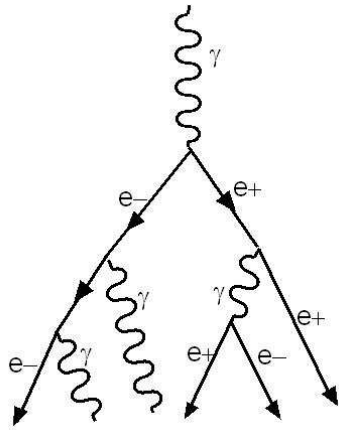

Figure 1.5. Electromagnetic shower.

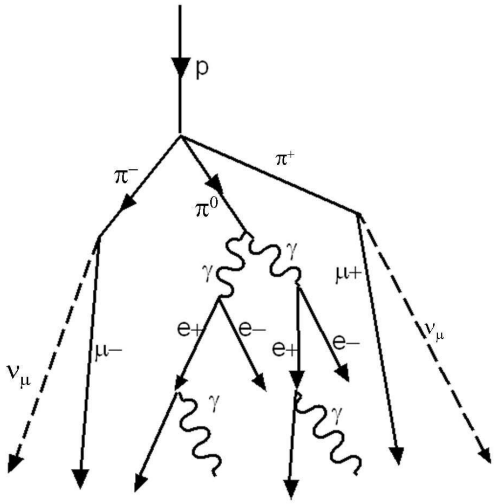

Figure 1.6. Hadronic shower.

In the electromagnetic, endcap hadronic and forward calorimeters liquid argon is used as the active detector medium because of its stability of response over time and its intrinsic radiation-hardness. A section through the calorimeters is illustrated in Fig. 1.7.

The electromagnetic (EM) calorimeter absorbs energy from particles that interact

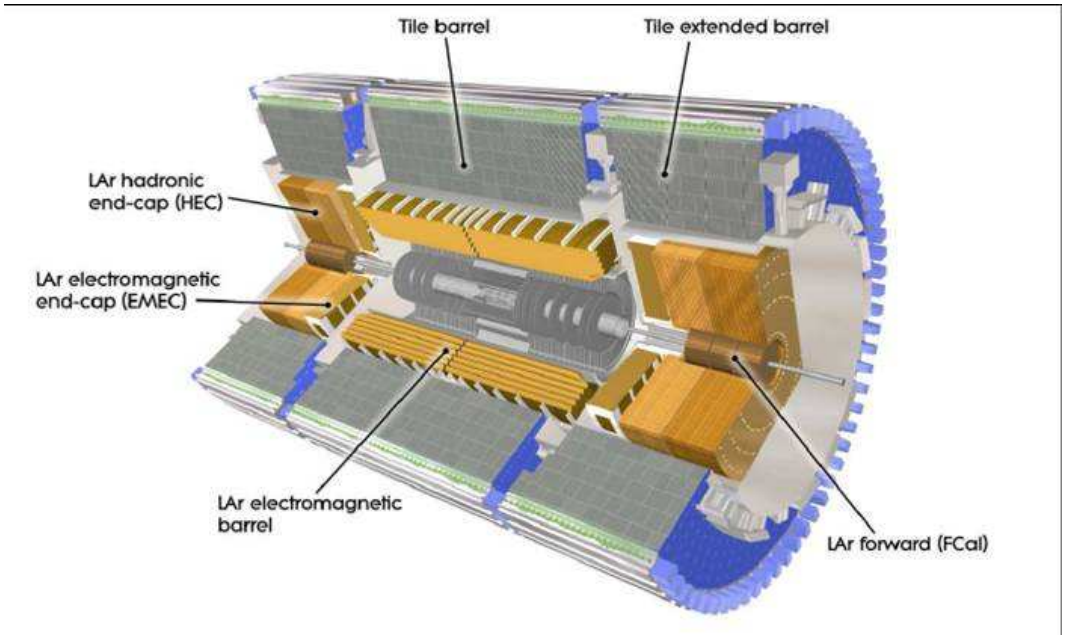

Figure 1.7. Cut-away view of the ATLAS calorimeters.

electromagnetically, which include charged particles and photons. Their detection is based on the electromagnetic shower. High energy photons or electrons incident on a thick absorber initiate an electromagnetic cascade through electron positron pair production and bremsstrahlung.

Bremsstrahlung is the process in which electromagnetic radiation(photons) is produced by the deceleration of a charged particle, such as an electron, when deflected by another charged particle, such as an atomic nucleus. Pair production refers to the creation of an electron positron pair by a photon with energy exceeding twice the rest mass of the electron. Thus more electrons and photons with lower energies are generated. These two processes will continue in turn, until the remaining particles have lower energy and then they are absorbed by atoms form the material. Fig. 1.5 shows a diagram of the process.

The ATLAS electromagnetic calorimeter is made out of lead absorber and electrode plates interleaved with liquid Argon (LAr) gaps. The lead is the energy-absorbing material and the liquid argon is the sampling material. The plates have an accordionshape geometry thus providing a hermetic and uniform ϕ coverage. Furthermore the accordion shape ensures constant amount of absorber and sampling liquid independent of the angle of incidence of the particle. For the barrel part, the amplitude of the accordion increases with radius so that each accordion plate keeps a constant ϕ. There are three electromagnetic detector parts: the electromagnetic Barel (EMB) and two Electromagnetic End Caps (EMEC). A cryostat is required around the EM calorimeter to keep it sufficiently cool [20].

The EMB is made out of two identical half-barrels. The length of each half-barrel is 3.2 m, their inner and outer diameters are 2.8 m and 4 m respectively, and each half-barrel weighs 57 tonnes. Each half-barrel is made of 1024 accordion-shaped absorbers, interleaved with readout electrodes. The electrodes are positioned in the middle of the gap by honeycomb spacers. The size of the drift gap, on each side of the electrode is 2.1 mm. The barrel calorimeter is complemented with a liquid-argon presampler detector that consists on an active layer of liquid argon, corrects for the energy loss upstream.

The EMEC calorimeters consist of two wheels, one on each side of the electromagnetic barrel. Each wheel is 63 cm thick and weighs 27 tonnes, with external and internal radii of 2098 mm and 330 mm, respectively. Each end-cap calorimeter consists itself of two co-axial wheels. Each wheel is further divided into eight wedge-shaped modules.

The hadron calorimeter absorbs energy from particles that pass through the EM calorimeter, but do interact via the strong force; these particles are primarily hadrons. The detection principle is based on the hadronic shower. This is produced by a high-energy hadron such as a nucleon or a pion. Some of these particles have electric charge, and so produce showers that are partially electromagnetic. All these particles also interact with nuclei via the strong force producing several lower-energy hadrons. The process continues, as with the electromagnetic shower, until all particles are stopped or absorbed in the material see Fig. 1.6.

The ATLAS hadronic calorimeters are: the tile calorimeter, the liquid-argon hadronic end-cap calorimeter (HEC) and the liquid-argon forward calorimeter (FCal).

The sampling medium for the Tile hadronic calorimeter is made of scintillator tiles. The absorber medium is steel. The calorimeter is divided in 3 regions; a central barrel and two extended barrels. The central barrel has a length of 5.8 m and an outer radius of 4.25 m and inner radius of 2.6 m. The tiles are 3 mm thick and the total thickness of the steel plates is 14 mm. The orientation of the scintillator tiles radially and normal to the beam line, in combination with wavelength-shifting fibre readout on the tile edges, allows for almost seamless azimuthal calorimeter coverage [21].

The hadronic end-cap calorimeter (HEC) is a copper/liquid-argon sampling calorimeter. It consists of two wheels, a front wheel (HEC1) and a rear wheel (HEC2), each wheel containing two longitudinal sections. The wheels are cylindrical with an outer radius of 2030 mm. Each of the four HEC wheels is constructed of 32 identical wedge-shaped modules. The modules of the front wheels are made of 24 copper plates, each 25 mm thick, and a 12.5 mm thick front plate. In the rear wheels, the sampling fraction is coarser with modules made of 16 copper plates, each 50 mm thick, plus a 25 mm thick front plate. The gaps in between the plates have a thickness of 8.5 mm which is maintained using a honeycomb sheet. The gap region between the barrel and the extended barrel has special modules, made of steel-scintillator sandwiches that allows to partially recover the energy lost in the crack regions between the detectors.

Because the FCal modules are located at high η, at a distance of approximately 4.7 m from the interaction point, they are exposed to high particle fluxes. This has resulted in a design with very small liquid-argon gaps to avoid ions buildup, obtained by using an electrode structure of small-diameter rods, center in tubes which are oriented parallel to the beam direction.

1.2.2.3. Muon Detector

The muon spectrometer measures the paths in a magnetic field of these heavy electron-like particles so that their momenta can be determined with high precision. It surrounds the calorimeters and extends from a radius of 4.25 m around the calorimeters out to the full radius of the detector (11 m) [19]. The muon detection is based on magnetic deflection of the muon tracks by the large toroid magnets. The toroidal magnetic field present in the muon spectrometer is produced by eight very large air-core superconducting barrel loops and two end-caps.

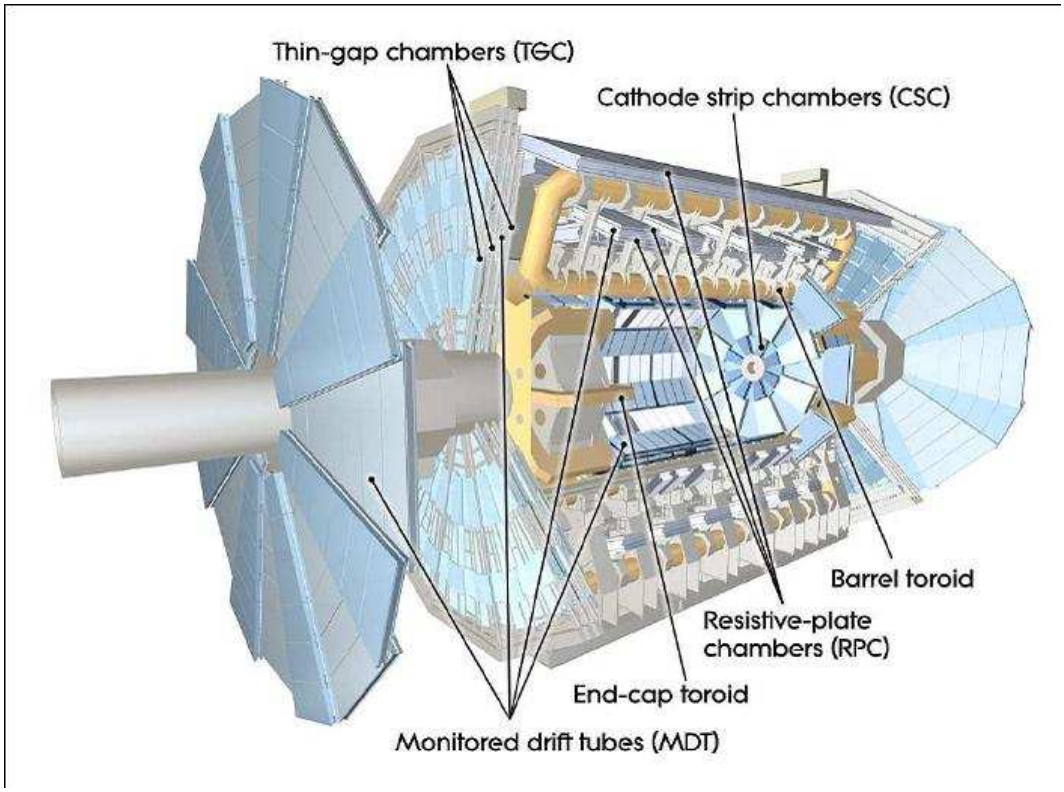

Figure 1.8. Cut-away view of the ATLAS muon system.

This magnetic field is 26 meters long and 20 meters in diameter, and it stores 1.2 gigajoules of energy. In the barrel region there are three cylindrical layers, oriented along the beam direction. In the forward region the detection layers are oriented perpendicular to the beam. The muon spectrometer has roughly one million readout channels, and its layers of detectors cover a total area of 12,000 square meters. A schematic representation of the muon system is shown if Fig. 1.7.

1.2.2.4. Trigger

With a bunch crossing frequency of 40 MHz at the LHC, the ATLAS experiment will produce a large amount of data. Since we can only store only about 200 Hz of data, we need to perform a selection of the event to be recorded. Sorting and storing the selected interesting events requires performant Triggers and Data Acquisition systems. The ATLAS trigger system has three levels: Level 1 (LVL1), Level 2 (LVL2) end Event Filter (EF). The trigger system is based on seeded event processing, that means that each trigger level starts with the decision made by the previous level and refines it by applying additional selection cuts. Fig. 1.9 shows a schematic description of the trigger levels.

The L1 trigger is a hardware trigger that selects event based on information from all of the calorimeters (electromagnetic and hadronic; barrel, end-cap and forward) and muon detector. It searches for high transverse-momentum muons, electrons, photons, τs, as well as large missing and total transverse energy. Isolation can be required, meaning that there must be a minimum angular separation from any other significant energy deposits from the same trigger event. In each event one or more Regions-of-Interest (RoIs) are defined. These are regions, within the detector, where its selection process has identified interesting features.

RoI information contains the eta and phi directions of the objects as well as a the transverse momentum thresholds that have been passed.

The thresholds are encoded in a binary word. The threshold names follow the following scheme:
(THRESHOLD TYPE)(THRESHOLD VALUE)(ADDINFO)
where THRESHOLD TYPE = type of the threshold in capital letters, THRESHOLD VALUE = threshold value in GeV, ADDINFO = additional information in capital letters. For example EM15I refers to an electromagnetic object with a transverse momentum greater than 15 GeV which is isolated.

While the trigger decision is being formed, the information for all detector channels has to be retained in pipeline memories. The LVL1 latency is the time from the proton-proton collision until the LVL1 trigger decision is made. This time interval must therefore be kept as short as possible. For the LVL1 the latency has a value of 2.2 μs.

The LVL2 trigger is software based processing only sub-regions of the detector(RoI) seeded by LVL 1 trigger. It combines tracking and calorimetry information .The average event processing time is about 40 ms.

The final step of the event selection is carried out by the EF which work similar to the LVL2 trigger. At this level the offline reconstruction algorithms are used. However, compared to the offline reconstruction, which reconstructs in the entire event, EF does only partial event reconstruction within the Level-2 RoI's. Its latency is of the order of a few seconds.

The LVL2 and EF together are called High-Level Trigger (HLT). Practically the HLT starts from the RoIs delivered by the L1 trigger and applies trigger decisions in a series of steps called a "trigger chain", each refining the preexisting information.

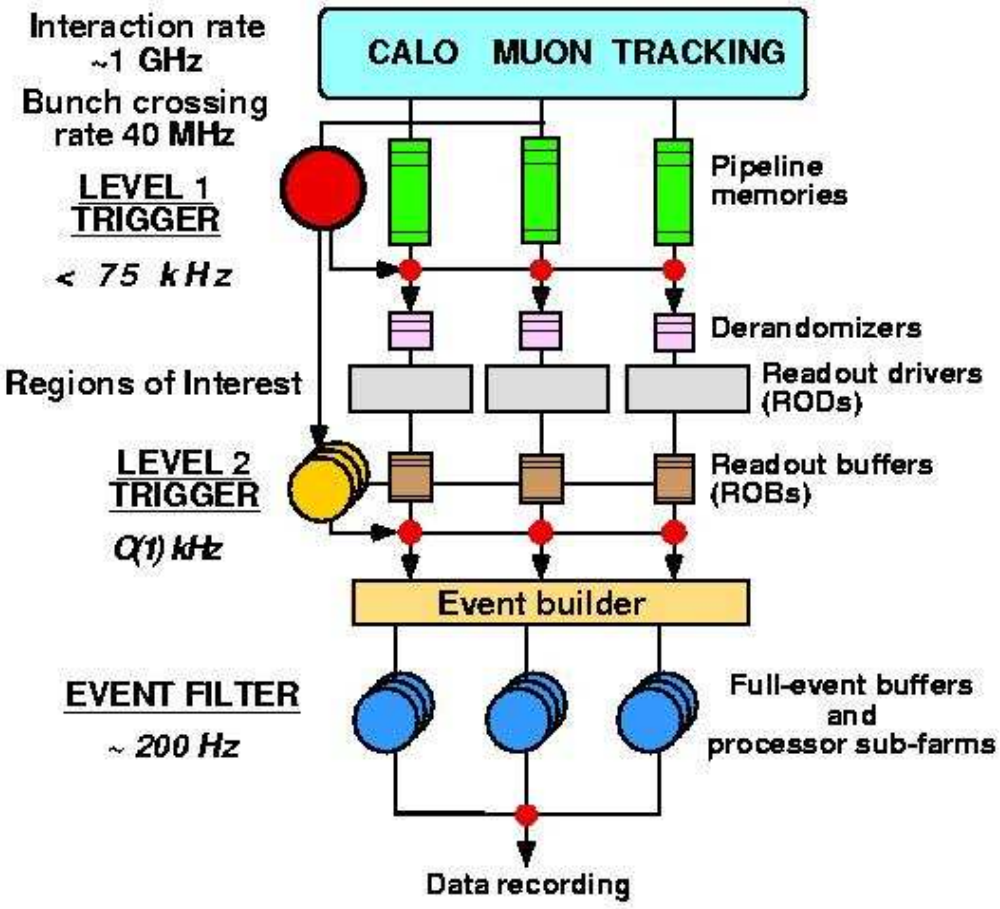

Figure 1.9. ATLAS trigger system.

The combination of trigger elements in each step that could lead to a positive trigger decision is called a "trigger signature". The decision is made by using extraction algorithms that request detector data from within the RoI and attempt to identify specific features, like a track or a calorimeter cluster. Subsequently, a hypothesis algorithm determines whether the identified feature meets the signature's criteria (such as a shower shape, track-cluster match or ET threshold) necessary to continue. With this set up, events can be rejected early at any intermediate step if no signatures remain viable.

The ATLAS trigger needs to reduce the incoming interaction rate of approximatively 1 GHz by a factor of 10^7 in order to have 200 Hz written to mass storage. This trigger setup ensures efficient background rejection while maintaining excellent selection efficiency for rare signals.

Chapter 2

HIGGS DALITZ DECAY

2.1. The Higgs boson

Symmetry has always played an important role in theoretical physics. Symmetry implies invariance. All the conservation laws of physics are related to the principles of invariance [22]. There are *Global Symmetries* in which the symmetry transformation is independent of space and time, and *Local Symmetries* or *Gauge Symmetries* for which the transformation equation is space-time dependent. The *Gauge Symmetries* are used to generate dynamics, the gauge interactions. The mathematical language for symmetry is the group theory. A group is a set of elements (*a,b,c,...*) with a multiplication law so that if a and b are elements of the group they satisfy the following properties:

- **Closure**: If $c = ab$ then c is an element of the group.
- **Associativity**:For any *a,b,c* we have *a(bc) = (ab)c*.
- **Identity**: Exists an element e such that $ea = ae = a$ for any a.
- **Inverse**: For every a exists an element a^{-1} such that $aa^{-1} = a^{-1}a = e$.

If the multiplication law is also **Commutative**: $ab = ba$ then the group is called Abelian Group.

The Unitary group, U(n) is a set of $n \times n$ unitary matrices:

$$UU^{+} = U^{+}U = I \tag{2.1}$$

where U^{+} is the conjugate transpose of U and I is the identity element of the group. For n = 1 we have the U(1)unitary group which is an Abelian group that consists of 1×1 unitary matrices, like phase transformations $e^{i\theta}$. It is the symmetry group associated with QED.

The group of $n \times n$ unitary matrices with unit determinant is called Special Unitary group, SU(n). In this case the matrices need to satisfy the relation:

$$detA = 1 \tag{2.2}$$

The group of isospin invariance is SU(2)and the SU(3) group is used to describe the symmetry based on three-quark flavors as well as three-quark color of the theory of the strong interactions known as QCD (Quantum Chromodynamics). In the language of group theory, the product $SU(3) \times SU(2) \times U(1)$, represents the underlying symmetry of the SM. This is equivalent to saying the SM incorporates the symmetries representing the electroweak theory (SU(2),U(1)) and QCD (SU(3)).

The Higgs mechanism [7] has been introduced into the Standard Model [3, 4, 5] to explain electroweak symmetry breaking and the masses of the fundamental particles. For a brief, intuitive description of the Higgs mechanism [23] consider a U(1) gauge theory with a single gauge field, the photon.

The Lagrangian in this case is:

$$L = -\frac{1}{4} F_{\mu\nu} F^{\mu\nu} \tag{2.3}$$

with $F_{\mu\nu} = \partial_\nu A_\mu - \partial_\mu A_\nu$ the field strength tensor and A_ν is the gauge field. This Lagrangian is invariant under the transformation $A_\mu(x) \rightarrow A_\mu(x) - \partial_\mu \eta(x)$ for any η and x, thus satisfying the local U(1) gauge invariance. If we add a mass term for the photon in the Lagrangian it becomes:

$$L = -\frac{1}{4} F_{\mu\nu} F^{\mu\nu} + \frac{1}{2} m^2 A_\mu A^\nu \tag{2.4}$$

In this case the gauge invariance is broken. So the U(1) gauge invariance requires for the photon to be massless.

The same procedure is applied for a complex scalar field with charge e which couples to the photon. In this case the Lagrangian is:

$$L = -\frac{1}{4} F_{\mu\nu} F^{\mu\nu} + |D_\mu \phi|^2 - V(\phi) \tag{2.5}$$

with

$$D_\mu = \partial_\mu - ieA_\mu \tag{2.6}$$

$$V(\phi) = \mu^2 |\phi|^2 + \lambda (|\phi|^2)^2 \tag{2.7}$$

The potential $V(\phi)$ is a renormalizable potential allowed by the U(1) gauge symmetry. Following the idea that a Gauge Symmetry is a local manifestation of a Global Symmetry, this Lagrangian has to be invariant under a global U(1) rotation $\phi \rightarrow e^{i\theta}\phi$ as well as under local gauge transformations. So the Lagrangian needs to be invariant under the transformations:

$$\phi(x) \rightarrow e^{i\eta(x)}\phi(x) \tag{2.8}$$

$$A_\mu(x) \rightarrow A_\mu(x) - \partial_\mu \eta(x) \tag{2.9}$$

There are two scenarios. When $\mu^2 > 0$ the symmetry is preserved. The vacuum

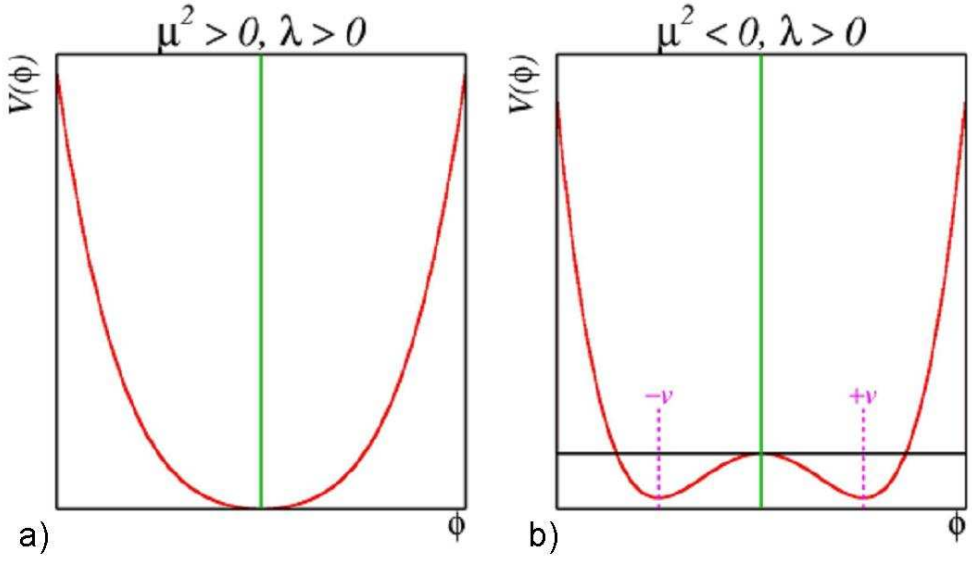

Figure 2.1. The shape of the potential in the case: a) $\mu^2 > 0$ and b) $\mu^2 < 0$.

state, which is obtained for the ϕ that minimizes the potential $V(\phi)$, has a zero value $\phi = 0$ and potential has the shape shown in fig. 2.1(a). This describes the quantum electrodynamics with a massless photon and a charged scalar field ϕ with mass μ.

If $\mu^2 < 0$ the potential can be rewritten as:

$$V(\phi) = -\mu^2|\phi|^2 + \lambda(|\phi|^2)^2 \tag{2.10}$$

This potential has the "mexican hat" shape shown in fig. 2.1(b). The minimum energy state is not at zero but at $\phi = \pm\sqrt{\frac{-\mu^2}{\lambda}} \equiv v$. The existence of this non zero vacuum expectation value (VEV) clearly breaks the U(1) global symmetry. To determine the spectrum in the region of minimum, consider a small perturbation $\eta(x)$ at the minimum value and expand around $\eta = 0$:

$$\phi(x) = \ v + \eta(x) \tag{2.11}$$

The fact that the same expansion when done around the negative minimum (-v) would result in the same physics generates the term of spontaneous symmetry breaking (there is no preferential direction). Using eq.(2.10) and eq.(2.11) the Lagrangian becomes:

$$L = \frac{1}{2}(\partial_\mu\eta\partial^\mu\eta) - (\lambda v^2\eta^3 + \lambda v\eta^3 + \frac{1}{4}\lambda\eta^4) + const \tag{2.12}$$

The result, instead of being the Lagrangian of the field ϕ now is the Lagrangian of the perturbation η.

This new Lagrangian describes the Higgs particle with mass $m^2 = 2\lambda v^2 = -2\mu^2$.

The Higgs boson is the quantum component of the Higgs field, a field imbedded in all space that has a non-zero vacuum expectation value. The gauge bosons and all fermions get their masses by interacting with this field. In the Standard Model, the Higgs field is a scalar field that means it requires the existence of a spin zero Higgs boson. The Higgs boson also has no charge and it is its own antiparticle.

The theoretical properties of the Standard Model Higgs boson have been extensively studied [24] including the production mechanisms, couplings and most of its major decays. The mass of the Higgs boson remains as an only free parameter. If the mass of the Higgs boson is between 115 and 180 GeV, then the Standard Model can be valid at energy scales all the way up to the Planck scale (10^{16} TeV) [25].

Many theorists predict the existence of new physics beyond the Standard Model. The Supersymmetric (SUSY) extensions to SM are of interest, since they provide a consistent framework for the unification of the gauge interactions at a high-energy scale[26]. Moreover, their predictions are compatible with existing high-precision data. The Minimal Supersymmetric Standard Model (MSSM) (reviewed in reference [27] and [24]) is the SUSY extension of the SM with minimal new particle content. This model predicts three neutral and two charged Higgs bosons. The lightest of the neutral Higgs bosons is predicted to have its mass of about 135 GeV.

Although the mass of the Higgs boson is an arbitrary parameter in the Standard Model and may have any value, the global fits to the numerous data on electroweak processes show a strong preference for the low mass of the Higgs. In fig. 2.2 the χ^2 for a global fit to electroweak data is shown as a function of the Higgs mass [28]. The shaded part of the plot indicates the region excluded by direct searches for the Higgs boson.

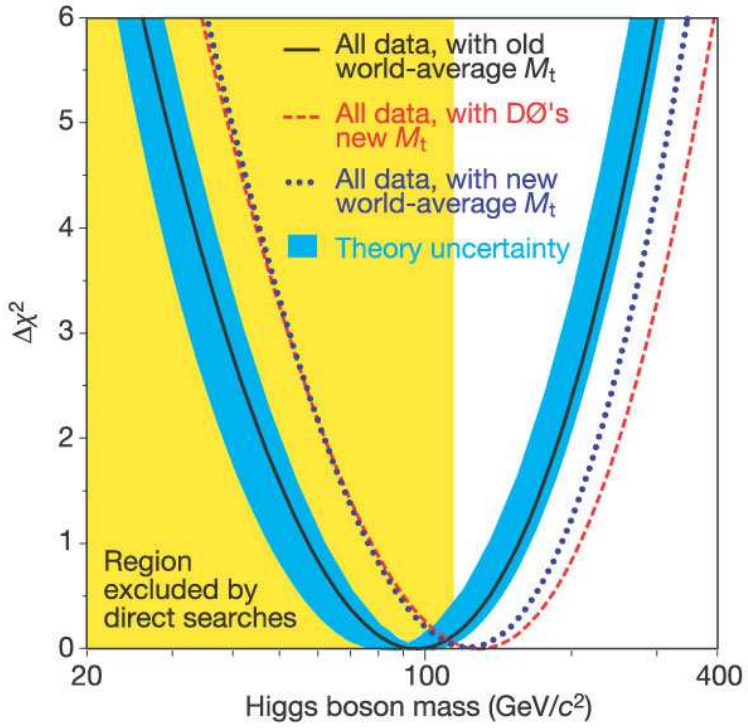

Figure 2.2. The χ^2 for a global fit to electroweak data as a function of the Higgs mass.

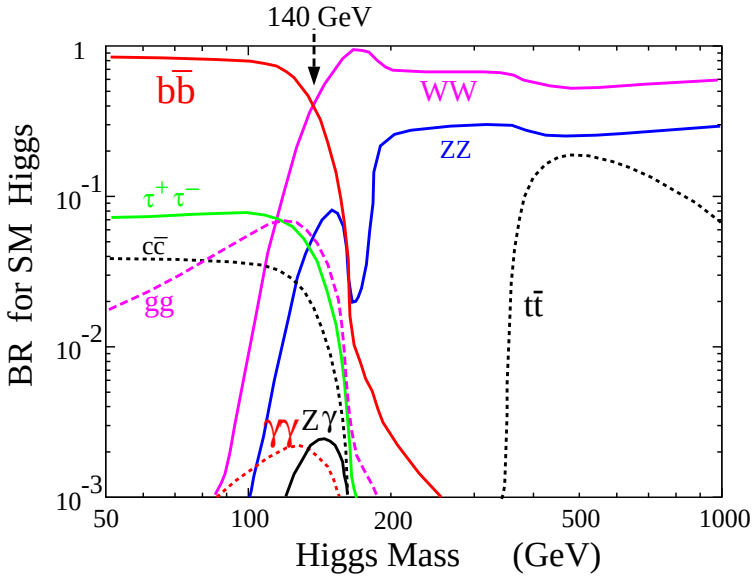

Figure 2.3. Branching ratios for different decay channels of the Higgs boson as a function of the Higgs mass.

Past searches have not been successful in finding the Higgs boson, but a lower limit on the mass - $m_H > 114.4$ GeV at 95 %CL - has been established in the LEP experiments [29]. From the fit, a relatively light value for the Higgs mass is favored. The current best fit value is $m_H < 186$ GeV at 95 $\%CL$.

Low mass Higgs will decay predominantly to a pair of fermions. The dominant branching ratio fractions are shown in Fig. 2.3, including all charged leptons and quarks except the top quark, or a pair of bosons (γ, $W^{\pm}$, Z). The identification of a Higgs particle in the mass region from 80 GeV to 130 GeV will be a challenge for the LHC. The dominant decay will be $H \rightarrow b\bar{b}$ but with the large background of QCD-jets this channel will be difficult to distinguish from the background. In Fig. 2.4 are shown the cross-sections for the SM background processes.

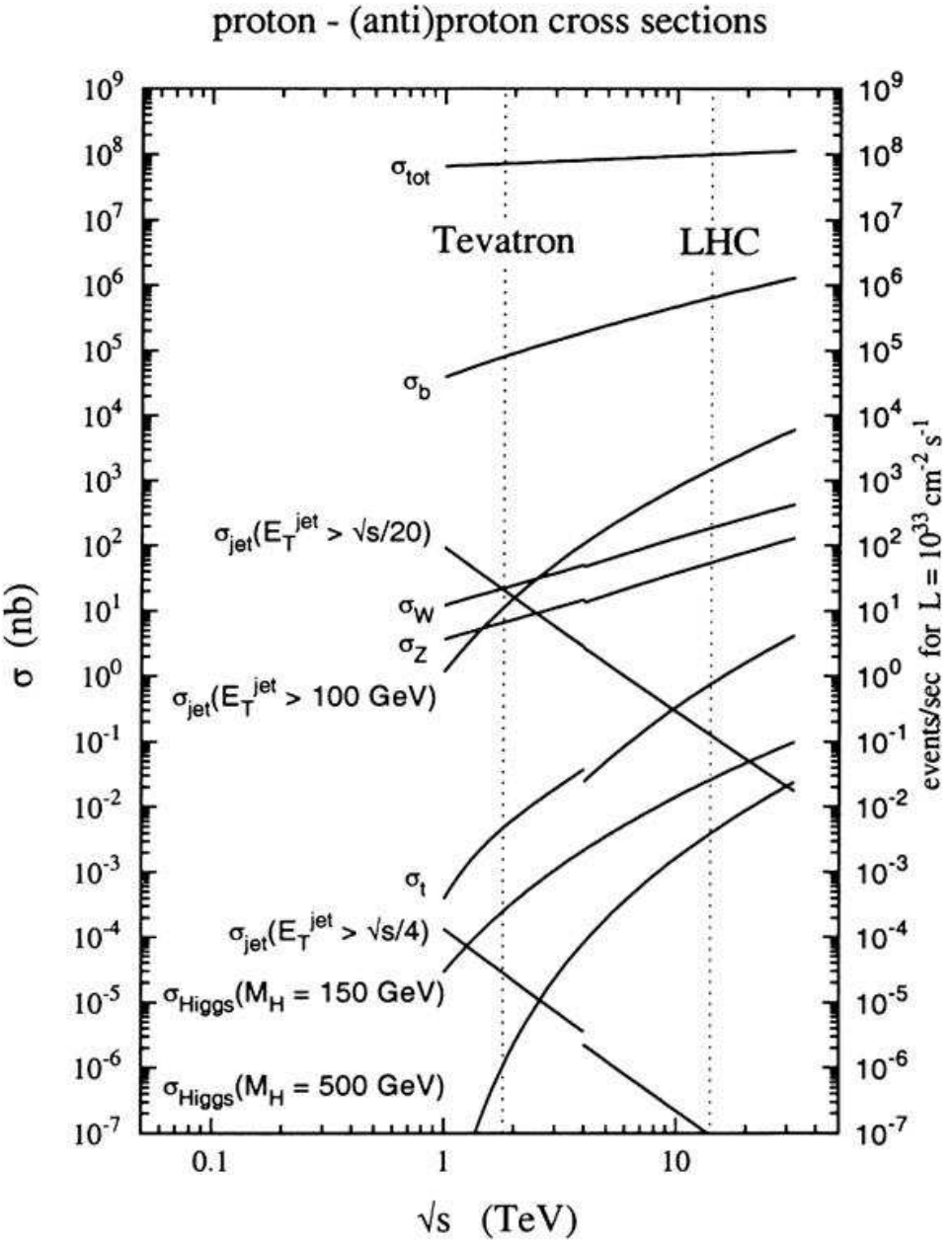

Figure 2.4. Cross sections for the Standard Model processes.

Once the center-of-mass energy exceeds the top-quark pair threshold, this process also contributes as one of the main backgrounds.

One of the most promising channels for the discovery of the Higgs boson is its decay $H \rightarrow \gamma\gamma$. This decay, to two photons, has a relatively small branching fraction of about 10^{-3} that falls rapidly with increasing Higgs mass making this decay mode useful only in the region 80 GeV $< m_H <$ 130 GeV. In spite of a small branching fraction, this decay represents a "golden discovery channel" because it is the Higgs resonance in the $\gamma\gamma$ invariant mass is easy to distinguish from the very small background. The main irreducible background comes from QCD processes of quark-antiquark annihilation ($q\overline{q} \rightarrow \gamma\gamma$) and gluon-gluon fusion ($gg \rightarrow \gamma\gamma$). This background is expected to be low for $\gamma\gamma$ mass range below $M_{\gamma\gamma} < 200$ GeV . For $M_H = 110$ GeV the ATLAS collaboration estimates a ratio [32]:

$$\frac{Signal}{\sqrt{Background}} \sim 9.0 \tag{2.13}$$

This important characteristic has been used as a benchmark in optimization of the ATLAS and CMS detectors and in estimates of the Higgs discovery potential.

2.2. The Higgs Dalitz decay

Internal photon conversion is by definition the decay of a virtual off-shell photon into electron-positron pair in the absence of matter. The process is also called Dalitz decay after the name of the physicist R.H Dalitz who was first to describe this process in the decay of the neutral pion [33]. While studying the π^0 decay he noticed that most of the time the π^0 decayed to two photons.

Fig. 2.5 shows the Feynman diagram for this process. In some rare instances though, that occurred only with a frequency of only 1.18 % ,the π^0 decayed into a photon and an electron positron pair. The Feynman diagram for this rare decay is shown in Fig. 2.6.

In SM, the Higgs particle is a neutral scalar boson. Its spin and decay character-

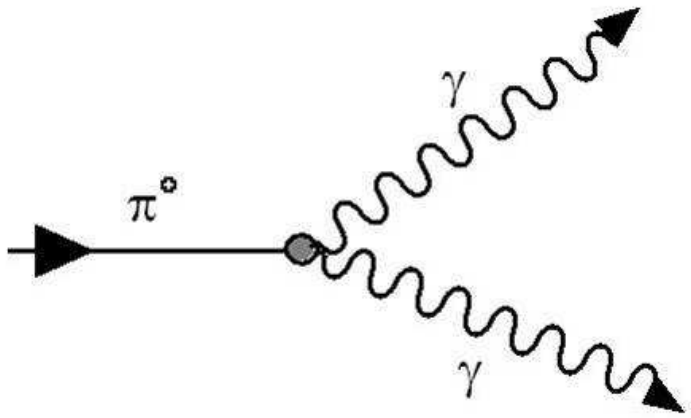

Figure 2.5. The Feynman diagram for the π^0 decay to two photons

istics are similar to that of the neutral pion with the only difference being the higher mass. It is then possible that the Higgs decay into two photons proceeds via the internal conversion process analogous to the Dalitz decay of a neutral pion. Fig. 2.7 illustrates the Feynman diagram for the Higgs Dalitz decay process.

The main difference between the π^0 Dalitz decay and the Higgs Dalitz decay is that in the Higgs case, the higher mass of the Higgs boson results in more energetic decay photons than for the π^0 case. Since photon couples to all charged particles via electromagnetic interactions, higher energy of the photons allows for higher masses of the decay products.

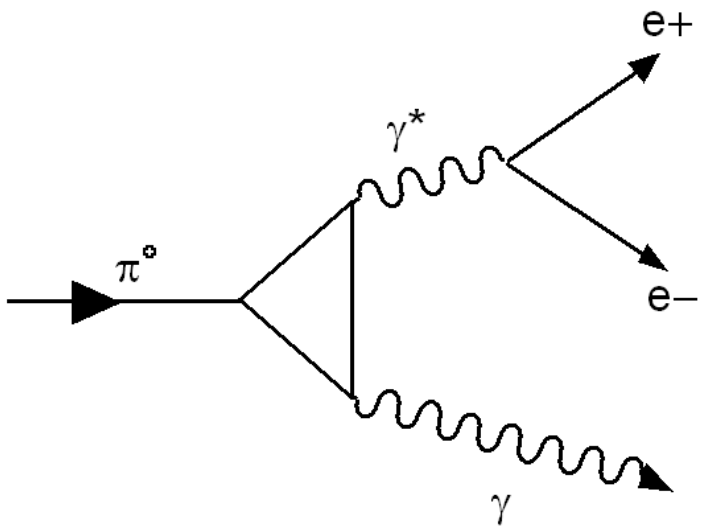

Figure 2.6. The Feynman diagram for the π^0 Dalitz decay

The mass of the virtual photon can range up to a value of the mass of the Higgs so in contrast to the case of a neutral pion, the choice of the fermion type is not limited to electrons only but will include all charged leptons and all quarks allowed by the kinematics: electrons, muons and tau leptons and up, down, strange, charm and bottom quarks. For higher Higgs masses the top quark is also allowed. In the Feynman diagram shown in Fig. 2.7, f refers to all energetically allowed fermions.

Since the photon is massless there is no direct coupling between the SM Higgs and the photon. However, the decay is possible through loop processes with either fermions or bosons in the triangular loop. The dominant process will be the virtual top/anti-top quark pair or a W boson because the couplings of the Higgs to up or down quarks or leptons are very small, due to the small masses of these particles.

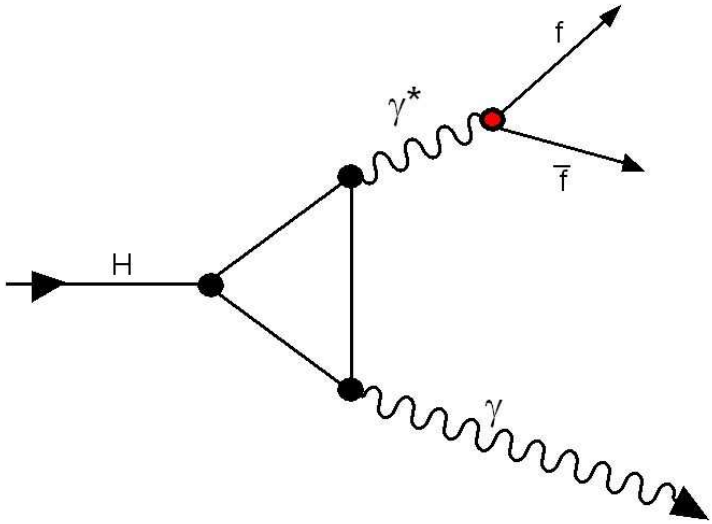

Figure 2.7. The Feynman diagram for the Higgs decay with internal conversion

In the next chapter we proceed to the calculation of the Higgs Dalitz decay branching ratio with respect to the Higgs to gamma gamma process following the same procedure as for the π^0 Dalitz decay calculation.

2.3. Correction to the Higgs to gamma gamma branching ratio

The Dalitz decay process was first studied systematically by Kroll and Wada [34] in 1955. It was later reevaluated in much more details by Miyazaki and Takasugi [35] in 1973. In their work they calculate the fraction of the neutral pion decay rates into $\gamma e^+ e^-$ to the overall rate for the decay to $\gamma\gamma$.

For the $\pi^0 \to \gamma\gamma$ the decay width, Γ, is [35]:

$$\Gamma(\pi^0 \to \gamma\gamma) = \frac{|f|^2\mu}{16\pi} \tag{2.14}$$

where $f = f(k_1^2, k_2^2)$ is the form factor dependent on the momenta of the two photons, k_1 and k_2, and μ is the π^0 mass. The $\pi^0 \to \gamma e^+e^-$ has a decay width expressed as:

$$\frac{d\Gamma(\pi^0 \to \gamma e^+e^-)}{dq} = \frac{|f|^2\mu\alpha_0}{12\pi}(1 - \frac{q^2}{\mu^2})^3(1 - \frac{4m_e^2}{q^2})^{1/2}(1 + \frac{2m_e^2}{q^2}) \tag{2.15}$$

In this case, $\alpha_0 = 1/137$ is the electromagnetic coupling constant, q denotes momentum of the virtual photon and m_e is the mass of the electron. The range of q is given by $2m_e < q < \mu$. The conversion rate is introduced as:

$$\rho = \frac{\Gamma(\pi^0 \to \gamma e^+e^-)}{\Gamma(\pi^0 \to \gamma\gamma)} \tag{2.16}$$

By combining eq.(2.16) and (eq. 2.17), the resulting expression for ρ is given by an integral over phase space for each final state leptons:

$$\rho = \frac{4\alpha_0}{3\pi}\int_{2m_e}^{\mu}\left(1 - \frac{q^2}{\mu^2}\right)^3\left(1 - \frac{4m_e^2}{q^2}\right)^{1/2}\left(1 + \frac{2m_e^2}{q^2}\right)\frac{dq}{q}. \tag{2.17}$$

The resulting theoretical value for this ratio, ρ, is found to have the numerical value of 0.0118 which is in excellent agreement with the experimental value [29].

To evaluate the rate of internal conversions for the $H \to \gamma\gamma$ decay we follow the procedure used for the evaluation of the π^0 Dalitz decay and calculate the fraction:

$$\rho_H = \frac{\Gamma(H \to \gamma f \overline{f})}{\Gamma(H \to \gamma\gamma)} \tag{2.18}$$

There are a few correction that need to be taken into account when estimating the ratio in this case. Because of the higher energy range we need to use the running effective coupling of the virtual photon to the fermion pair evaluated at the mass of the virtual photon, q [36]:

$$\alpha_{eff}(q^2) = \frac{\alpha_0}{1 - \frac{\alpha_o}{3\pi} \sum_i e_i^2 \Theta(q^2 - 4m_i) \ln\left(\frac{q^2}{4m_i}\right)} \tag{2.19}$$

where $\alpha_0 = 1/137$, e_i is the charge and m_i the mass of the fermion in Θ the Callan-Symanzik beta function,Θ [37] [38]. For example for energies up to a Higgs mass of 120 GeV, we could have electrons, muons, taus, up, down, strange and bottom quarks in the function so the coupling becomes:

$$\alpha_{eff}(q^2) = \frac{\alpha_0}{1 - \frac{\alpha_o}{3\pi}[\ln(\frac{q^2}{4m_e}) + \ln(\frac{q^2}{4m_\mu}) + (\frac{2}{3})^2 \ln(\frac{q^2}{4m_u}) + (\frac{-1}{3})^2 \ln(\frac{q^2}{4m_d}) + (\frac{-1}{3})^2 \ln(\frac{q^2}{4m_s})]} \tag{2.20}$$

Since $\alpha_{eff}(q^2)$ contains a step function $\Theta(q^2 - 4m_i)$, it must be integrated in steps across all of the particle mass thresholds as q varies from $2m_f$ to m_H.

With all these considerations included, in the case of leptons as final decay product of the virtual photon, the ratio ρ_l is given by:

$$\rho_l = \frac{4}{3\pi}\int_{2m_l}^{m_H} \alpha_{eff}(q^2)\left(1-\frac{q^2}{m_H^2}\right)^3\left(1-\frac{4m_l^2}{q^2}\right)^{1/2}\left(1+\frac{2m_l^2}{q^2}\right)\frac{dq}{q} \tag{2.21}$$

where m_l is the lepton mass.

In the case of quarks we need to take into account the color factors for the quarks and the charge dependence of the couplings . The modification of the eq.(2.23) takes the form:

$$\rho_q = 3(e_i)^2\frac{4}{3\pi}\int_{2m_q}^{m_H} \alpha_{eff}(q^2)\left(1-\frac{q^2}{m_H^2}\right)^3\left(1-\frac{4m_q^2}{q^2}\right)^{1/2}\left(1+\frac{2m_q^2}{q^2}\right)\frac{dq}{q} \tag{2.22}$$

In this equation m_q represents the quark mass, e_i is the fractional charge of the quarks and the factor 3 accounts for the three possible quarks colors. We assume the lower limit of the mass integration to be equal to the lowest mass of a physical hadron produced in the decay, i.e., pion mass for the u and d quarks and kaon mass for the strange quark; we use the particle Data Group values for the masses of c and b quarks [29]. The corresponding partial width is:

$$\Gamma_i = \rho_i \times Br(H \to \gamma\gamma) \times \Gamma_{tot} \tag{2.23}$$

where Γ_{tot} denotes the total width. The results of the evaluation of this ratio for three values of the Higgs mass are listed in Tables 2.1 , 2.2 and 2.3 . In Fig 2.8 we show the shift in the branching fraction value for the $H \to \gamma\gamma$ due to the Higgs Dalitz decays. As can be seen, in the region just above the limit of the present day observation, the total Dalitz decay rate of the neutral Higgs is about 10% of the $H \to \gamma\gamma$ branching fraction.

Table 2.1. Values of the ratio ρ and branching fractions for the Higgs with mass $m_H = 120$ GeV decaying to two photons with single internal conversions.

$HiggsMass$	$m_H = 120$ GeV	
$Channel$	ρ	$BranchingFraction$
$H \to e^+e^-\gamma$	0.0332	71.38×10^{-6}
$H \to \mu^+\mu^-\gamma$	0.0167	35.90×10^{-6}
$H \to \tau^+\tau^-\gamma$	0.0078	16.77×10^{-6}
$H \to u\bar{u}\gamma$	0.0211	45.36×10^{-6}
$H \to d\bar{d}\gamma$	0.0053	11.39×10^{-6}
$H \to s\bar{s}\gamma$	0.0040	8.38×10^{-6}
$H \to c\bar{c}\gamma$	0.0123	26.44×10^{-6}
$H \to b\bar{b}\gamma$	0.0018	3.87×10^{-6}
	0.1022	219×10^{-6}

Table 2.2. Values of the ratio ρ and branching fractions for the Higgs with mass $m_H = 150$ GeV decaying to two photons with single internal conversions.

$HiggsMass$	$m_H = 150$ GeV	
$Channel$	ρ	$BranchingFraction$
$H \to e^+e^-\gamma$	0.0340	47.12×10^{-6}
$H \to \mu^+\mu^-\gamma$	0.0174	24.19×10^{-6}
$H \to \tau^+\tau^-\gamma$	0.0086	11.81×10^{-6}
$H \to u\bar{u}\gamma$	0.0220	30.58×10^{-6}
$H \to d\bar{d}\gamma$	0.0055	7.64×10^{-6}
$H \to s\bar{s}\gamma$	0.0042	5.83×10^{-6}
$H \to c\bar{c}\gamma$	0.0132	18.35×10^{-6}
$H \to b\bar{b}\gamma$	0.0020	2.78×10^{-6}
	0.1070	148×10^{-6}

Table 2.3. Values of the ratio ρ and branching fractions for the Higgs with mass $m_H = 180$ GeV decaying to two photons with single internal conversions.

$HiggsMass$	$m_H = 180$ GeV	
$Channel$	ρ	$BranchingFraction$
$H \to e^+e^-\gamma$	0.0346	3.4×10^{-6}
$H \to \mu^+\mu^-\gamma$	0.0180	1.79×10^{-6}
$H \to \tau^+\tau^-\gamma$	0.0091	0.91×10^{-6}
$H \to u\bar{u}\gamma$	0.0229	2.28×10^{-6}
$H \to d\bar{d}\gamma$	0.0057	0.57×10^{-6}
$H \to s\bar{s}\gamma$	0.0044	0.44×10^{-6}
$H \to c\bar{c}\gamma$	0.0140	1.39×10^{-6}
$H \to b\bar{b}\gamma$	0.0022	0.22×10^{-6}
	0.1110	11×10^{-6}

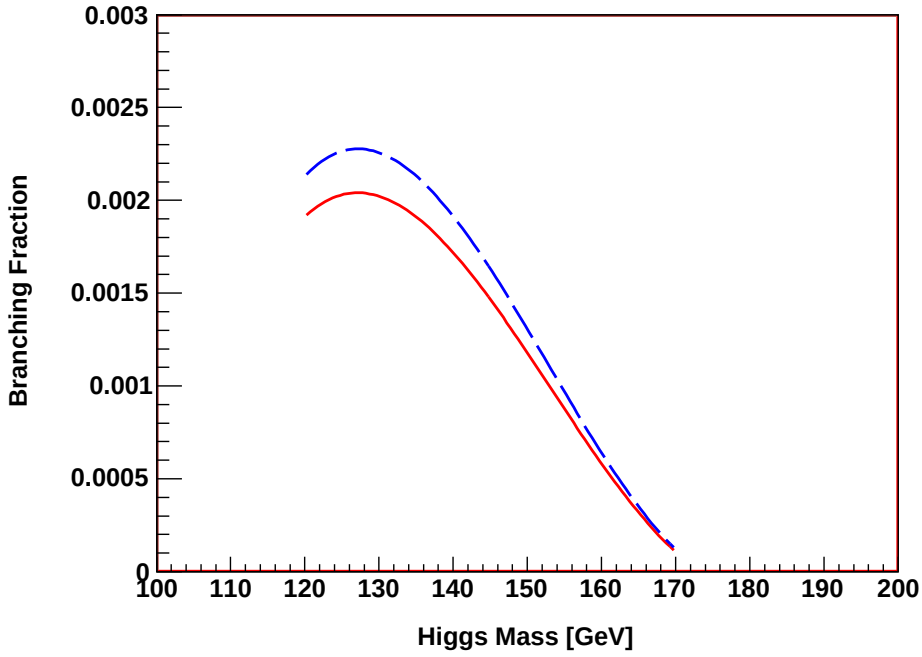

Figure 2.8. The shift in the Branching Fraction $Br(H \rightarrow \gamma\gamma)$ due to the Dalitz decay correction. The dotted line represents the Branching Fraction without the Dalitz decay corrections and the solid line takes into account the corrections

2.4. Conclusion

The search for the Higgs boson has been one of the main motivations for the construction of the Large Hadron Collider (LHC). The potential for the Higgs discovery was the object of a detailed assessment study that was done by both the ATLAS [39] team, and the CMS [40] teams. According to their results, it is expected that the Standard Model Higgs can be discovered if its mass ranges from 80 GeV/c^2 up to 1 TeV/c^2 . The Higgs boson mass can be measured with 1 % precision across the entire mass range.

After the discovery of a Higgs particle it will be important to measure the rate of its decay into several decay channels to check if the coupling strength is indeed proportional to the mass of the fermions, as predicted by the Standard Model. From this point of view, the correct estimation the branching fractions is of extreme importance.

This study shows that there are new Higgs decay channels, previously neglected by the literature that proceed via the Higgs Dalitz decay mechanism. Even though the cross sections for these processes are very low making them unsuitable for direct discovery channels, they impose corrections to the branching fraction for the Higgs to gamma gamma process that is the "golden channel" for Higgs discovery. All LHC experiments should include the corresponding correction in their respective Monte Carlo programs.

This work has been published in *Physical Reviews* **D76** 057301 (2007) [41].

Chapter 3

MONTE CARLO STUDIES ON METHODS TO SEARCH FOR DIRAC MAGNETIC MONOPOLES

3.1. History of magnetic monopoles and the present status

Classical Electrodynamics is regarded as the best established theory of physics. Maxwell's equations and Lorentz law of forces describe the interactions of systems of electromagnetic fields and charged particles. In these equations there are two fields, the electric field **E** and the magnetic field **B**, and only one charge, the electric charge. Fundamentally, all electromagnetic effects can be derived from a set of differential equations known as the Maxwell equations. For a vacuum without sources they have the following form [42]:

$$\nabla \cdot \mathbf{E} = 0, \tag{3.1}$$

$$\nabla \cdot \mathbf{B} = 0, \tag{3.2}$$

$$\nabla \times \mathbf{E} + \frac{1}{c}\frac{\partial \mathbf{B}}{\partial t} = 0, \tag{3.3}$$

$$\nabla \times \mathbf{B} - \frac{1}{c}\frac{\partial \mathbf{E}}{\partial t} = 0, \tag{3.4}$$

In equations (3.1) - (3.4), there is a striking symmetry between electric and magnetic charges, more precisely the electric and magnetic fields. The equations are invariant under the electromagnetic duality transformations which refers to the exchange of:

$$\mathbf{E} \longrightarrow \mathbf{B} \tag{3.5}$$

$$\mathbf{B} \longrightarrow -\mathbf{E} \tag{3.6}$$

In the presence of an electric charge density ρ_e and an electric current density $\mathbf{J}_e$, Maxwell equations are:

$$\nabla \cdot \mathbf{E} = 4\pi\rho_e, \tag{3.7}$$

$$\nabla \cdot \mathbf{B} = 0, \tag{3.8}$$

$$\nabla \times \mathbf{E} + \frac{1}{c}\frac{\partial \mathbf{B}}{\partial t} = 0, \tag{3.9}$$

$$\nabla \times \mathbf{B} - \frac{1}{c}\frac{\partial \mathbf{E}}{\partial t} = \frac{4\pi}{c}\mathbf{J}_e \tag{3.10}$$

In this case, the equations are no longer symmetric under the electromagnetic duality transformations; we say that the absence of magnetically charged particles breaks the symmetry.

To restore symmetry we need another particle called by the literature the magnetic monopole. Experimentally, such a particle has never been observed [25]. This lack of experimental evidence was interpreted as a proof of their non-existence.

If we assume that magnetic monopoles might exist but we are just not able to detect them yet, we need to modify Maxwell equations by adding in the magnetic charge density ρ_m and the magnetic current $\mathbf{J}_m$:

$$\nabla \cdot \mathbf{E} = 4\pi\rho_e, \tag{3.11}$$

$$\nabla \cdot \mathbf{B} = 4\pi\rho_m, \tag{3.12}$$

$$\nabla \times \mathbf{E} + \frac{1}{c}\frac{\partial \mathbf{B}}{\partial t} = \frac{4\pi}{c}\mathbf{J}_m, \tag{3.13}$$

$$\nabla \times \mathbf{B} - \frac{1}{c}\frac{\partial \mathbf{E}}{\partial t} = \frac{4\pi}{c}\mathbf{J}_e, \tag{3.14}$$

These "new" Maxwell equations remain unmodified under the following duality transformations:

$$\mathbf{E} \to \mathbf{B}, \rho_e \to \rho_m, \mathbf{J}_e \to \mathbf{J}_m \tag{3.15}$$

$$\mathbf{B} \to -\mathbf{E}, \rho_m \to -\rho_e, \mathbf{J}_m \to -\mathbf{J}_e \tag{3.16}$$

Thus, the introduction of the concept of the magnetic monopole in Classical Electrodynamics, restores the symmetry of Maxwell equations.

In theoretical particle physics, we use relativistic quantum field theory to describe particles and their interactions. When describing the magnetic monopole in Quantum Mechanics there is one fundamental problem. In classical electrodynamics we have as basic quantities the electric and magnetic fields, but in quantum mechanics those two fields do not provide a complete description of the electromagnetic effects on the wave functions of the charged particles. We need to use another vector field called vector potential $\mathbf{A}$ and a scalar field called scalar potential ϕ. If we define the magnetic field by analogy with the electric field, we have the expression:

$$\mathbf{B} = \nabla \times \mathbf{A} \tag{3.17}$$

In addition, $\mathbf{B}$ needs to satisfy the vector identity [43]:

$$\nabla \cdot (\nabla \times \mathbf{A}) = 0 \tag{3.18}$$

Equations (3.17) and (3.18) imply that:

$$\nabla \cdot \mathbf{B} = 0 \tag{3.19}$$

But from Maxwell equations we should have:

$$\nabla \cdot \mathbf{B} = 4\pi\rho_m \tag{3.20}$$

This creates an obvious contradiction and, in the early 20-th century, it seemed that the concept of magnetic monopole had to be abandoned in order to maintain the vector potential without which we cannot describe the behavior of the electron in magnetic field [43].

In 1931 P.A.M. Dirac introduced the idea of a magnetic monopole in his paper "Quantised singularities in the electromagnetic field" [44] and then revised later, in 1948, in "The theory of magnetic monopoles" [45]. In his work, he showed that it is possible to have both magnetic monopole and vector potential in quantum mechanics. While doing this he showed that the existence of the magnetic monopole would explain the quantization of electric charge. In nature all electric charges are the multiples of the electron's charge [46]. This behavior was well documented by numerous experiments but no one could find a valid theoretical explanation for it. Dirac introduced the idea of a magnetic "Dirac" potential of the form:

$$A^D(\mathbf{r}) = -\frac{1}{2}\frac{g}{4\pi r}\left(\frac{\hat{\mathbf{n}}\times\mathbf{r}}{\mathbf{r}-\hat{\mathbf{n}}\cdot\mathbf{r}} - \frac{\hat{\mathbf{n}}\times\mathbf{r}}{\mathbf{r}+\hat{\mathbf{n}}\cdot\mathbf{r}}\right) = \frac{g}{4\pi r}\left(\frac{1-\cos\theta}{\sin\theta}\right)\hat{\phi} \tag{3.21}$$

which has a singularity along the $\hat{\mathbf{n}}$ direction. In this equation, θ is the polar angle and ϕ is the azimuthal angle and $\mathbf{r}$ is the position vector.

To understand the idea behind this construct we need to look back at equations (3.17)-(3.19). It is clear that $\mathbf{B}$ cannot be defined as $\nabla \times \mathbf{A}$ everywhere. But $\mathbf{B}$ could be defined this way everywhere but on a infinite line along the negative z-axis. This setup is similar to a field of a infinitely long and thin solenoid placed along the negative z-axis with its positive pole of strength g placed at origin.

The magnetic field for the solenoid is [23]:

$$\mathbf{B}_{Sol} = \frac{g}{4\pi r^2}\hat{\mathbf{r}} + g\theta(-z)\delta(x)\delta(y)\hat{\mathbf{z}} \tag{3.22}$$

, where $\hat{\mathbf{r}}$ is the unit vector in the radial direction and $\hat{\mathbf{z}}$ is the unit vector in the z-direction. Since this magnetic field has no sources it satisfies $\nabla \cdot \mathbf{B}_{Sol} = 0$ and it can be written as:

$$\mathbf{B}_{Sol} = \nabla \times \mathbf{A}_{Sol} \tag{3.23}$$

with:

$$\mathbf{A}_{Sol} = \frac{g}{4\pi r}(\frac{1-\cos\theta}{\sin\theta})\hat{\phi} \tag{3.24}$$

In the case of the magnetic monopole, the "Dirac" potential vector, with the $\hat{\mathbf{n}}$ in the negative z-direction, and the solenoid vector potential have similar expressions. In this case the solenoid line is called the "Dirac String". Respecting the electromagnetic duality, the magnetic field for a magnetic charge g has to have the form:

$$\mathbf{B} = \frac{g^2}{4\pi r^2}\hat{\mathbf{r}} \tag{3.25}$$

This is actually the first term in equation (3.22).

Using equations (3.23)- (3.24) the magnetic field can be redefined as:

$$\mathbf{B} = \nabla \times \mathbf{A}^D - g\theta(-z)\delta(x)\delta(y)\hat{\mathbf{z}} = \frac{g^2}{4\pi r^2}\hat{\mathbf{r}} \tag{3.26}$$

From this equation it can be seen that in order to define the magnetic field, we need a vector potential, $\mathbf{A}^D$, and a string. The string is not an observable, but just a mathematical artifact. The requirement that the physical charge should not be able to "see" the string results in the quantization of electric charge. A detailed description of the calculation is given in one of the recent reviews of the field [60]. Dirac charge quantization condition states that if we have a magnetic charge g, and an electric charge e, their product must be:

$$eg = \frac{n}{2} \tag{3.27}$$

Taking $n = 1$ the equation becomes:

$$g_D = \frac{1}{2e} = \frac{e}{2e^2} \tag{3.28}$$

but

$$\alpha_{em} = e^2 \tag{3.29}$$

where α_{em} is the electromagnetic coupling constant.

From equations (3.28) and (3.29) we have:

$$g_D = \frac{e}{2\alpha_{em}} = 68.5e \tag{3.30}$$

This value is called by the literature the "Dirac charge" and represents the elementary magnetic charge.

In spite of the lack of experimental evidence, most theories predict the existence of magnetic monopoles. Practically, any theory that tries to unify electromagnetism with other fundamental forces introduces the concept of magnetic monopole. In 1974 t'Hooft [48] and Polyakov [49] proved that in the Grand Unified Theories (GUT) of electroweak and strong interactions the magnetic monopoles are produced in the Early Universe as topological defects during phase transition. There are also Kaluza-Klein monopoles [50] that appear during the unification of the GUT interaction and gravitational interaction, monopoles in String Theory, Wu-Yang monopoles [51] and the list goes on.

Over the last several years, a lot of searches for the magnetic monopoles were conducted in different settings. The observation of a signal consistent with the passage of a single magnetic monopole in a single superconductive loop [52] initiated new interest in the topic. Physicist at high energy accelerators searched for the low mass magnetic monopoles immediately after their production or investigated the possibility of finding them trapped in the matter located around the beam interaction points [53]. These searches focused mainly on Dirac type magnetic monopoles, which are point like particles with spin 1/2 that carry the unit magnetic charge g_D. In 1998, the D0 group searched for the virtual magnetic monopoles [70] that would have a signature of highly energetic photons.

Then later in 2000 and 2004, searches were conducted by the CDF and D0 groups for magnetically charged particles trapped in the matter around the interaction point [54], [55]. GUT theories predict monopoles masses about 10^{17} GeV which are not accessible to any accelerator experiments. In this case, the searches focused on studying cosmic radiation looking for magnetic monopoles left over as relics from the Big Bang. Attempts to find magnetic monopoles trapped in exotic materials like moon rocks or old church windows were also not successful.

Unfortunately Dirac could not constrain the mass of the magnetic monopole. The mass can only be estimated based on the equality of the classical electron radius and the magnetic monopole radius [56]:

$$r_e = \frac{e^2}{m_e c^2} = r_M = \frac{g^2}{m_M c^2} \tag{3.31}$$

this gives a monopole mass of $m_M = 2.4$ GeV. This value is already excluded by many searches. The superstring model predicts monopole masses of 1 TeV and the GUT monopole can be expected to have even higher mass. Thus any mass region for magnetic monopoles remains still open. The current lower limit of mass of the Dirac magnetic monopole was set at 350 GeV by the CDF experiment at the Tevatron [57].

The Large Hadron Collider can open a new era in the search for the Dirac type magnetic monopoles because of the new energy range available that allows to search for monopoles with higher masses that were not accessible at older accelerators. If these particles are produced during highly energetic proton-proton collisions, they will leave specific signatures inside the ATLAS detector. Defining this signature is the main goal of this study.

To achieve this goal we need a reliable Monte Carlo simulations based upon our best knowledge of the monopole production mechanisms and the behavior in interaction with matter.

3.2. Monte Carlo simulation of the Magnetic Monopole

3.2.1. Generation

3.2.1.1. Cross section calculations

Monopole searches at colliders are restricted to searches for the Dirac type monopoles, assumed to be spin 1/2 particles that carry a elementary magnetic Dirac charge g_D. In proton-proton collisions, models of Dirac monopole production are mainly based on the Drell-Yan (DY) type of process in which a quark and antiquark ($q\overline{q}$) from the interacting protons annihilate to produce a monopole anti-monopole pair ($\overline{m}m$) [55], [58], [54]. In fig 3.2 is shown the Feymnman diagram for the "classical" Drell-Yan process in which a lepton-antilepton pair is produced. In the monopole Drell-Yan process, for which the Feynman diagram is shown in Fig. 3.2, the electromagnetic coupling constant at the monopole/anti-monopole vertex has been replaced by the magnetic coupling constant α_{mm}.

The field theory for the magnetic monopoles is still in a primitive stage mainly because of the large monopole coupling implied by the Dirac quantization condition that prevents the use of the perturbation theory. Thus a non-perturbative approximation must be used.

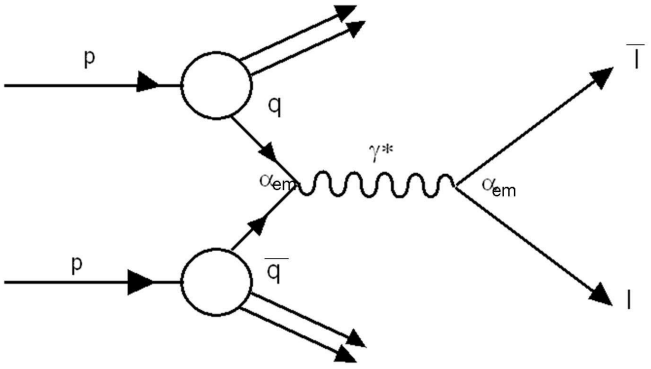

Figure 3.1. Feynman diagram for Drell-Yan

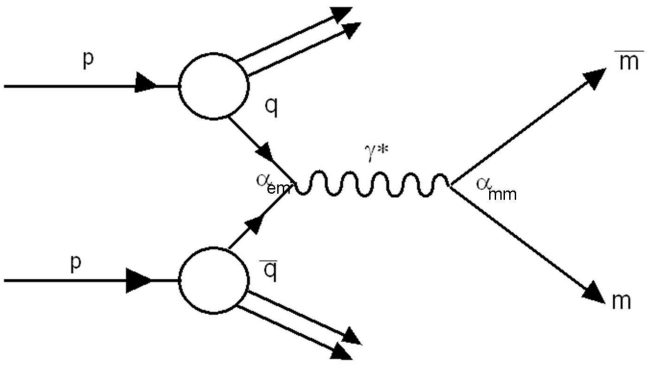

Figure 3.2. Feynman diagram for magnetic monopole Drell-Yan

If we define the magnetic monopole coupling by analogy with the electromagnetic coupling, we have:

$$\alpha_{mm} = g^2. \tag{3.32}$$

where α_{mm} is the magnetic coupling constant. Squaring the charge quantization condition, eq.(3.27) and setting $n = 1$ we have:

$$e^2 g^2 = \frac{1}{4} \Rightarrow \alpha_{em}\alpha_{mm} = \frac{1}{4}. \tag{3.33}$$

This leads to a definition of a magnetic monopole coupling constant as:

$$\alpha_{mm} = \frac{1}{4\alpha_{em}} = 34.25. \tag{3.34}$$

Because of this huge coupling constant, the perturbative calculation of the cross section fails and leaves us with a lowest order approximation as our only means to proceed.

To define a more rigorous magnetic coupling constant we follow in our study the work done by Schwinger [59] which shows that for relativistic scattering, the monopole effective charge is obtained by the substitution :

$$e \rightarrow g\beta \tag{3.35}$$

where is defined as $\beta = \frac{v}{c}$ is the velocity of the monopole. This result is obtained by comparing the cross section for electron-monopole scattering and electron-electron scattering. A detailed description is given by [60]. For small scattering angles the cross section for electron-electron scattering is:

$$\frac{d\sigma}{d\Omega} = (\frac{e^2}{2m_e v^2})^2 \frac{1}{(\theta/2)^4} \tag{3.36}$$

with m_e representing the electron mass, v its velocity and θ the scattering angle. The corresponding cross section for electron-monopole scattering is:

$$\frac{d\sigma}{d\Omega} = (\frac{1}{2m_M v})^2 (\frac{eg}{c})^2 \frac{1}{(\theta/2)^4} \tag{3.37}$$

Comparing those two formulas, the substitution $\frac{e}{v} \rightarrow \frac{g}{c}$ is evident.

The magnetic coupling constant can be defined by an analogy with the electromagnetic coupling using eq.(3.35):

$$\alpha_{em} = e^2 \tag{3.38}$$

$$\alpha_{mm} = (g\beta)^2 \tag{3.39}$$

But squaring the charge quantization condition we have:

$$e^2 g^2 = \frac{1}{4} \Rightarrow \alpha_{em} g^2 = \frac{1}{4} \tag{3.40}$$

which leads to a definition of the magnetic monopole charge as

$$g^2 = \frac{1}{4\alpha_{em}} \tag{3.41}$$

From equations (3.42) and (3.44) we obtain the magnetic coupling constant formula:

$$\alpha_{mm}(\beta) = \frac{1}{4\alpha_{em}}\beta^2 \tag{3.42}$$

In the limit $\beta \to 1$ we obtain the classical formulation presented in equation (3.34).

In the classical DY process, a lepton pair can be produced in the collision of two protons via a virtual photon or Z-boson. In fact, one quark in one proton and one antiquark from the other annihilate into a virtual photon which then decays into a lepton pair. An extensive review of the DY process is presented in ref. [61]. The differential cross section for the process is:

$$\frac{d\sigma}{dM^2} = \frac{4\pi\alpha_{em}^2}{3nM^4}\Sigma e_i^2 \frac{M^2}{s}\int dx_1 dx_2 [G_{q_i/p}(x_1)G_{\overline{q}_i/p}(x_2) + G_{\overline{q}_i/p}(x_1)G_{q_i/p}(x_2)]\delta(\frac{M^2}{s} - x_1x_2) \tag{3.43}$$

where M is the mass of the virtual photon, e_i represents the quark charge and n is the number of possible quark colors. The variables x_i are the fractional momenta of the quarks and are defined each as the the ratio between the quark momentum and the momentum of the parent proton. The functions $G_{q_i/p}(x)$ and $G_{\overline{q}_i/p}(x)$ represent the probability that quark q_i(or the antiquark $\overline{q}_i$) has a fractional momentum x_i.

The mass of the photon, M, is related with the fractional momentum of the quarks, x_i and the center of mass energy energy squared, $s = 4E^2_{beam}$, through:

$$M^2 = sx_1x_2 \tag{3.44}$$

The cross section for the magnetic monopole DY production is derived from equation (3.43). In this case the term α^2_{em} has to be replaced by $\alpha_{em}\alpha_{mm}$ to correct for the magnetic coupling present at the monopole/anti-monopole vertex(see the Feyman diagram in Fig. 3.2). With these considerations the term α^2_{em}:

$$\alpha^2_{em} \rightarrow \alpha_{em}\alpha_{mm} \tag{3.45}$$

Using eq.(3.42) we have:

$$\alpha^2_{em} \rightarrow \alpha_{em}\frac{1}{4\alpha_{em}}\beta^2 = \frac{\beta^2}{4} \tag{3.46}$$

This equation depends on the fractional momentum of the quarks trough the velocity dependence of the virtual photon mass M:

$$\beta = \sqrt{1 - \frac{4m^2_M}{M^2}} \tag{3.47}$$

where m_M is the magnetic monopole mass.

Because of this dependence, in the cross section for the magnetic monopole, the term described by eq.(3.45) has to be integrated over the quarks fractional momenta:

$$\frac{d\sigma_{MM}}{dM^2} = \frac{4\pi}{3nM^4}\Sigma\frac{e_i^2M^2}{s}\int dx_1dx_2\frac{\beta^2}{4}[G_{q_i/p}(x_1)G_{\bar{q}_i/p}(x_2)+G_{\bar{q}_i/p}(x_1)G_{q_i/p}(x_2)]\delta(\frac{M^2}{s}-x_1x_2) \tag{3.48}$$

Comparing the cross section of the two Drell-Yan processes we have, in the limit $\beta = 1$:

$$\frac{\sigma_{MM}}{\sigma_{DY}} = \frac{\frac{\beta^2}{4}}{\alpha_{em}^2} = \frac{\beta^2}{4\alpha_{em}^2} \tag{3.49}$$

From this equation we can see that the cross section for the magnetic monopole production is about 4700 times larger than the one for lepton production. With such a big estimated production cross section, monopole searches at LHC look optimistic.

3.2.1.2. Using Pythia to generate magnetic monopoles

In order to generate monopoles via the Drell-Yan process, the Pythia generator, version 6.403, was chosen and used as a part of the standard ATLAS computing framework, ATHENA [62]. To implement the correct cross section, as described in section 3.2.1.1, we need to modify the way the generator calculates the cross-section.

From the eq.(3.46) we observe that we can define a "modified" coupling constant α_{mod} as:

$$\alpha_{mod} = \frac{\beta}{2} \tag{3.50}$$

With this new coupling constant approach, we can minimize the number of changes to the generation software package. The only modification we need to make is to replace the electromagnetic coupling constant with the "modified" coupling constant:

$$\alpha_{em} \rightarrow \alpha_{mod} \tag{3.51}$$

Using this new coupling constant in equation(3.43) we get the cross section for the magnetic monopole DY process identical with the one presented in equation(3.48).

The changing of the definition of the coupling constant was implemented in a FORTRAN subroutine **pysgwz.F** which is a part of the standard ATHENA Generators package. The Drell-Yan monopole production process was setup in the python jobOption by setting "msub 1 1" flag with the Z^*/γ interference switched on ("mstp 43 1"). Since the magnetic monopoles are not implemented in Pythia, the generator was set to produce "heavy muons" by assigning to the flag "pmas 13" values equivalent to the monopole mass.

In the ATHENA framework, each particle is assigned a numeric identification(ID) code according to the Particle Data Group(PDG) convention. There is a standard meaning for the digits in a PDG code that is described in the PDG review articles [29]. Note 11(c) of the PDG table says that "one-of-a-kind particles are assigned numbers in the range 41-80". The (PDG) ID of the magnetic monopole was chosen to be 50.

After generation, the ID of the "heavy muons" was change to 50, in order to be able to propagate the monopole through the detector correctly. This ID reassignment was done by adding a piece of code called TranslateMonoID to the HepMCTools package. In Fig. 3.3 and Fig. 3.4 we show the histograms confirming that a particle with ID 50 and mass 350 GeV has been produced in PYTHIA.

The cross section values, as calculated by Pythia, for a different magnetic monopole

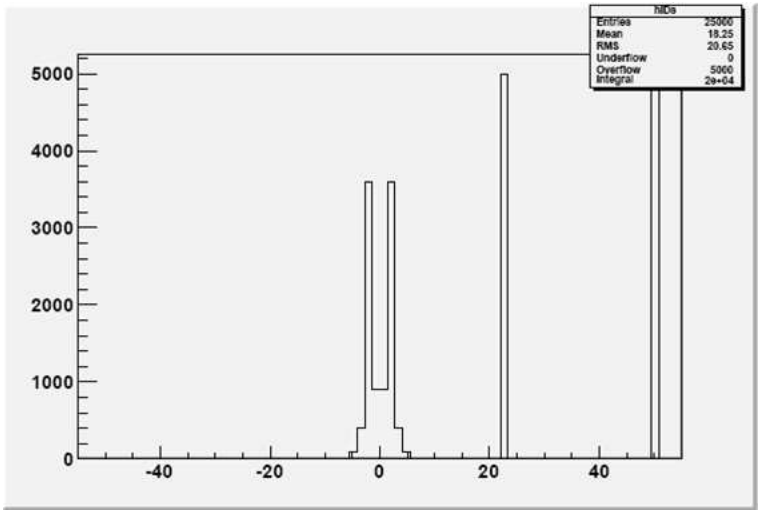

Figure 3.3. Magnetic monopole ID

masses are listed in 3.1. These values show good agreement with the theoretical predictions. The expected values of the cross section at the LHC, as a function of the monopole mass are shown in Fig. 3.5.

The generation of a full monopole event with the Pythia code has to account for the modified coupling constant.

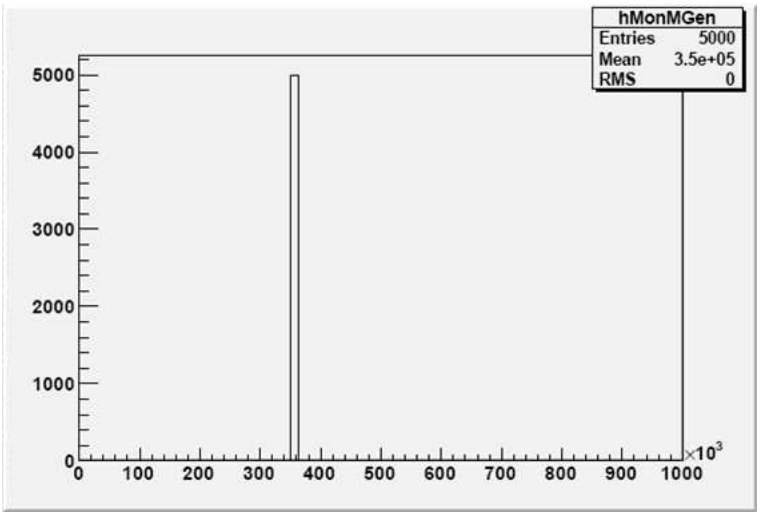

Figure 3.4. Magnetic monopole mass

Table 3.1. Values of the DY magnetic monopole cross section, as calculated by Pythia, for different monopole masses.

$Mass(GeV)$	$CrossSection(pb)$
350	19.00
500	4.04
750	0.56

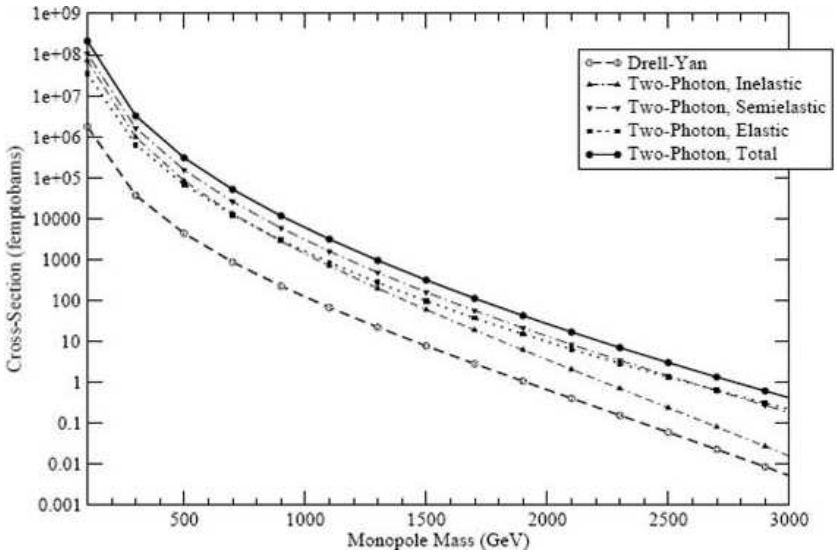

Figure 3.5. Expected magnetic monopole for the Drell-Yan process at LHC

Since using this coupling constant would lead to wrong generation of all standard charged particles, which should have standard electromagnetic coupling, we generate the monopole event with all parton showers and hadronization processes turned off. Then a standard Drell-Yan muon sample is produced with the "heavy" muon mass matching the magnetic monopole mass in order to ensure energy and momentum conservation. The muons were eliminated and the remaining event was superimposed over the monopole sample. Thus we were able to create a "real" magnetic monopole event.

3.2.2. Simulation

The coordinate system and the names of variables used for describing the ATLAS detector are briefly described here as they are used repeatedly in the following paragraphs. The beam direction defines the z-axis and the x-y plane is the plane transverse to the beam direction. The positive x-axis is defined as pointing from the interaction point to the centre of the LHC ring and the positive y-axis is defined as pointing upwards. The azimuthal angle ϕ is measured around the beam axis, and the polar angle θ is the angle from the beam axis. A new variable called pseudorapidity is defined as :

$$\eta = -ln(tan\frac{\theta}{2}) \tag{3.52}$$

Variable of the form A_T are defined in the x-y plane unless stated otherwise. They are called transverse variables like transverse momentum p_T or transverse energy E_T. They describe the fraction of the momentum or energy projected on the transverse plane.

Another term frequently mentioned is the ATHENA framework. This framework, developed by the ATLAS experiment, is a skeleton of an application in which developers plug in their codes. The framework provides most of the common functionalities needed and ensures communication between different components.

The system of units used in Particle Physics is not the International System (SI). Instead a system of units called *natural* system of units is used. Because Particle Physics relies on Special Relativity and Quantum Mechanics almost all formulas contain the speed of light in vacuum $c = 3.0 \times 10^8 m/s$ and the Planck constant $\hbar = h/2\pi = 1.055 \times 10^{-34} Js$. The *natural* system of units sets $\hbar \equiv c \equiv 1$.

With this convention we have $E^2 = m^2 + p^2$. This implies that the units for energy, mass and momentum are the same. The unit for energy is $1\text{GeV} = 1.602 \times 10^{-10} J$ and its multiples.

3.2.2.1. Trajectory in Inner Detector

To evaluate the momentum of particles produced in a proton-proton collision, the Inner detector uses the fact that the trajectories of electrically charged particles in the presence of a magnetic field will bend due to the Lorentz force and that the radius of curvature of this bending is directly proportional to the particle's momentum. For a particle with the momentum p (in GeV) and a charge ze in a uniform magnetic field $\mathbf{B}$ (in Tesla) the trajectory is a helix with the pitch angle λ and radius R (in meters). The relation connecting the momentum to the radius is given by [29]:

$$p \cdot cos\lambda = 0.3z \cdot \mathbf{B} \cdot R \tag{3.53}$$

Based on this concept, the Inner Detector region is enclosed inside the solenoid that produces a two Tesla magnetic field oriented parallel to the beam axis. By measuring the radius of a curved trajectory we have information about the momentum of the particle.

The magnetic monopole trajectory inside the ATLAS detector will be distinct because will bend in the "wrong" direction. In contrast to an electron, the monopole will be accelerated by the magnetic field and its trajectory will thus bend in the $x - z$ plane while remaining a straight line in the $x - y$ plane.

However, because of the expected huge mass of the magnetic monopole mass, the acceleration in the direction of the magnetic field is negligible. A detailed evaluation is given in Appendix A.

Using the electric/magnetic duality, the behavior of the magnetic charge in uniform magnetic field can be considered analogous to the behavior of the electric charge in electric field. Assuming a uniform magnetic field in the z direction, the solution of the monopole equation of motion is, as presented by [68]:

$$\overrightarrow{r}(t) = \frac{E_{T0}}{gB}(\sqrt{1 + (\frac{gB}{E_{T0}}t)^2} - 1)\widehat{e_z} + \frac{p_{T0}}{gB} arcsinh(\frac{gB}{E_{T0}}t)\widehat{e_T} \tag{3.54}$$

where

$$E_{T0} = p_{T0}^2 + m^2 \tag{3.55}$$

is the transverse initial energy, p_{T0} is the transverse momentum, $\widehat{e_z}$ is the unit vector along the z direction, $\widehat{e_T}$ is the unit vector in the transverse direction and t is the time.

In Fig. 3.6 are plotted the trajectories of a 350 GeV mass monopole in a uniform magnetic field of two Tesla oriented along the z axis. The transverse momentum was varied from 50 KeV to 10 MeV. The plot focuses on a spatial region of 7 meters of length and 1.2 meters in radius corresponding to the Inner detector dimensions. In this region, the bending of the trajectory for a magnetic monopole with p_T larger than a few GeV is negligible.

To establish a precise limit in which the linear trajectory approximation is valid one needs to evaluate the displacement, along the z direction, of the curved trajectory from the linear track and then to compare it with the resolution of the Inner Detector.

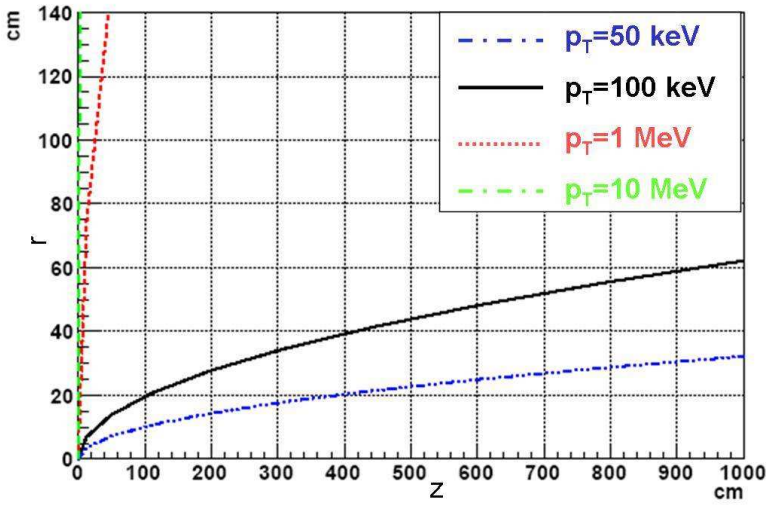

Figure 3.6. Trajectory of a Magnetic Monopole with 350 GeV mass and different p_T in 2T uniform magnetic field

The trajectories for which the displacement remains smaller than the resolution will be detected as linear.

We are plotting the displacement as a function of p_T for a magnetic monopole with 350 GeV mass, and comparing it with specific resolutions in two regions of the Inner Detector. In the the Semiconductor Tracker (Fig. 3.7) the resolution in z direction has a value of 66 μm. The resolution of the Silicon Strips region of the Inner Detector is 680 μm(Fig. 3.8). The specific resolutions are represented by the dotted lines on the two plots.

We conclude that the trajectory of a magnetic monopole with a p_T greater than 60 MeV can be approximated by a straight line. This conclusion was used in the Monte Carlo setup of the Geant4 Simulation where the magnetic monopole was propagated similar to a neutral particle.

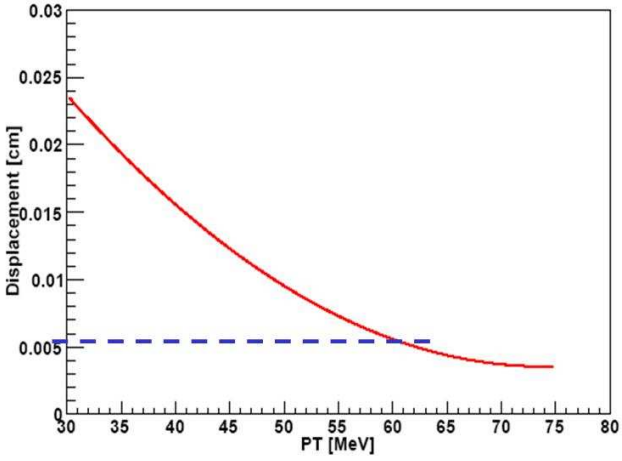

Figure 3.7. Displacement from the linear path for a 350 GeV monopole mass compared to the Pixel Detector resolution(the dotted line)

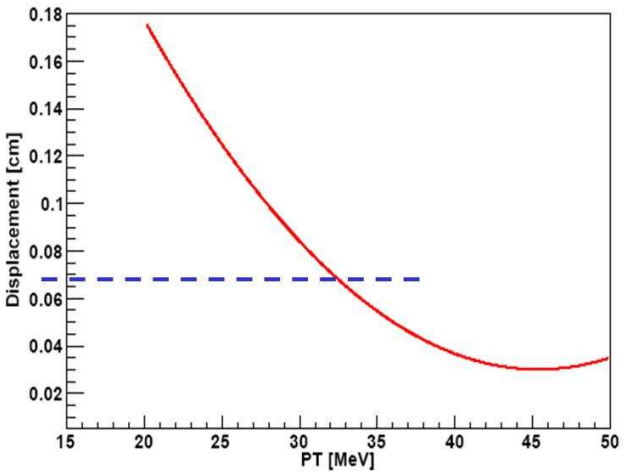

Figure 3.8. Displacement from the linear path for a 350 GeV monopole mass compared to the Semiconductor Tracker resolution(the dotted line)

3.2.2.2. Relativistic monopole energy loss in matter

The way the magnetic monopole interacts with matter depends on values of their velocities. A detailed description is given in reference [56]. Fast magnetic monopoles, with $\beta > 10^{-2}$, which are the objects of this study, behave like an equivalent electric charge with an electric charge $(ze)_{eq} = g_D\beta$ where g_D is the Dirac magnetic monopole charge. Monopole with $10^{-4} < \beta < 10^{-2}$the energy is lost in ionization or excitation of the atoms and molecules of the medium. Low velocity monopoles, with $\beta < 10^{-4}$, lose energy in elastic collisions with atoms or with nuclei. In Fig. 3.9 we show the energy loss of magnetic monopole with Dirac magnetic charge in liquid hydrogen as a function of β as presented by [56].

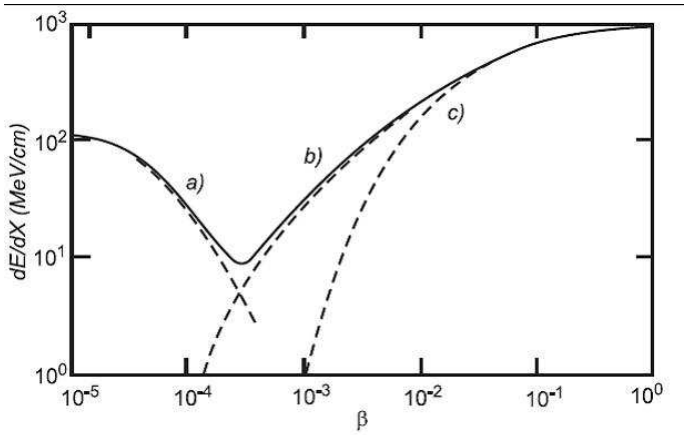

Figure 3.9. The energy losses,in MeV/cm, for Dirac Magnetic Monopoles in liquid hydrogen as a function of β: a) corresponds to elastic monopolehydrogen atom scattering; b) corresponds to excitation of the hydrogen atoms; c) describes the ionization energy loss.

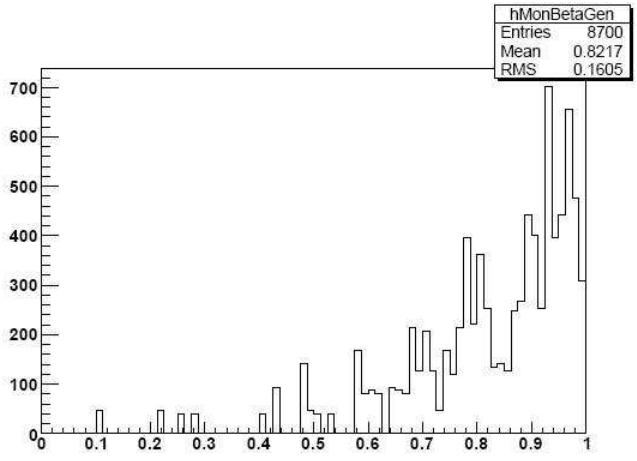

Figure 3.10. The β distribution for the Drell-Yan process producing a magnetic monopoles with 350 GeV mass.

In Fig. 3.10, the β distribution is plotted for a magnetic monopole sample with mass of 350 GeV, produced through the DY process described in chapter (3.2.1.1)-(3.2.1.2). From the plot it is evident that most of the events have $\beta > 0.1$ which clearly situates them in the category of fast magnetic monopoles that interact with matter predominantly through ionization.

The monopole-matter interaction was described in references [63] and [64]. We consider the energy loss due three mechanisms: the ionization of the medium, pair production and bremsstrahlung.

For relativistic monopoles, the energy loss by ionization is described by the formula [65]:

$$\frac{dE_M}{dx} = -\frac{4\pi Z \alpha_{em} \alpha_{mm} N_A}{A m_e} [\ln(\frac{m_e \beta^2 \gamma^2}{I}) - \frac{\delta}{2}] \tag{3.56}$$

where :

-$\gamma = \sqrt{\frac{1}{1-\beta^2}}$ and $\beta = \frac{v}{c}$,

-Z atomic number of the medium,

-m_e is the electron mass,

-I mean excitation energy of the material,

-A is the atomic mass of the medium,

-$\alpha_{em} = \frac{1}{137}$ electromagnetic coupling constant,

-$\alpha_{mm} = 34.5$ magnetic monopole coupling constant,

-δ parameterizes the density effect [66].

The density effect refers to the tendency of matter to become polarized as the velocity of the incident particle increases.

From this formula we can conclude that the energy loss by the magnetic monopole due to ionization is not dependent on the monopole mass, but it depends on the magnetic coupling constant α_{mm}.

The energy loss by magnetic monopole through pair production is obtained by adapting the study on the energy loss through pair production by muons to the magnetic monopole case [65]. For the region of interest, defined by $m_M > m_e$ and $\gamma < 10^5$, where m_M is the monopole mass:

$$\frac{dE_{pair}}{dx} \simeq -\frac{19\pi}{9}\frac{\alpha^3\alpha_{mm}Z^2N_A}{Am_e}\gamma[(1-\mathbf{B}_1)\ln(\frac{\gamma}{4})-\mathbf{B}_2] \tag{3.57}$$

where:

$$\mathbf{B}_1 = \frac{48}{19\pi^2}\frac{m_e}{m_M}\ln(\frac{m_M}{m_e})^2 \tag{3.58}$$

$$\mathbf{B}_2 = \frac{11}{6} - \frac{16}{19\pi^2}\frac{m_e}{m_M}\ln(\frac{m_M}{m_e})^3 \tag{3.59}$$

The energy loss by Bremsstrahlung is inversely proportional to the mass of the particle, so taking into account the huge monopole mass, this energy loss should be negligible:

$$\frac{dE_{brem}}{dx} = -\frac{16}{3}\frac{\alpha\alpha_{mm}^2Z^2N_A}{Am_M}\gamma\ln(\gamma) \tag{3.60}$$

In Fig. 3.11 we show the energies losses for a magnetic monopole with a $350GeV$ monopole mass in silicon block. From those three plots, we conclude that the energy loss due to ionization is the dominant process.

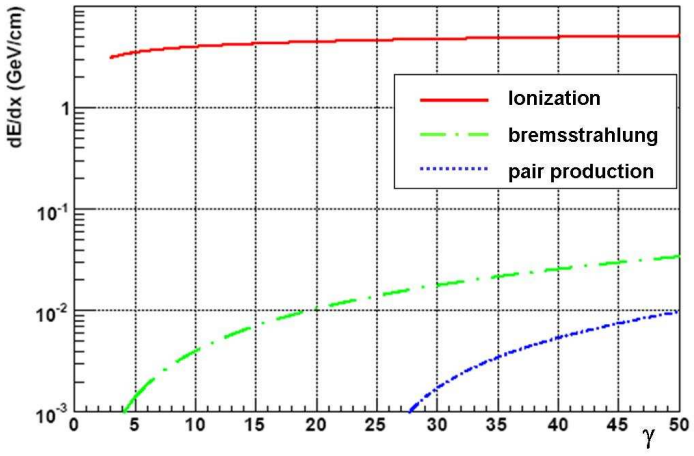

Figure 3.11. The electromagnetic energy loss from ionization-red, pair production-blue and bremsstrahlung-green for a 350 GeV monopole mass in Silicon

We use this result in modeling the interactions of the magnetic monopole with matter using the Monte Carlo Geant4 Simulation package.

3.2.2.3. Geant4 Simulation

The propagation of particles through matter is simulated by an elaborated program called Geant4 [67]. Its areas of application include high energy physics, nuclear physics and accelerator physics, as well as medical and space science. The understanding of the experimental conditions and performance of an experiment, both in the optimization and design phase as well as during data acquisition, relies heavily on the computer simulation of the experiment. Starting from 2004 Geant4 is the only officially supported software for the ATLAS detector simulation.

This highly configurable and flexible software can therefore accommodate all the requirements the simulation of a complex experiment such as ATLAS imposes.

GEANT4 is a toolkit for simulating the passage of particles through matter. It includes tools for designing the geometry of the system, a large set of materials and fundamental particles and most importantly, a wide range of physical processes. In Geant4 each particle with a given momentum vector is propagated in steps through the material. At each step the probability of interaction is calculated . The resulting secondary particles are then propagated in the same manner. This enable us to track the passage of a particle passage through the defined geometry, to record its interaction with the materials and the response of sensitive detectors. A comparison of the known generated particles with the reconstructed particles (particle for which the passage through the detector was simulated) gives us means to evaluate the detection efficiency.

Up to now, we established that the magnetic monopole will behave like a neutral, massive particle that interacts with matter via ionization. The magnetic monopole, with the PDG ID 50, was implemented in the Geant4 Simulation by adding a new package called **Monopole** to the Simulation/G4Extensions/. This code was set to propagate the magnetic monopole in straight line according the conclusions of chapter (3.2.2.1) through the ATLAS detector and models an energy loss following the modified Bethe-Bloch presented in eq.(3.58).

Using the Monopole simulation package, a sample of magnetic monopoles produced by a Single Particle Gun generator was propagated through the ATLAS detector and then analyzed. The Single Particle Gun generator produces single particles, specified by their PDG ID codes and either (p_T, η, ϕ) or (E, θ, ϕ) where E is the energy of the particle. In our case the magnetic monopoles, with mass of 350 GeV, were produced with a flat eta and phi distributions.

The energy of the gun was set at 1 TeV.

To check that indeed the tracks of the simulate magnetic monopole events are

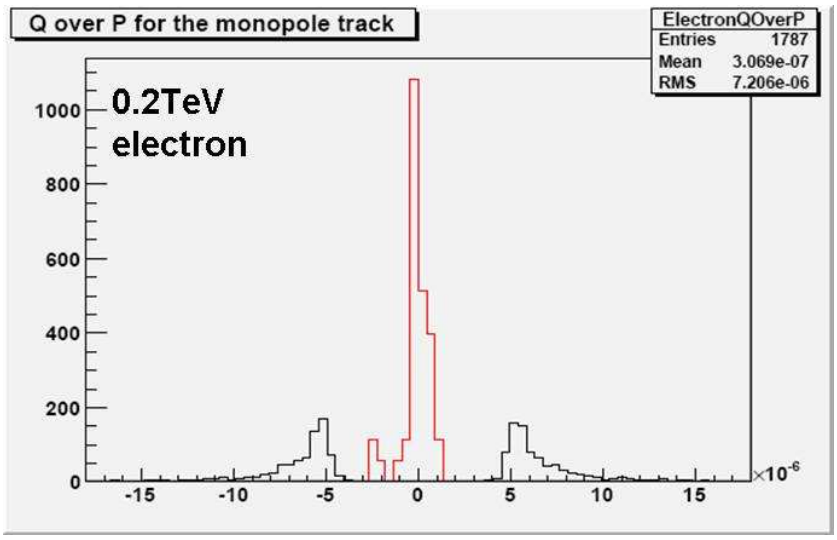

Figure 3.12. Inverse momentum for monopoles in red vs electrons with 200 GeV energy in black

linear, we investigate the values of the inverse momentum of the particle. The relation between the radius of curvature of the trajectory and the momentum of the particle, eq.(3.56), implies that for a linear track, $R \to \infty$, we expect a very small inverse momentum $1/p \to 0$. In Fig. 3.12 the inverse momentum of a monopole sample with the mass 350 GeV (the red line) is compared with the one of an electron sample(black) with an energy of 200 GeV. For consistency, the electron-control sample was produced in the same conditions, using the Single Particle Gun with the same geometrical settings. The plot shows a peak of zero value for 1/p corresponding to infinite radius of curvature for the magnetic monopole events from which we conclude that they are propagated following a linear track.

The magnetic monopole losses energy in interaction with matter according to equation (3.56). To prove that indeed our simulated sample follows this behavior, we compared the energy deposited in the Electromagnetic Calorimeter Barrel (EMB) by the monopole sample with the energy loss of a muon-control sample. Again for consistency the muon-control sample was created using the Single Particle gun with similar geometrical setting and with an energy set at 10 GeV. The choice for the value of the muon energy was made so that the β of the muon and monopole samples match. The Bethe-Bloch energy loss formula for muon is:

$$\frac{dE_{muon}}{dx} = -\frac{4\pi Z\alpha_{em}^2 N_A}{Am_e}\frac{1}{\beta^2}[\ln(\frac{m_e\beta^2\gamma^2}{I}) - \frac{\delta}{2}] \tag{3.61}$$

where:

-Z atomic number of the medium,

-m_e is the electron mass,

-I mean excitation energy of the material,

-A is the atomic mass of the medium,

-$\alpha_{em} = \frac{1}{137}$ electromagnetic coupling constant,

-δ parameterizes the density effect [66].

By dividing equations (3.56) and (3.61) we have:

$$\frac{\frac{dE_M}{dx}}{\frac{dE_{muon}}{dx}} = \frac{\alpha_{mm}}{\alpha_{em}}\beta^2 \tag{3.62}$$

In the limit $\beta \to 1$ this ratio has a value of approximately 4700. This implies that we expect the magnetic monopole to deposit 4700 times more energy in the calorimeter than the muon.

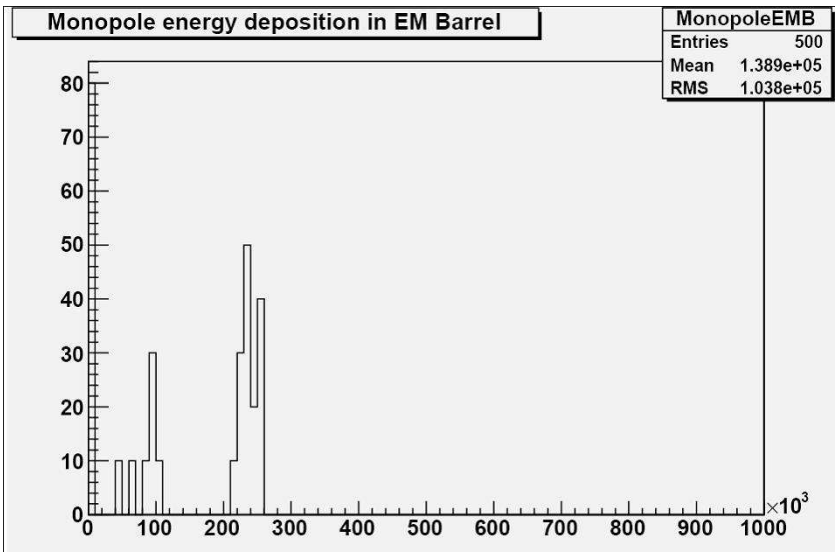

Figure 3.13. Energy deposited in EMB by monopoles

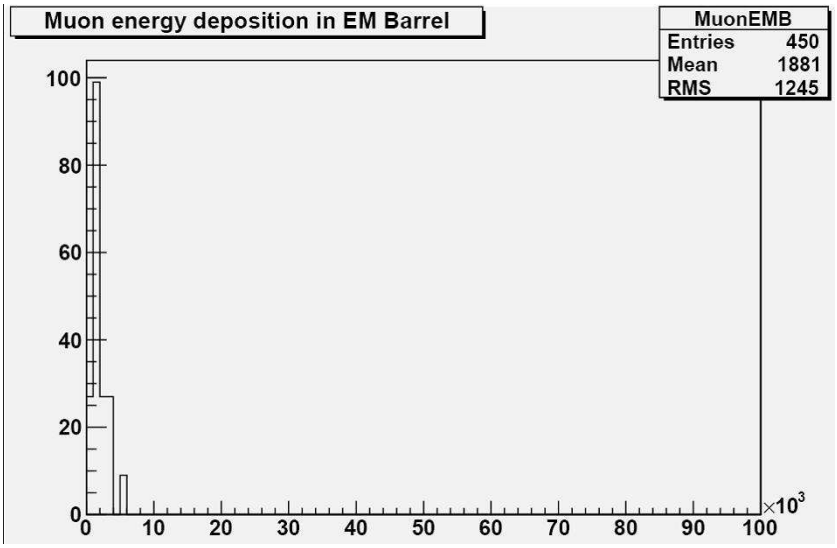

Figure 3.14. Energy deposited in EMB by muons

We show the total energy loss in EMB by monopoles in Fig. 3.13 , and muons in Fig. 3.14 . From the plots, the ratio between the two energies is around 200 which is a lot less than expected. The explanation for this unexpected behavior would be the saturation of the detector cells. The ATLAS calorimeters are segmented in cells in (R, θ, ϕ). Each of these cells is read out independently. The calorimeter cell is thus the smallest detection unit that provides energy deposition readings through the read-out system. When the energy deposition exceeds a certain limit the electronics signals get saturated. Furthermore, the increase of the deposited energy does not increase the signal response. To prove that this indeed the case with the magnetic monopole signal we increased the energy of the particle gun and plotted the energy deposited in different layers inside the EMB.

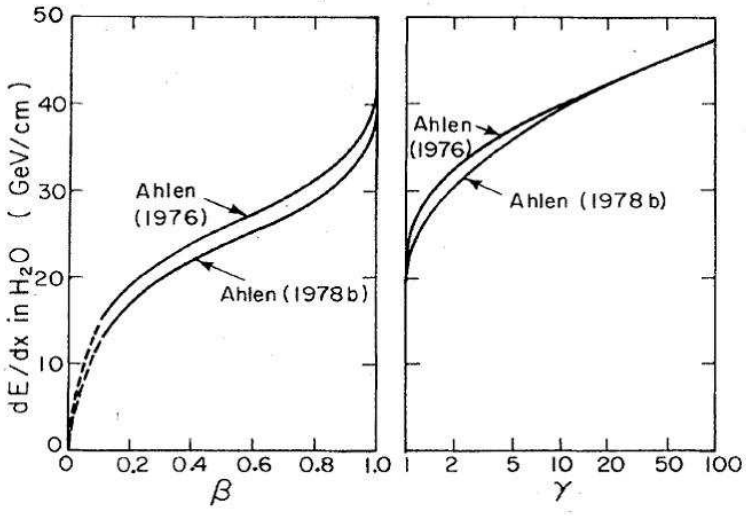

Figure 3.15. Stoping power for a magnetic monopole in water as calculated by Ahlen (1976) and then corrected it(1978)

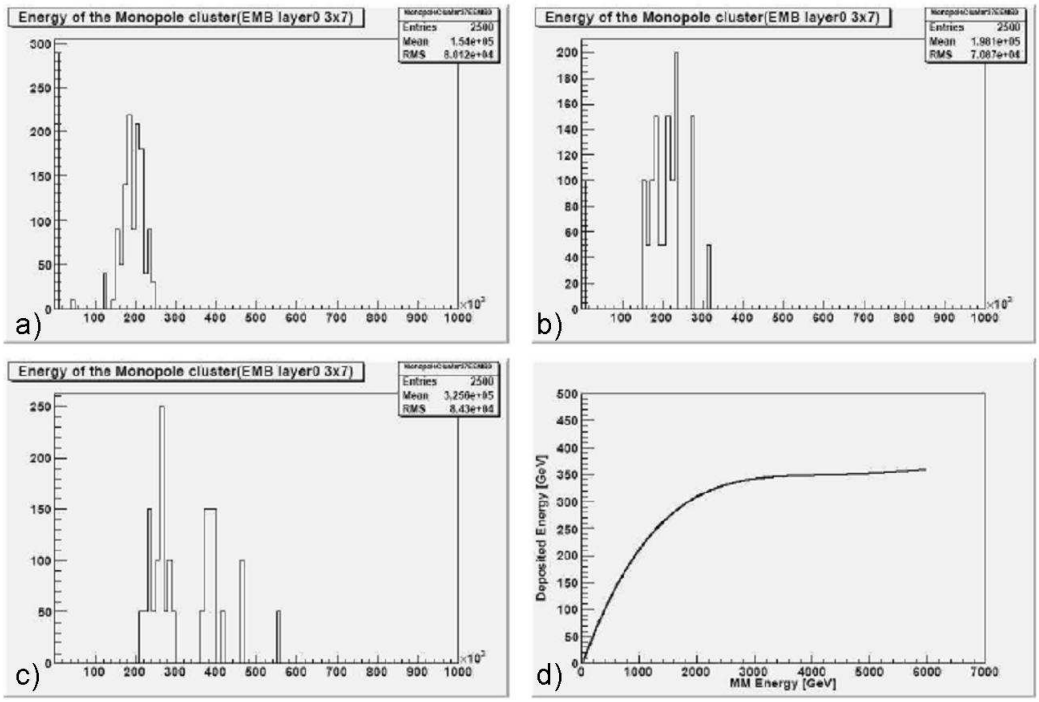

Figure 3.16. The energy deposited in the Presampler by magnetic monopoles with mass 350 GeV and energy:a) 0.9 TeV, b) 1TeV, c) 4 TeV ; d) reconstructed energy In the detector versus the actual energy of the magnetic monopole

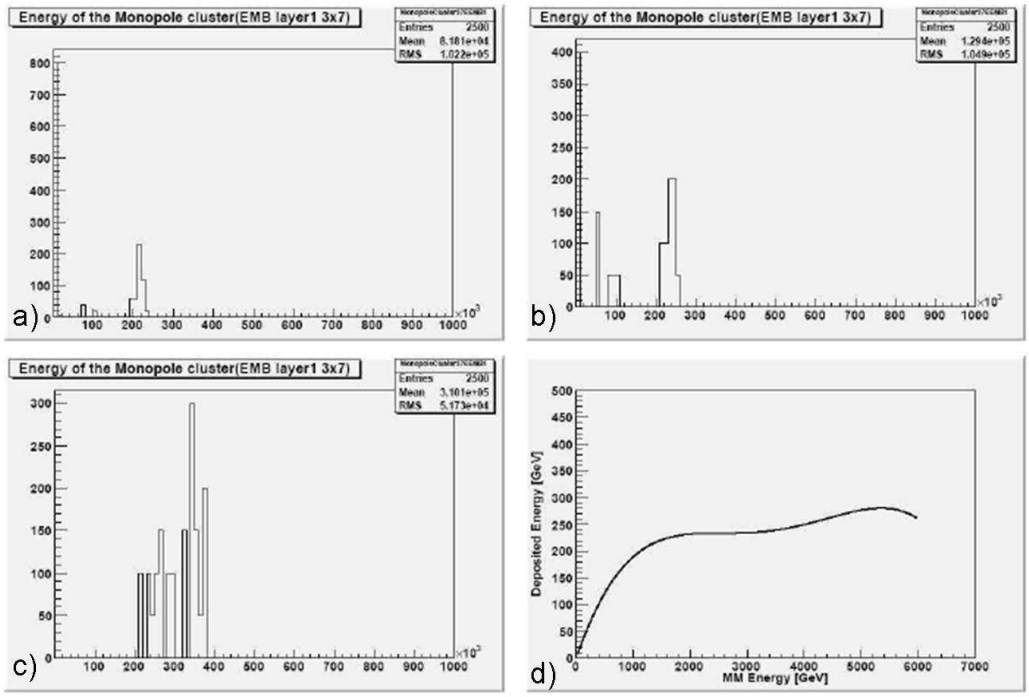

Figure 3.17. The energy deposited in the first Layer of the EMB by magnetic monopoles with mass 350 GeV and energy:a) 0.9 TeV, b) 1TeV, c) 4 TeV ; d) reconstructed energy In the detector versus the actual energy of the magnetic monopole

In Fig. 3.16 we show the plots for the energy deposited in the Presampler. The magnetic monopole has a mass of 350 GeV and its energy is set to 0.9 TeV (plot a), 1 TeV (plot b) and 4 TeV (plot c). The last plot (plot d) shows the reconstructed energy deposition as a function of the actual energy of the magnetic monopole. From this plot it is easy to see the saturation effect. In Fig. 3.15 we show the expected energy loss in the passage of the magnetic monopole through matter [64] as a function of β. The corresponding plot for ATLAS detector is expected to have similar characteristics. The material composition of the ATLAS detector is too complex to perform accurate calculations. Nevertheless, although the vertical scale will change due to the different Z composition of the ATLAS calorimeter, the smooth rise with the increase of β or γ will remain the same. Thus, it is expected that as the initial energy increases so does the energy loss. The discrepancy between the two facts is explained by the saturation of the readout electronics of the detector cells resulting in a lower reconstructed energy.

To prove consistency of the saturation throughout the detector, the energy deposited in all three layers were checked. Fig. 3.17 shows the energy deposited, by the same magnetic monopole sample, in Layer 1 inside the EMB. Again the saturation of the detector cells becomes obvious in the plot d) that shows the dependence of the energy deposited in the calorimeter on the initial energy of the particle.

With the understanding of the way that the magnetic monopole is generated and propagated through the ATLAS detector we now need to define a search strategy that will successfully identify the unique magnetic monopole signal.

3.2.3. Search criteria

3.2.3.1. Trigger

ATLAS has a three level trigger system designed to reduce the volume of data-recording event. Each trigger level refines made by the previous. A more detailed description was presented in chapter 1 (1.2.2.4). The Level 1 trigger (LVL1) works on information from the calorimeter and muon detectors to identify regions that contain relevant physics information called a Regions of Interest(RoI). The RoI are passed then to the Level 2(LVL2) trigger for further analysis based on refining the selection of candidate objects using information from all detectors, including the inner tracker which is not used at LVL1. The last step, the Event Filter analyzes fully reconstructed events.

In order to estimate correctly the number of magnetic monopole events expected to be found by the LHC we need to evaluate two efficiencies: the trigger selection efficiency, ε_{trig}, and the reconstruction efficiency, ε_{Reco}; that measures the probability of correct reconstruction of the monopole event. The number of expected events is then:

$$N = \sigma \cdot \varepsilon_{trig} \cdot \varepsilon_{Reco} \cdot L \tag{3.63}$$

where σ is the event cross section and L is the integrated luminosity of the LHC run period.

The trigger efficiency was calculated using the formula:

$$\epsilon_{Trig} = \frac{N(passEF)}{N(truth)}, \tag{3.64}$$

where $N(passEF)$ is the number of events that passed the Event Filter requirements and $N(truth)$ is the number of generated events.

The ATLAS trigger algorithm does not have a specific magnetic monopole hypothesis. We need to use one of the already defined signatures to see if the monopole signal will pass the trigger. The magnetic monopole ionizes heavily and while doing so losses energy rapidly. It will eventually be stopped in the detector material. Because of this specific behavior, only a small number of events will reach the Hadronic Calorimeter and practically none will reach the Muon Detector. Therefore, the trigger signatures for muon and hadrons cannot be used. Because the monopole signal has geometry similar to that of heavily ionizing charged particle, it has a track component and does not resemble a photon event.

Thus the closest match is the electron trigger signature. We chose to use the "e10"

Table 3.2. Cuts for e10 signature.

$LVL1$	$LVL2$	$LVL2(track)$	EF
$E_T > 7GeV$	$E_T = 10GeV$	$p_T > 1.0GeV$	$E_T cluster > 10GeV$
	$E_T HAD < 2GeV$	$delPhi < 0.1$	
	$RCore > 0.86$	$delEta < 0.05$	
	$ERatio > 0.8$		

signature which refers to electrons with transverse momentum greater than 10 GeV. The selection criteria for this signature at each trigger level are summarized in Table 3.2. In the table:

-E_T is the electromagnetic transverse energy,

-$E_T HAD$ is the hadronic transverse energy,

-$RCore = \frac{E_{3\times7}}{E_{7\times7}}$ with $E_{n\times m}$ the energy deposited in a window of $n \times m$ cells around the LVL1 RoI,

-$ERatio = \frac{E_{1st}-E_{2nd}}{E_{1st}+E_{2nd}}$ where E_{1st} and E_{2nd} are the energies of the two highest maxima.

-p_T is the transverse momentum,

-$delPhi$ the phi extent of the cluster,

-$delEta$ the eta extent of the cluster,

-$E_T cluster$ transverse energy of the cluster.

The trigger efficiencies were evaluated in a model independent setup at first, using the Single Particle Gun generator described in chapter (3.2.2.3), to produce magnetic monopole events with a uniform eta and phi distributions. Then, the particular case of the Drell-Yan monopole production process was studied. We expect a dependency on both mass and energy, so both aspects were carefully evaluated.

To establish the dependency on energy of the particle, a sample of magnetic monopoles with fixed mass of 350 GeV, and different energies ranging from 0.75 TeV to 2 TeV was used. Table 3.3 shows these efficiencies evaluated in two regions: the Electromagnetic Calorimeter Barrel only ($\eta < 1.4$) and in the full detector region ($\eta < 2.5$). The plot of the trigger efficiency as a function of eta is shown in Fig. 3.18. As the energy of the magnetic monopole increases the efficiency becomes close to one.

The magnetic monopoles mass is another factor that plays an important role. In this case a Single Particle Gun generator was used to produce magnetic monopole events with different masses: 600 GeV, 500 GeV and 350 GeV at a fixed energy of 1 TeV . In Table 3.4 we show the mass dependence of the trigger efficiency in the EMB and in the whole calorimeter. Fig 3.19 illustrates the eta distribution of efficiencies in this case. As the mass of the magnetic monopole increases the efficiency drops.

After evaluating the overall trigger efficiency, a specific production channel was studied, the magnetic monopole Drell-Yan process.

Table 3.3. Trigger efficiency for for magnetic monopoles with fixed mass of 350 GeV and energies ranging from 0.75 TeV to 2 TeV.

Single Particle	ε_{Trig}	
$Energy(TeV)$	$\eta < 1.4$	$\eta < 2.5$
0.75	0.55 ± 0.013	0.37 ± 0.010
0.9	1.00 ± 0.027	0.86 ± 0.007
1	1.00 ± 0.019	0.92 ± 0.004
2	1.00 ± 0.027	1.00 ± 0.022

Table 3.4. Trigger efficiency for magnetic monopole masses with fixed 1TeV energy and different masses.

$ParticleGun$	ε_{Trig}	
$Mass(GeV)$	$\eta < 1.4$	$\eta < 2.5$
350	1.00 ± 0.019	0.92 ± 0.004
500	0.52 ± 0.010	0.47 ± 0.008
600	0.00 ± 0.022	0.00 ± 0.017

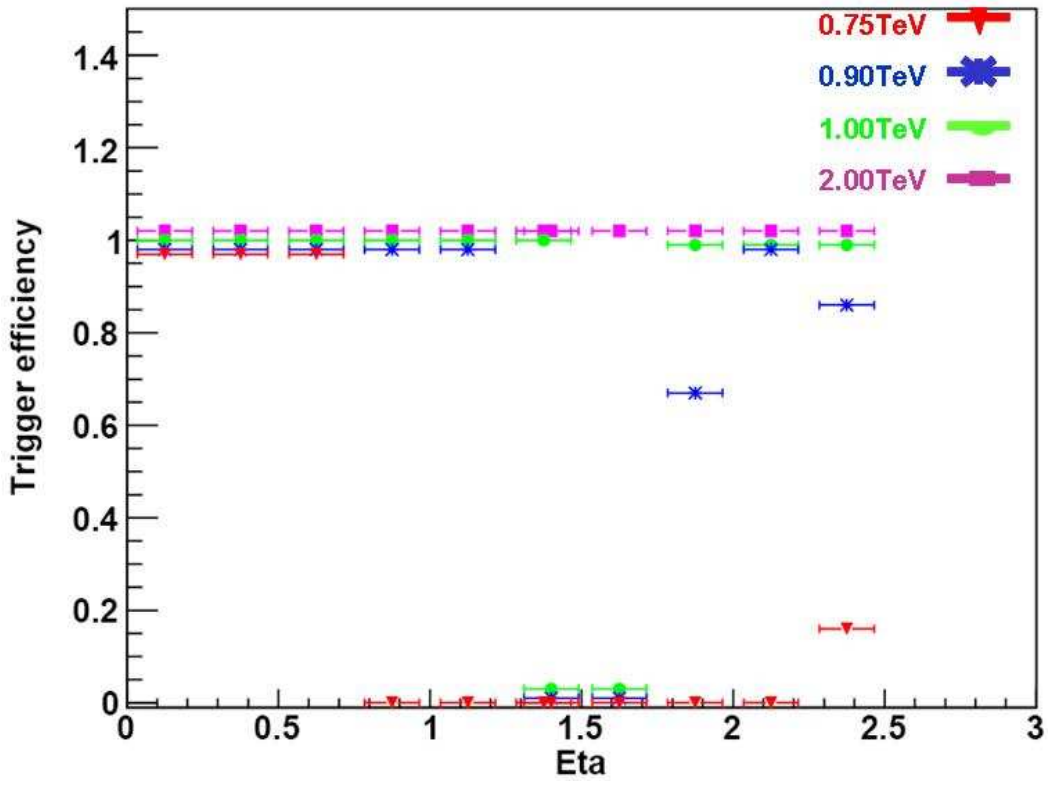

Figure 3.18. Eta distribution of trigger efficiencies for magnetic monopoles with fixed mass of 350 GeV but energies ranging from 0.75 TeV to 2 TeV

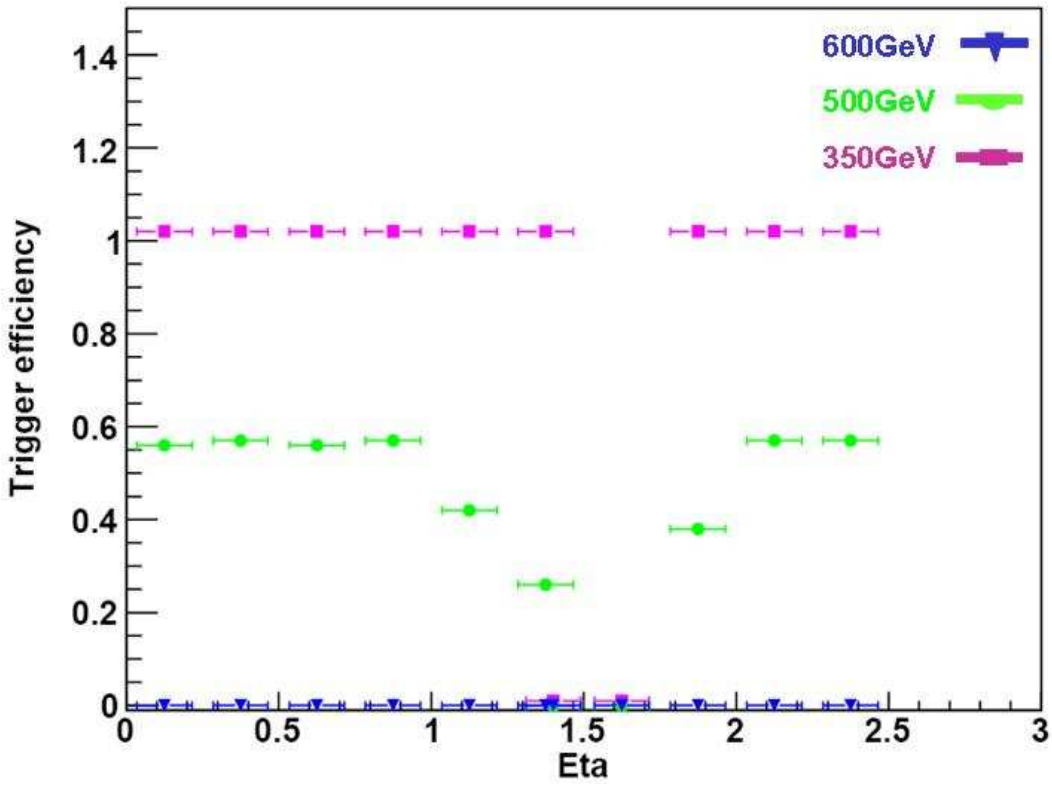

Figure 3.19. Eta distribution for trigger efficiencies for magnetic monopole masses with fixed 1TeV energy but different masses

The sample used in this case was produced using the modified Pythia code with all parton showers and hadronization processes turned off for reasons explained in the Cross Section paragraph (3.2.1.2). For this process, the eta dependence of the efficiency(see Fig. 3.20) shows higher values in the region of the forward calorimeter compared to the EMB.

This behavior is due to the kinematic of the Drell-Yan process. In Fig. 3.21 and

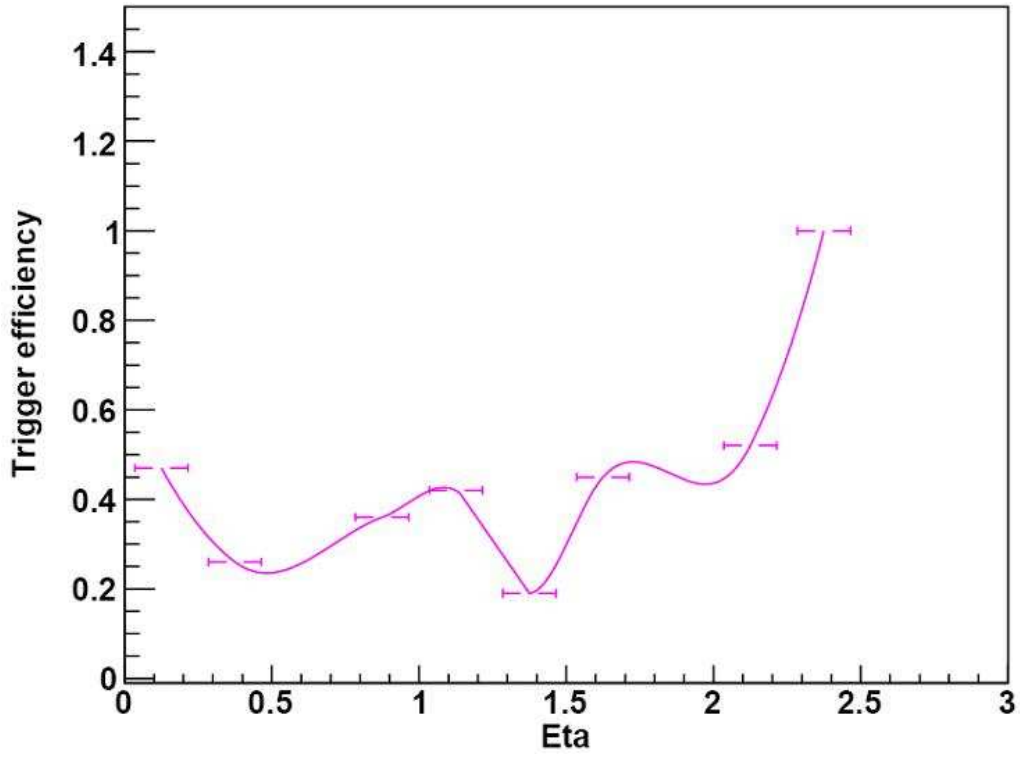

Figure 3.20. Eta distribution for trigger efficiencies for the Drell-Yan process

Fig. 3.22 we show the eta distribution of the energies before and after a 1 TeV energy cut. It is clear that higher energetic events are in the forward region.

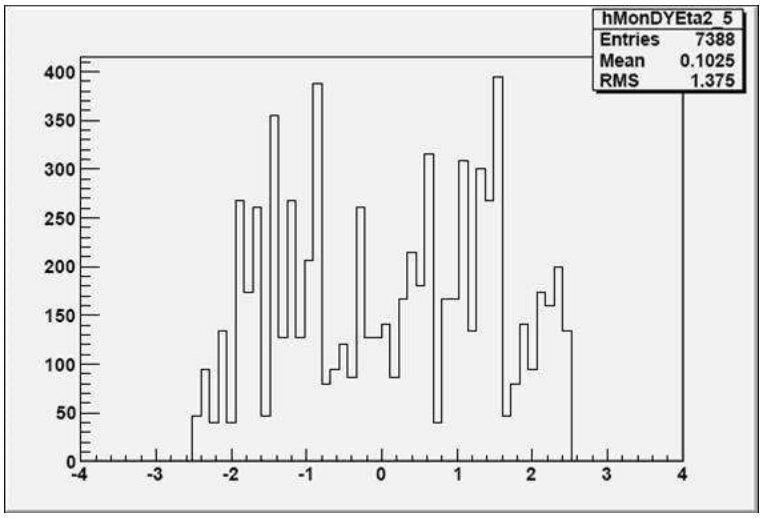

Figure 3.21. Energy distribution of the Drell-Yan sample

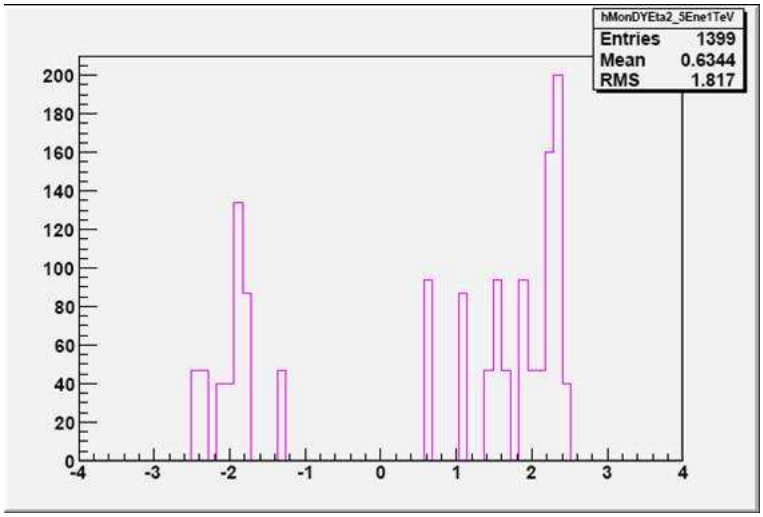

Figure 3.22. Energy above 1 TeV for the Drell-Yan sample

All eta trigger efficiency distributions show a drop in efficiency in the region of eta between $\eta = 1.4$ and $\eta = 1.6$. One reason for this is the existence of a crack at $\eta = 1.4$ between the barrel and the forward calorimeter. Also, the material distribution in Inner Detector (see Fig. 3.23) shows an increase in the material density in the region of eta between $\eta = 1.4$ and $\eta = 2.0$ that would explain why lower energetic samples will lose all their energy and get trapped in the material before reaching the calorimeter.

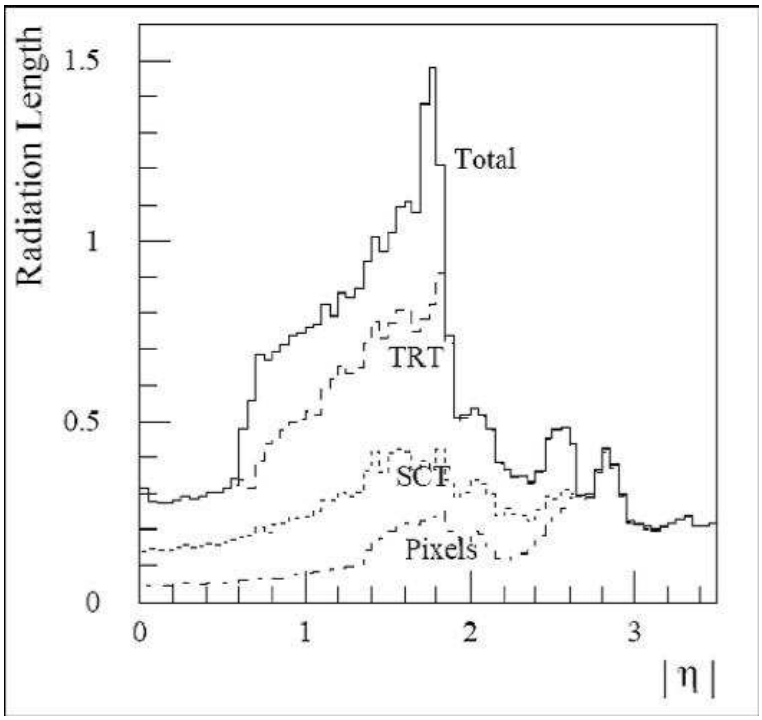

Figure 3.23. Eta distribution for trigger efficiencies

In conclusion, in spite the fact that we do not have a specific magnetic monopole trigger signature, using the single electron e10 is working with satisfactory results.

3.2.3.2. Calorimeter event reconstruction

We now proceed to define specific signatures of the magnetic monopole passage through the ATLAS detector. A magnetic monopole sample with a mass of 350 GeV was produced with a particle gun set up with flat eta and phi distributions. Based on the trigger efficiency study the energy of the gun was set at 1 TeV because for this energy all events fulfil the trigger requirements. As a control, we used an electron sample with the same geometry as the magnetic monopole sample. The electrons were produced using the Single Particle Gun generator setup to produce events with flat eta and phi distribution and fixed energy. To ensure an unbiased selection for the value of the cuts, the energy of the electron samples was varied from 100 GeV to 1 TeV. There are two aspects that are worth investigating, the linearity of the track and the shape of the electromagnetic cluster.

To investigate the linearity of the tracks, we use the variable Q/P which is the ratio of the charge to the reconstructed momentum of the particle. This variable is proportional with the inverse of the radius of the curvature of the monopoles tracks. Its value can be compared with the one for the electrons tracks see Fig. 3.24. The solid line marks the value $Q/P = 10^{-6}$. As the energy of the electrons increases the curvature of the tracks diminishes. There is some overlapping of the two distributions for the electrons and monopoles. Nevertheless, a cut at $Q/P < 10^{-6}$ would select the monopole tracks.

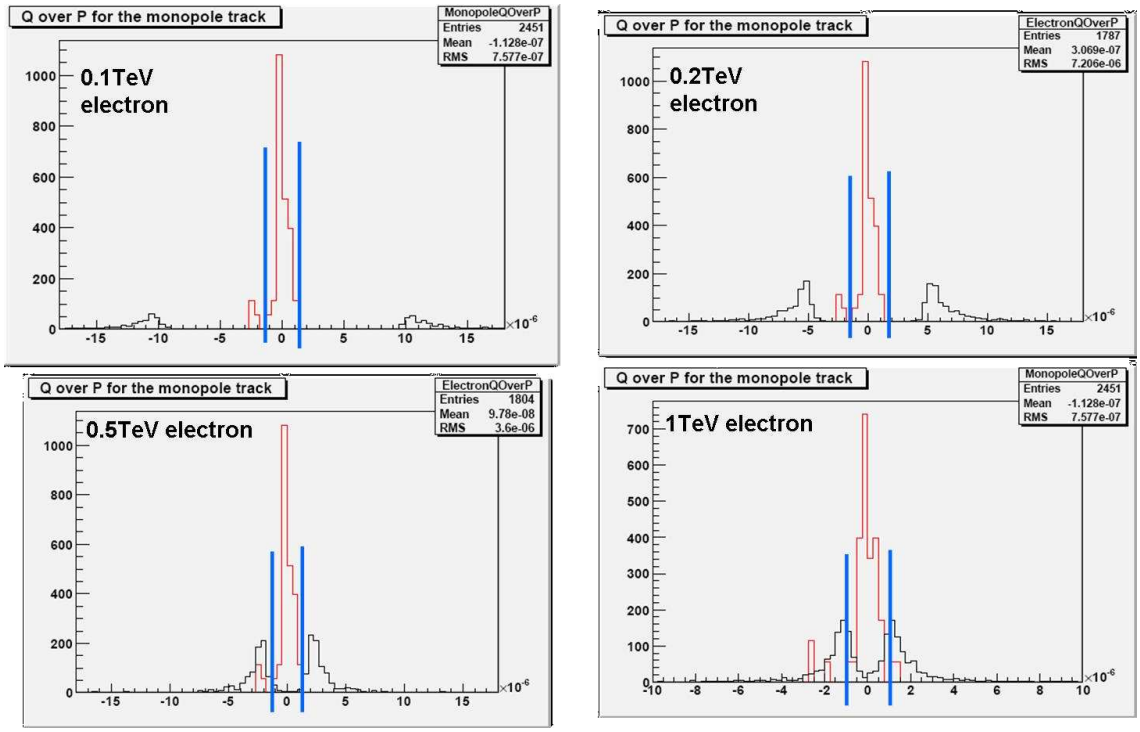

Figure 3.24. Q/P of monopole-red and electrons-black

The shape of the shower is investigated using a variable called Fracs1 defined as:

$$Fracs1 = \frac{E_7 - E_3}{E_7} \tag{3.65}$$

where E_7, E_3 are the energy in seven and three cells, respectively around the core of the calorimeter cluster. The values of this variable for the magnetic monopoles and for the electrons are shown in Fig. 3.25. These plots point to a value of Fracs1 = 0 for the magnetic monopole. From equation(3.65) we have $E_7 = E_3$ which means all the energy of the cluster is contained by three cells cluster implying a very narrow cluster. In this plot the value $Fracs1 = 0.05$ is marked by the solid line.A cut of $Fracs1 < 0.05$ will separate the monopoles clusters from the electrons clusters.

Once we established the magnetic monopole identification criteria, we have

Table 3.5. Magnetic monopole reconstruction cuts.

Variable	Cut value
Q/p	1×10^{-6}
$Fracs1$	0.05

to study how efficient those criteria are in selecting the monopole events. Table 3.5 summarizes the ATHENA variable defining the selections and their corresponding numerical values.

To calculate the reconstruction efficiency the following formula was used:

$$\epsilon_{Rec} = \frac{N(Rec)}{N(truth)} \tag{3.66}$$

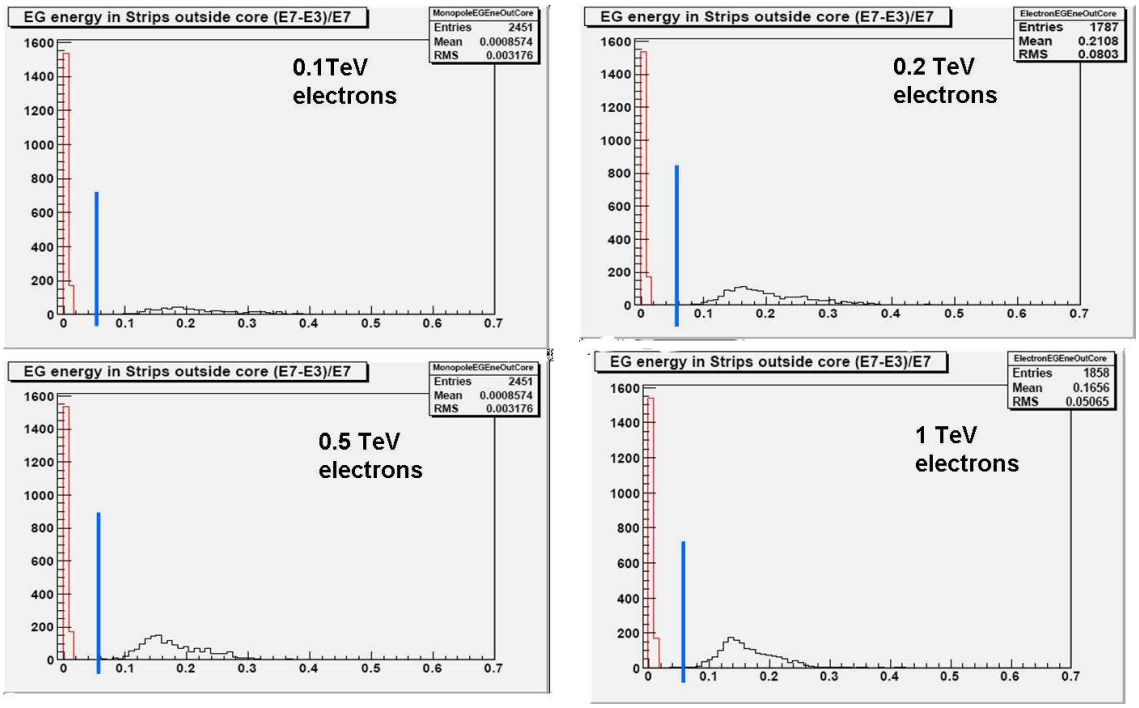

Figure 3.25. Fracs1 of monopole-red and electrons-black

where $N(Rec)$ represents the number of reconstructed events and $N(truth)$ represents the number of generated events. The reconstructed events are the events that the simulation package has propagate through the ATLAS detector. We are using events that passed already the Trigger requirements.

Just like in the trigger efficiency study, we start with a model independent efficiency evaluation using magnetic monopole events generated with the Single Particle Gun generator setup to produce events with uniform eta and phi distributions. Then we study the particular case of the Drell-Yan magnetic monopole process representing one of the models of the magnetic monopole production.

The reconstruction efficiencies were evaluated in two regions; the electromagnetic barrel ($\eta < 1.4$) and full detector region ($\eta < 2.5$) using a magnetic monopole sample with a fixed mass of 350 GeV. The resulting values are summarized in Table 3.6. Fig. 3.26 shows the dependency of the reconstruction efficiency on eta for the same sample.

Just like in the trigger study, the reconstruction efficiency depends on the monopole mass.

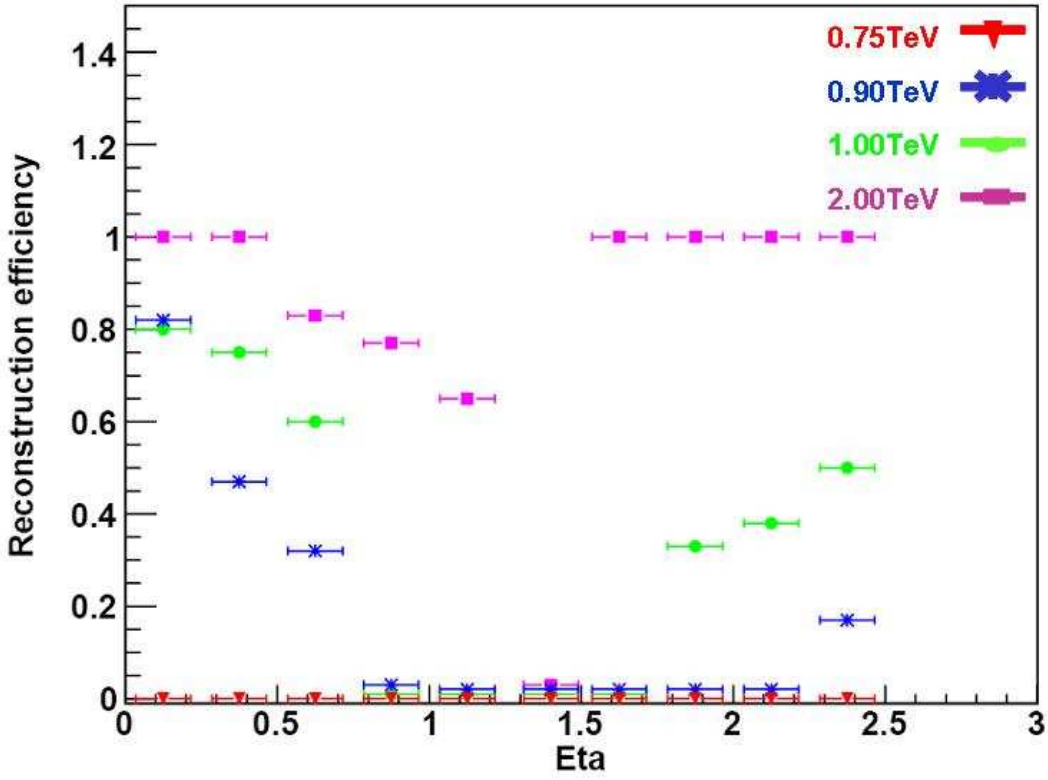

Figure 3.26. Eta distribution for reconstructed efficiencies for different monopole energies and same mass

Table 3.6. Reconstruction efficiency for magnetic monopoles with fixed mass of 350 GeV and different energies.

$SingleParticle$	ε_{Rec}	
$Energy(TeV)$	$\eta < 1.4$	$\eta < 2.5$
0.75	0.00 ± 0.027	0.00 ± 0.021
0.9	0.37 ± 0.013	0.24 ± 0.009
1	0.38 ± 0.010	0.40 ± 0.008
2	1.00 ± 0.027	1.00 ± 0.022

A sample of magnetic monopole produced using the Single Particle Gun generator was used. The generation energy is fixed at 1TeV, but the mass of the magnetic monopole is varied. Table 3.7 summarizes the results and Fig. 3.27 illustrates the eta distributions.

Table 3.7. Reconstruction efficiency for magnetic monopole with fixed energy of 1TeV and different masses.

$SingleParticle$	ε_{Rec}	
$Mass(TeV)$	$\eta < 1.4$	$\eta < 2.5$
0.35	0.38 ± 0.010	0.40 ± 0.008
0.50	0.18 ± 0.008	0.11 ± 0.005
0.60	0.00 ± 0.022	0.00 ± 0.017

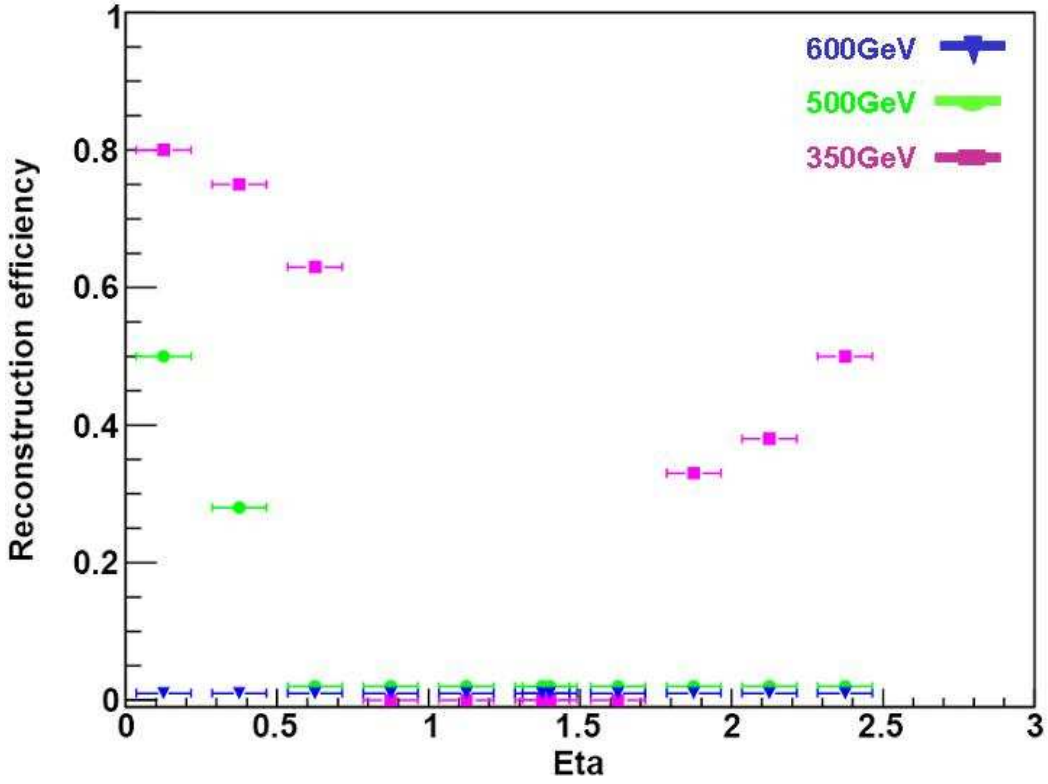

Figure 3.27. Eta distribution for reconstructed efficiencies for different monopole masses and same energy

The reconstruction efficiency for the Drell-Yan magnetic monopole channel is shown in Fig. 3.28. The sample used in this case is the same as in the trigger study. It was produced using the modified Pythia code. For the same reasons mentioned in the trigger study (existence of the crack between the EMB and the forward calorimeter at $\eta = 1.4$, and the increase in material density in Inner Detector) we observe a decrease in efficiency in the region $1.0 < \eta < 1.6$. Also the kinematics of the sample explains the high efficiency in the forward region.

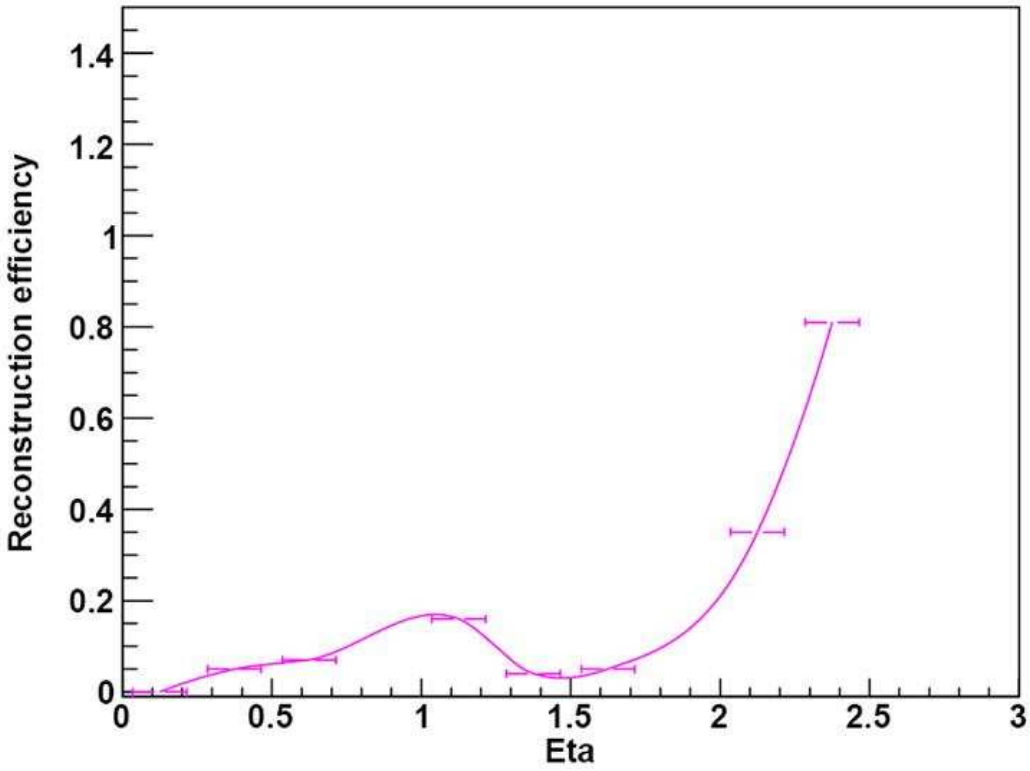

Figure 3.28. Eta distribution for trigger efficiencies for the Drell-Yan process

Knowing the reconstruction efficiency, the cross section calculated by Pythia and using the estimated luminosity for the first year for the ATLAS experiment, we can now evaluate the event rate which is the product of the two efficiencies eq.(3.63). In Fig.(3.29)we show the estimated number of events as a function of eta for two magnetic monopole Drell-Yan samples with two different masses 350 GeV and 500 GeV after a year of running with an luminosity of 1 fb^{-1}.As expected most of the detectable events will be in the forward calorimeter.

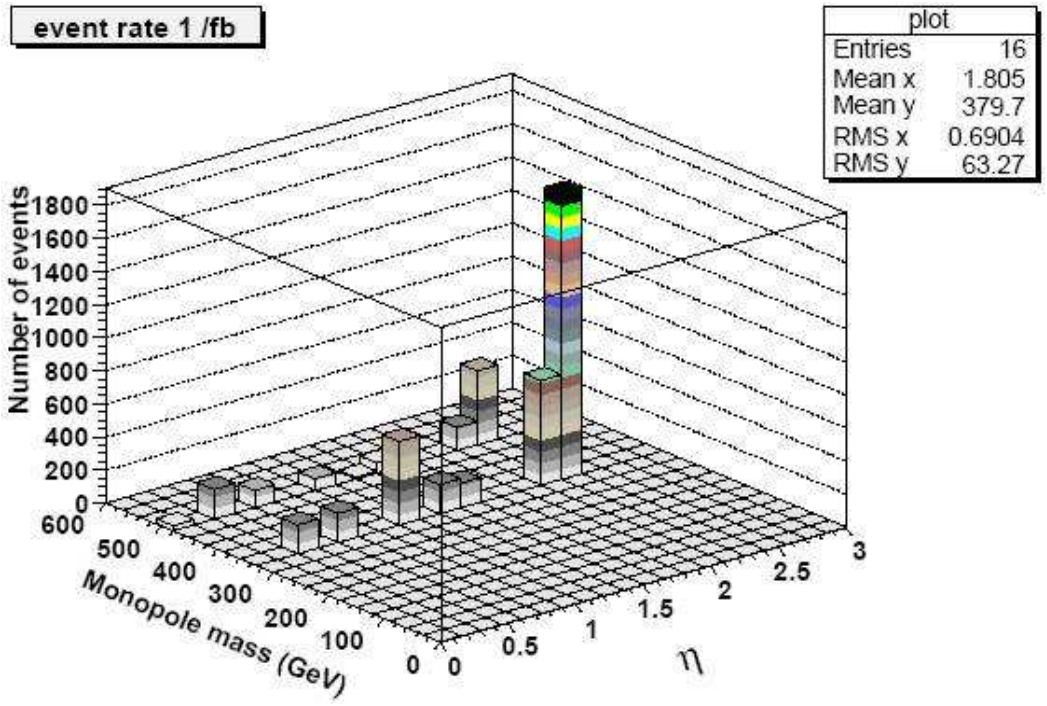

Figure 3.29. Event rate based on a $1fb^{-1}$ luminosity

3.2.3.3. Background

The LHC will collide protons with a centre-of-mass energy of 14 TeV. Most of the time the protons will pass through each other with low amount of momentum (low-pt) being transferred between the interacting partons. Only occasionally there will be a hard parton-parton collision, resulting in outgoing particles with large transverse momentum. The background of an event is everything except the two outgoing hard scattered particles. There are two components of the background: the minimum bias and the Underlying Event (UE). Both consists of events dominated by soft interactions. They differ only by the correlation of the UE with the "interesting" physics process with which it shares the same vertex.

We tested the validity of our analysis by applying the selection criteria listed in Table. 3.5 to signal and to the minimum bias data samples. In Fig. 3.30 we show the distribution of the Fracs variable before and after the 0.05 selection cut. Most of the events from both samples passed this cut. This can be explained by the fact that the minimum bias events have low energy thus generating narrow showers with characteristics similar to the magnetic monopole showers.

In Fig. 3.31 the distributions for the Q/P variable is shown. In this case, a cut at Q/P ¡ 1×10^{-6} clearly separates the linear trajectories of the magnetic monopole events from all others tracks, thus providing a very good background rejection.

We proceed in the same manner to test the UE. The way this sample was created was described in details in chapter 3.2.1.2. Because the particles in these events are created in the same parton-parton interactions that generate the magnetic monopole pairs they have higher energies and materialize in wider showers as illustrated in Fig. 3.32. Thus the cut on narrow shape of the shower easily selects the magnetic monopole events only.

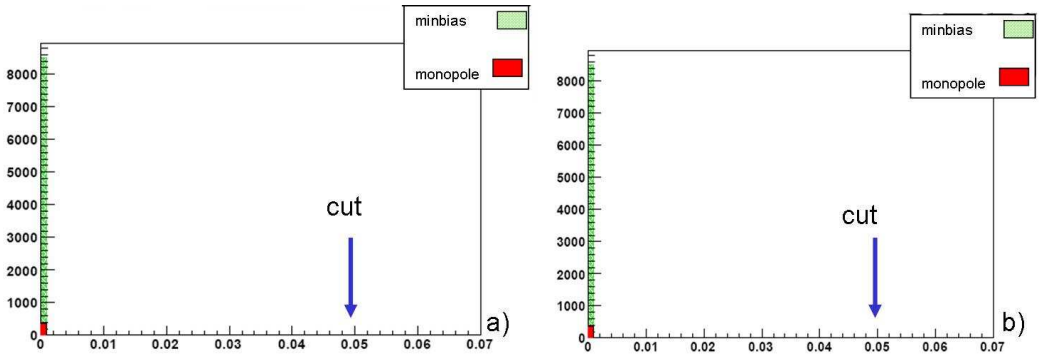

Figure 3.30. Effect on Fracs1 = 0.05 cut on Monopole vs minimum bias sample; Distribution before the cut (a), Distribution after the cut (b)

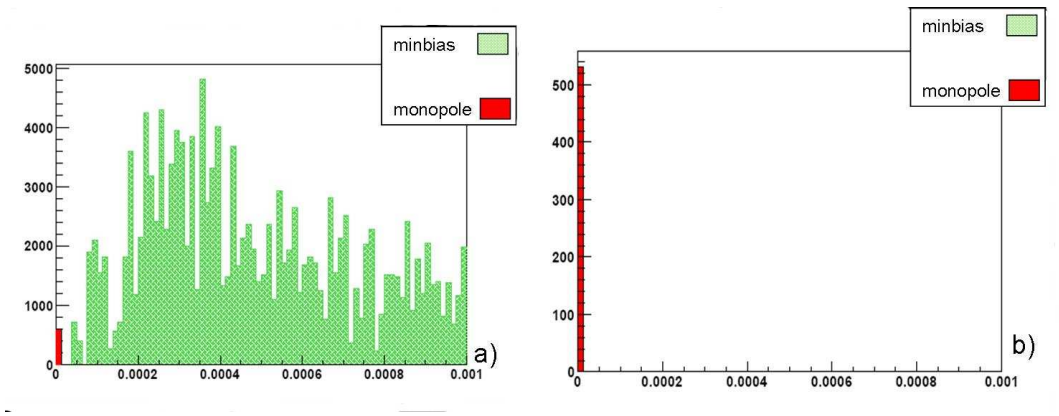

Figure 3.31. Effect on Q/P = 1×10^{-6} cut on Monopole vs minimum bias sample;Distribution before the cut (a), Distribution after the cut (b)

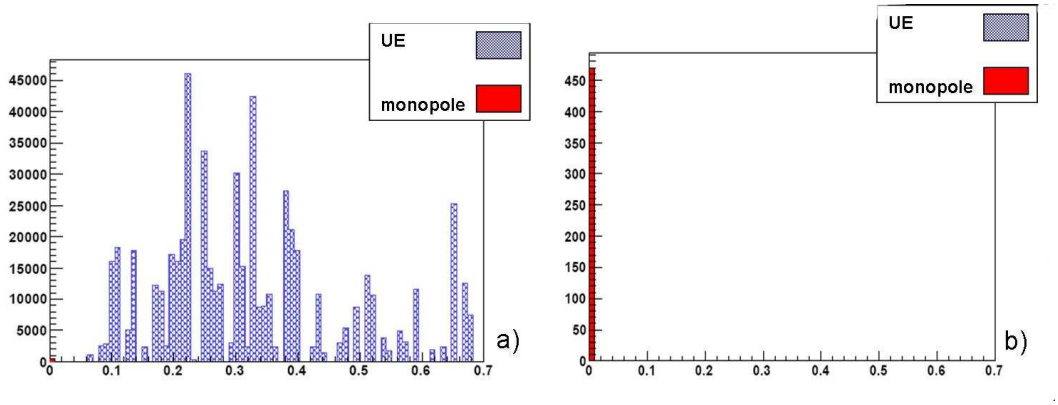

Figure 3.32. Effect on Fracs1 = 0.05 cut on Monopole vs UE sample; Distribution before the cut (a), Distribution after the cut (b)

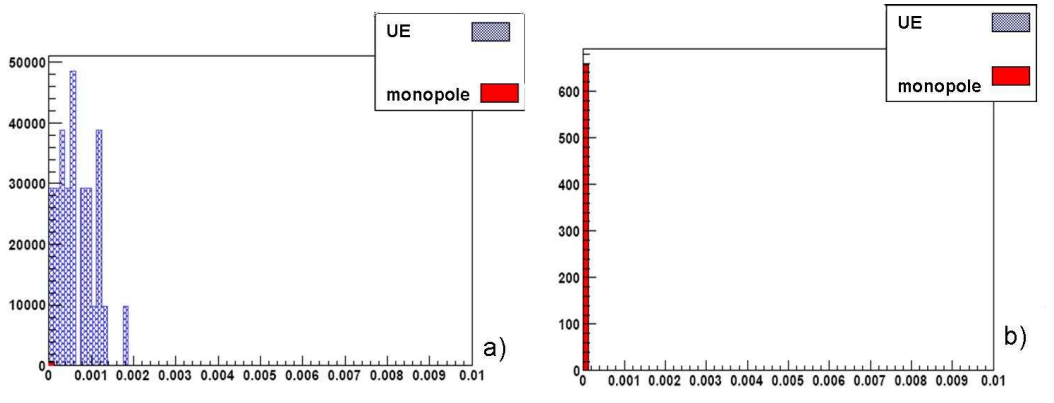

Figure 3.33. Effect on Q/P = 1×10^{-6} cut on Monopole vs UE sample;Distribution before the cut (a), Distribution after the cut (b)

The linearity of the tracks criteria is not satisfied by any of background events either, as seen in Fig. 3.33, thus leaving a pure magnetic monopole sample.

From this study, we conclude that in each individual background sample there are events that pass either the linearity of the track or the shape of the cluster selection threshold but the combination of the two conditions creates a powerful tool in separating magnetic monopole events only.

We proceed next to identify and evaluate the source of fake events. The fake events are standard physics events with other SM particles that survived all the magnetic monopole selection cuts. We tested the selection criteria on Drell-Yan events that produce muons, electrons and taus. In table 3.8 we show the cross section calculated by Pythia for 5000 events for the considered Drell-Yan background processes compared to the magnetic monopole DY cross section. In the last column to the right the ratios of event to background, for each individual background are shown. Based on these figures we normalize the signal to background. Furthermore, we apply a scale factor of $1000 : 1$ to reduce the background. The number of events in each sample as well as the percentage of events that passed each cut individually are are listed in Table 3.9. In the last right column are listed the number of events passing both selection criteria.

In Fig. 3.34 we plot the eta distribution of the reconstructed clusters for the signal and for all of the background processes. After the narrow cluster cut the distribution changes to the one shown in Fig. 3.35. We can see that there are still background events that survived the cut. The second cut, which requires linear tracks, is then applied and the remaining event distribution is shown in Fig. 3.36. No background events pass this second selection criteria.

Table 3.8. Cross sections for the magnetic monopole DY production and background samples.

Drell-Yan process	$\sigma_{DY}(mb)$	σ_{DY}/σ_{MM}
$Z \rightarrow \mu\mu$	1.11×10^{-4}	5842
$Z \rightarrow \tau\tau$	3.57×10^{-5}	1842
$Z \rightarrow ee$	1.10×10^{-4}	5789
MM with mass 350GeV	1.90×10^{-8}	1

Table 3.9. Magnetic monopole reconstruction cuts tested on different possible background samples.

Drell-Yan process	No. of events generated	Passed $Q/p < 1 \times 10^{-6}$	Passed $Fracs1 < 0.05$	Passed Both cuts
$Z \rightarrow \mu\mu$	44567	0.003 ± 0.007	0.069 ± 0.002	0.000±0.005
$Z \rightarrow \tau\tau$	14892	0.003 ± 0.008	0.124 ± 0.005	0.000±0.008
$Z \rightarrow ee$	41615	0.011 ± 0.001	0.185 ± 0.004	0.000±0.005
MM m=350GeV	8248	0.456 ± 0.007	0.434 ± 0.005	0.183±0.004

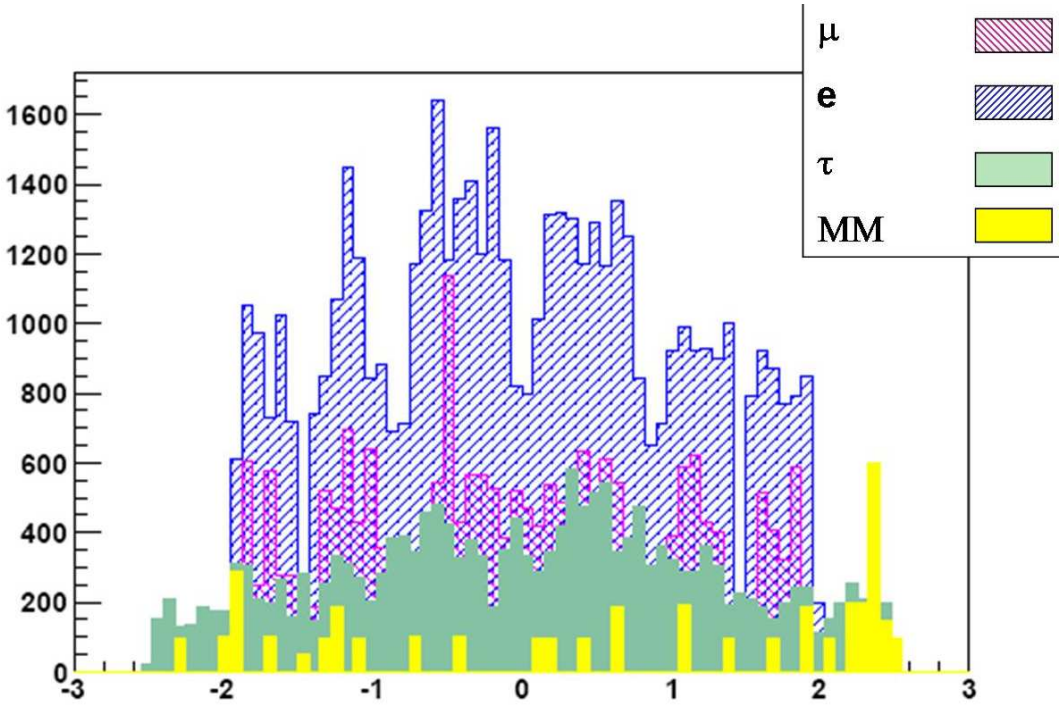

Figure 3.34. Eta distribution of reconstructed clusters for the signal and background

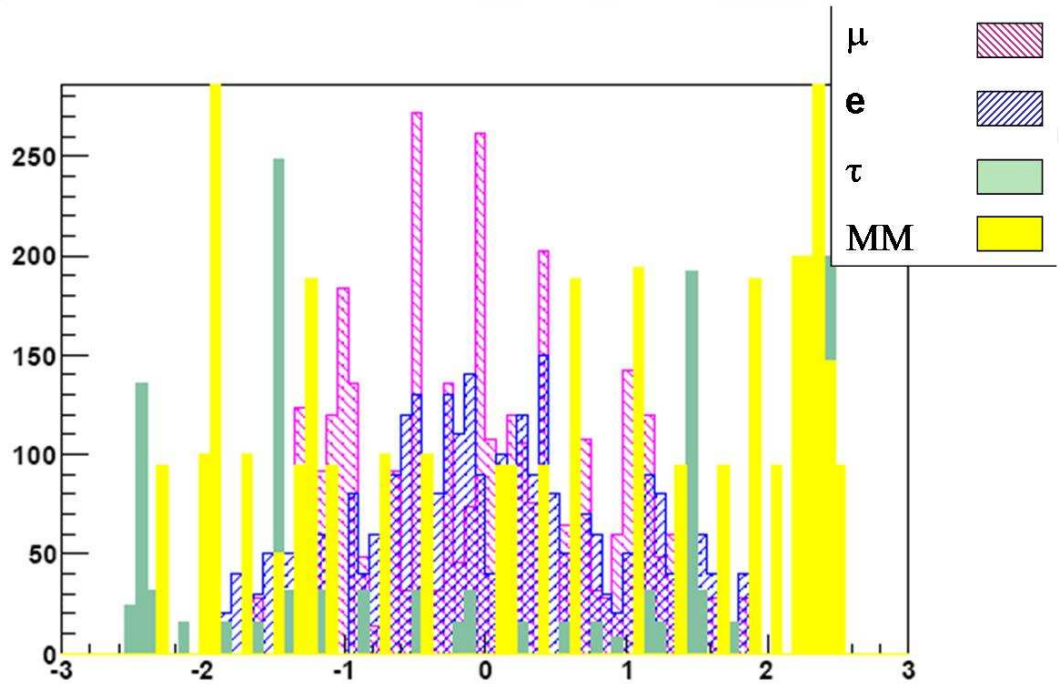

Figure 3.35. Eta distribution of clusters that qualify as a monopole cluster for the signal and background

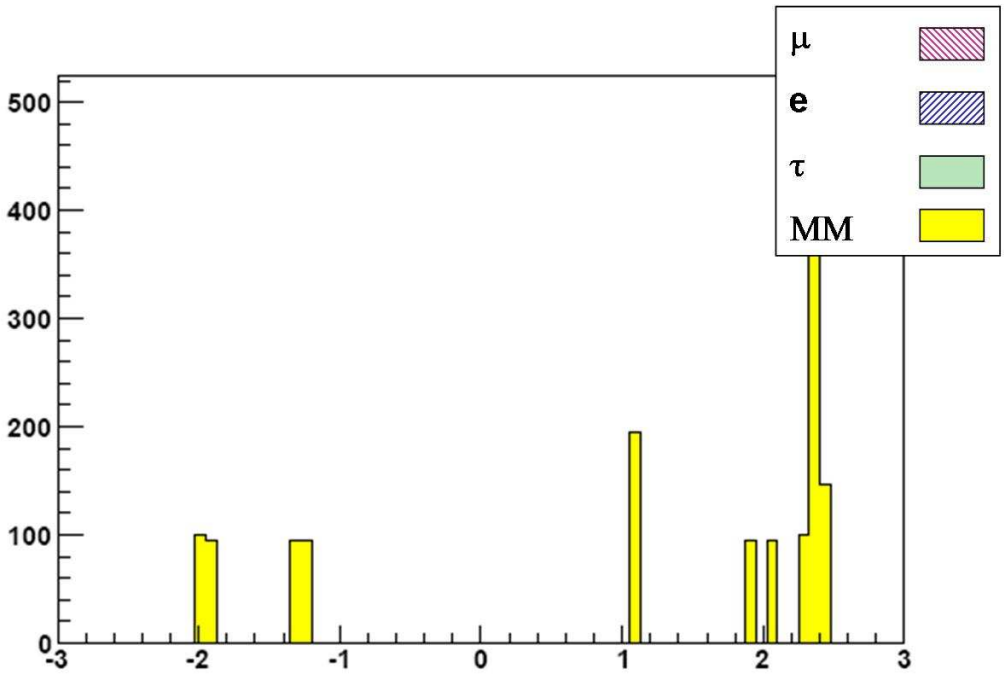

Figure 3.36. Eta distribution of monopole like events in signal and background

The estimated number of events versus background is calculated taking into account the cross section listed in Table 3.8 and the expected luminosity for the first year for the ATLAS experiment which is 1 fb^{-1}. The fact that a scaling factor was used is taken into account and the results are listed in Table 3.10. As an observation, the estimated number of magnetic monopoles events for the first year, obtained from this background evaluation study matches closely the estimation obtained in chapter 3.2.3.2 and plotted in Fig. 3.29.

As expected, the combination of these two cuts ensures a very good background

Table 3.10. Estimated magnetic monopole and background events.

Drell-Yan process	Number of events
$Z \rightarrow \mu\mu$	13
$Z \rightarrow \tau\tau$	3
$Z \rightarrow ee$	13
MM with mass 350GeV	3777

rejection mainly because the combination of a linear track and a narrow shower does not commonly occur. Usually, the linear track would infer a highly energetic particle which should create a wide shower. This unique signature is specific to magnetic monopoles events only.

3.3. Conclusion

This study shows that the magnetic monopole, if exist, will be detected with the ATLAS detector. The model independent selection cuts for the event makes this analysis a powerful tool that can be used with any future theoretical predicted process like the two photon monopole production [69].

In the particular case of the Drell-Yan magnetic monopole production that is used in this study, the huge production cross section is compensated by the important energy loss in interaction with the detector material. In spite the fact that a significant number of events are trapped before reaching the detector, the event rate is still optimistic.

A few images of the magnetic monopole Drell-Yan event were obtained using the ATLANTIS visualization package available in ATHENA. In Fig. 3.37 the magnetic monopole track is simulated in the Inner Detector. The shorter track represents a magnetic monopole that, after a certain distance inside the detector losses all of its energy thus getting stopped. The remaining track reaches the Electromagnetic Calorimeter where it creates a cluster as seen in Fig. 3.38.

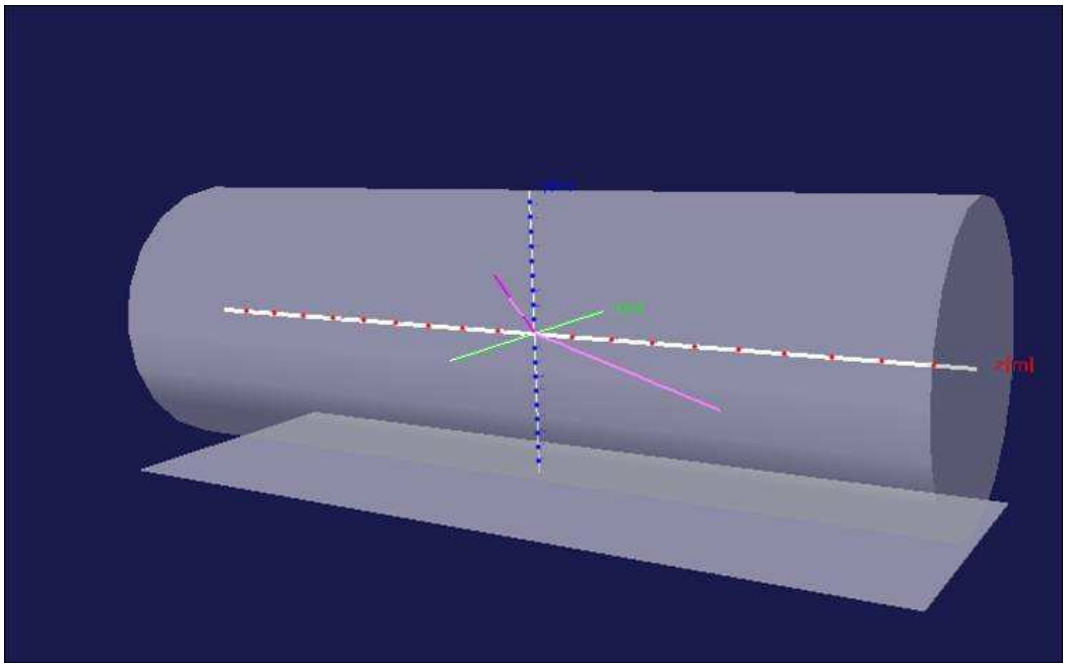

Figure 3.37. Three dimensional monopole track in Inner detector

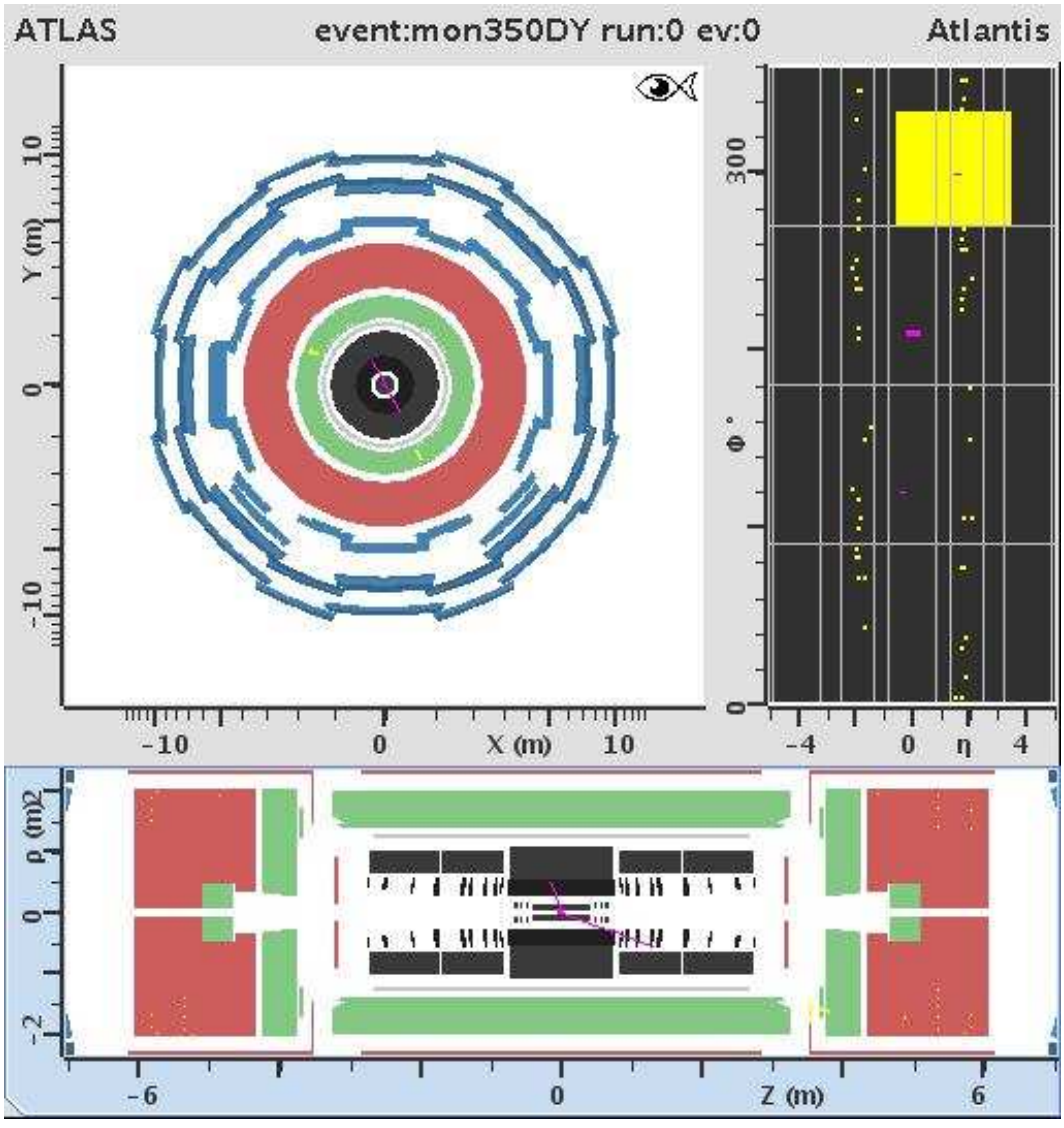

Figure 3.38. The magnetic monopole event inside the ATLAS detector

Appendix A

Acceleration of a magnetic charge in magnetic field

We need to evaluate the acceleration that a 2T magnetic field would exert on a unit magnetic charge(the Dirac charge $g_D = 68.5e$). Working with magnetic charges and magnetic fields is difficult so it is more useful to use the more familiar electric charge and electric field. The electromagnetic duality allows us to assume similar behavior of the magnetic charge in magnetic field as an electric charge in electric field. In electrodynamics the energy density of the field is defined as:

$$U_{EB} = \frac{1}{2}(\varepsilon_0 \mathbf{E}^2 + \frac{1}{\mu_0}\mathbf{B}^2) \tag{A.1}$$

where $\mathbf{E}$ and $\mathbf{B}$ are the electric and magnetic fields, ε_0 is the permittivity and μ_0 is the permeability of free space. If we assume equal contributions from the electric and magnetic fields we have:

$$\varepsilon_0 \mathbf{E}^2 = \frac{1}{\mu_0}\mathbf{B}^2 \tag{A.2}$$

which implies that:

$$\mathbf{E} = \frac{\mathbf{B}}{\sqrt{\varepsilon_0 \mu_0}} \tag{A.3}$$

Numerically we have:

$$\mathbf{E} = \frac{2T}{\sqrt{10^{-7}\frac{N}{A^2}10^{-12}\frac{F}{m}}} = \frac{2\frac{kg}{As^2}}{\sqrt{10^{-7}\frac{1}{A^2}(\frac{kg\cdot m}{s^2})10^{-12}\frac{1}{m}(\frac{s^4A^2}{m^2kg})}} = \frac{2}{\sqrt{10^{-19}}}\frac{kg\cdot m}{As^3} = 0.63\frac{V}{m} \tag{A.4}$$

This electric field represents the "equivalent" electric field that corresponds to the 2T magnetic field. Now we reduced the problem to finding the acceleration that a 0.63 V/m electric field would exert on a $q_M = 68.5e$ electric charge. The equation that give us the acceleration is:

$$q_M\mathbf{E} = m_M \cdot a_M \Rightarrow a_M = \frac{q_M\mathbf{E}}{m_M} \tag{A.5}$$

where m_M is the magnetic monopole mass. The acceleration that the same field would have on an electron would be:

$$q_e\mathbf{E} = m_e \cdot a_e \Rightarrow a_e = \frac{q_e\mathbf{E}}{m_e} \tag{A.6}$$

In this equation q_e is the electron charge and m_e is the electron mass. The ratio of the two acceleration is:

$$\frac{a_e}{a_M} = \frac{q_e m_M}{q_M m_e} \tag{A.7}$$

Using the lowest magnetic monopole mass of 350 GeV this ratio is of the order of:

$$\frac{a_e}{a_M} \simeq 10^4 \qquad (A.8)$$

From equation (A.8) we can conclude that the acceleration of the magnetic monopole in a 2 T magnetic field is 10^4 time smaller than the acceleration of the electron in an "equivalent" electric field. This effect is mainly due to the huge magnetic monopole mass. As the monopole mass increases the acceleration due to the magnetic field become negligible.

REFERENCES

[1] D.J.Griffiths, *Introduction to Elementary Particles*, Wiley,John Sons,ISBN 0-471-60386-4.

[2] I.J.Aitchison, A.J.Hey, *Gauge Theories in Particle Physics*,Inst.of Physics Pub. Inc.,ISBN 0-7503-0864-8.

[3] S. Weinberg, *Phys. Rev. Lett.* **19** (1967) 1264.

[4] A. Salam, *Proceedings of the 8th Nobel Symposium*, edited by N. Svartholm, Almquist and Wicksel, Stockholm, 1968 p.367.

[5] S. Glashow, *Nucl. Phys.* **22** (1961) 579.

[6] J.C. Maxwell,*Philosophical Transactions of the Royal Society of London* **155**(1865) 459-512.

[7] P.W. Higgs,*Phys. Rev. Lett.* **13**(1964) 508.

[8] T. P. Cheng,L.F. Li , *Gauge Theory of Elementary Particles*, Oxford University Press,ISBN 0-19-851961-3.

[9] J.W. Cronin,*Rev.Mod. Phys.* **53**(1981) 373-383.

[10] J. Ellis,*Nature* **448**(2007) 297-301.

[11] S. Witten,*Phys. Rev. Lett. B* **105**(1974) 267-271.

[12] E. Farhi, R. Jaffe,*Phys. Rev. Lett.* **D30**272 (1984).

[13] S. Dimopoulos, S. Landsberg,*Phys. Rev. Lett.* **87**161602(2001).

[14] ATLAS Technical Design Report.

[15] ATLAS Colaboration, Inner Detector Technical Design Report, CERN/LHCC/97-016/017 (1997).

[16] G.D. Hallewell,*Nucl. Instrum. Meth. Phys. Res.* **A383**(1996) 44.

[17] ATLAS Colaboration, Pixel Detector Technical Design Report,CERN/LHCC/98-013(1998).

[18] submitted to JINST on 24/12/2007,https://twiki.cern.ch/twiki/bin/view/Atlas/AtlasTechn

[19] ATLAS Colaboration, Muon Spectrometer Technical Design Report CERN/LHCC/97-22(1997).

[20] ATLAS Collaboration, Liquid Argon Calorimeter Technical Design Report, CERN/LHCC/96-041(1996).

[21] ATLAS Collaboration, Tile Calorimeter Technical Design Report, CERN/11205 LHCC/96-042(1996).

[22] E.Noether,"Invariante Variations probleme". *Math-phys.*253-257 (1918).

[23] Ta-Pei Cheng, Ling-Fong Li *Gauge Theory of Elementary Particle Physics*,Oxford University Press,ISBN:0-19-851961-3.

[24] J.F. Gunion, H. E. Haber, G. Kane and S. Dawson, *The Higgs Hunter's Guide*, Addison Wesley,1990.

[25] W.M. Yao et al.,*J. Phys.* **G33**(2006) 1.

[26] J. Wess, B. Zumino,*Phys. Lett* **49B** (1974) 52,

[27] A.Djouadi hep-ph/0503173.

[28] D0 Collaboration, *Nature* **429** 638-642 (2004).

[29] Review of Particle Properties, *J.Phys.G:Nucl.Part.Phys* **33** (2006).

[30] E. Brubaker for the CDF Collaboration,**arXiv:hep-ex/0605092v1**2006.

[31] N. M .Kroll and W. Wada, *Phys. Rev.Lett* **89** (2002) 1355.

[32] LOI of the ATLAS Collaboration, CERN/LHCC/92-4, Oct., 1992.

[33] R.H. Dalitz,*Proc.Phys.Soc.(London)* **A64** (1951) 667.

[34] N. M. Kroll and W. Wada, *Phys. Rev* **98** (1955) 1355.

[35] T. Miyazaki and E. Tagasugi, *Phys. Rev* **D8** (1973) 2051.

[36] M. and D. Schroeder, *Collider Physics*, Westview Press, 1996 ISBN:0-201-14945-1.

[37] C. G. Callan *Phys. Rev.* **D2**, 1541 (1970).

[38] K. Symanzik*Commun. Math. Phys.* **18**, 227 (1970).

[39] ATLAS Colaboration.CERN-LHCC/99-15(1999)

[40] Technical proposal CERN-LHCC/94-38(1994)

[41] A. Firan and R. Stroynowski, *Phys. Rev.* **D76** (2007) 057301.

[42] J.D. Jackson,*Classical Electrodynamics* (3rd ed.)Wiley ISBN 0-471-30932-X.

[43] J. Griffiths,*Introduction to Electrodynamics* (3rd ed.)Prentice-Hall,Inc., ISBN 0-138-05326-X.

[44] P.A.M. Dirac *Proc. R. Soc.* A **133**, 60 (1931).

[45] P.A.M. Dirac *Phys. Rev.* **74**, 817-830 (1948).

[46] R.A. Millikan *Phys. Rev. II* **2** 109 (1913).

[47] L. Gamberg, K.A. Milton, *Eikonal Scattering of Monopoles and Dyons in Dual QED*, hep-ph/0005016

[48] G. tHooft,*Nucl. Phys.* **B79**, 276 (1974).

[49] A. Polyakov, Pisma. Eksp.*Teor. Fiz.* **20**, 430 (1974) [JETP Lett. 20, 194 (1974)].

[50] R.D. Sorkin *Phys. Rev Lett* **B 51** 87 (1983).

[51] T.T.Wu,C.N.Yang, *The Properties of Matter Under Unusual Conditions*, Ed. by H.Mark,S.Fernbach, Wiley, 1969.

[52] B. Cabrera *Phys. Rev. Lett.* **48** 1378-1381 (1982).

[53] G. Giacomelli and L. Patrizii,**hep-ex/0112009**(2001).

[54] CDF Collaboration, *Phys. Rev. Lett* **96**,201801 (2006).

[55] G.R. Kalbfleisch et all., *Phys. Rev. Lett* **85**, 5292 (2000;G.R. Kalbfleisch et all., *Phys. Rev.* **D 69**, 052002 (2004.

[56] G. Giacomelli and L. Patrizii,**hep-ex/0302011**(2003).

[57] G.R. Kalbfleisch et all., *Phys. Rev.* **D 69**, 052002 (2004.

[58] M.J. Mulhearn, *A Direct Search for Magnetic Monopoles* **FERMILAB-THESIS** 2004-51.

[59] J.S. Schwinger, K.A. Milton, W.Y.Tsai, L.L.DeRaad and D.C. Clark, *Nonrelativistic dyon dyon scattering*, *Annals Phys.* **1001**,451 (1976.

[60] K.A.Milton *Prog.Rep in Phys.* **69** 1637-1711 (2006).

[61] R. Stroynowski,*Phys.Rept* **71**,1 (1981).

[62] T. Sjöstrand, P. Edén, C. Friberg, L. Lönnblad, G. Miu, S. Mrenna and E. Norrbin, *J. Computer Physics Commun* 135 (2001) 238.

[63] G.Giacomelli *Theory and Detection of magnetic Monopoles in Gauge Theories*,ed N. Craigie p.407(Singapore World Scientific Publishing Co.,1986).

[64] S.P. Ahlen, *Rev.Mod.Phys.* **52**,121(1980).

[65] S.D.Wick, T.W.Kephart, T.J. Weiler and P.L. Biermann, *Signatures for a Cosmic Flux of Magnetic Monopoles*, *Astropart. Phys.***18**,663 (2003).

[66] , R.M.Sternheimer,R.F.Peierls, *General expression for the density effect for the ionization loss of charged particles*,*Phys.Rev.* B3,3681(1971)

[67] http://geant4.cern.ch

[68] G.Bauer and co., *Search for Magnetic Monopoles at CDF using the Time-of-Flight Detector***CDF note**,5506(2000).

[69] Yu.Kurochkin,I.Satusunkevich,Dz.Soukavy, *On production of magnetic monopoles via photon-photon fusion at high energy pp collisions*,*Mod.Phys.Lett.A* **21**, 38(2006).

[70] D0 Collab.*Phys. Rev. Lett.* **81**, 524 (1998).

[71] N. Kauer, T. Plehn, D. Rainwater and D. Zeppenfeld, *Phys. Rev. Lett* **B503:113-1208** (2001.

[72] D. Rainwater and D. Zeppenfeld, *Phys. Rev.* **D60:113004** (1999.

[73] T. Plehn, D. Rainwater and D. Zeppenfeld, *Phys. Rev.* **D61:093005** (2000).

[74] M. Peskin and D. Schroeder, *An Introduction to Quantum Field Theory*, Basic Books, 1995.